Available online at www.sciencedirect.com
ScienceDirect
Comput. Methods Appl. Mech. Engrg. 372 (2020) 113397
Computer methods in applied mechanics and engineering
www.elsevier.com/locate/cma

Hybridisable discontinuous Galerkin solution of geometrically parametrised Stokes flows

Ruben Sevilla[a,*], Luca Borchini[a,b], Matteo Giacomini[b,c], Antonio Huerta[b,c]

[a] *Zienkiewicz Centre for Computational Engineering, College of Engineering, Swansea University, Bay Campus, SA1 8EN, Wales, United Kingdom*
[b] *Laboratori de Calcul Numeric (LaCàN), ETS de Ingenieros de Caminos, Canales y Puertos, Universitat Politècnica de Catalunya, Barcelona, Spain*
[c] *Centre Internacional de Mètodes Numèrics en Enginyeria (CIMNE), Barcelona, Spain*

Received 18 June 2020; received in revised form 24 August 2020; accepted 24 August 2020
Available online xxxx

Abstract

This paper proposes a novel computational framework for the solution of geometrically parametrised flow problems governed by the Stokes equation. The proposed method uses a high-order hybridisable discontinuous Galerkin formulation and the proper generalised decomposition rationale to construct an off-line solution for a given set of geometric parameters. The generalised solution contains the information for all the geometric parameters in a user-defined range and it can be used to compute sensitivities. The proposed approach circumvents many of the weaknesses of other approaches based on the proper generalised decomposition for computing generalised solutions of geometrically parametrised problems. Four numerical examples show the optimal mesh convergence properties of the proposed method and demonstrate its applicability in two and three dimensions, with particular emphasis on parametrised flows in microfluidics.

Keywords: Reduced order model; Geometry parametrisation; Hybridisable discontinuous Galerkin (HDG); Proper generalised decomposition (PGD)

1. Introduction

Reduced order models (ROMs) have become commonplace in many areas of computational sciences and engineering [1]. Some popular ROMs used to reduce the complexity of high dimensional problems include the reduced basis method [2], the proper orthogonal decomposition (POD) [3–5] and the proper generalised decomposition (PGD) [6–8].

One of the main attractive properties of the PGD is its ability to build reduced basis without prior knowledge of the solution [6–8]. However, the intrusive implementation and the difficulty in handling geometrically parametrised problems has often been considered a difficulty when considering its application to complex problems. In recent years, there have been an increase in non-intrusive implementations of the PGD [9–11]. In terms of geometrically parametrised problems, early work focused on solutions tailored to specific problems [12–15] or strategies only

* Corresponding author.
E-mail addresses: r.sevilla@swansea.ac.uk (R. Sevilla), luca.borchini@upc.edu (L. Borchini), matteo.giacomini@upc.edu (M. Giacomini), antonio.huerta@upc.edu (A. Huerta).

https://doi.org/10.1016/j.cma.2020.113397

applicable in a context of low order approximations [16,17]. Similar to the work in [16,17], where piecewise linear geometric parametrisations are used, other PGD approaches that employ piecewise NURBS parametrisations have been proposed [18]. More recently, a general approach to deal with geometrically parametrised problems in a CAD environment was proposed [19]. The previously mentioned PGD strategies using high order approximations lead to the need to use the so-called high-order PGD projection [20] to separate some terms of the weak formulation.

In this work a PGD strategy is proposed in the framework of the hybridisable discontinuous Galerkin (HDG) method [21–25]. The use of a mixed formulation is shown to be beneficial as all the terms of the weak formulation can be written in a separated form, as required by the PGD, without invoking to the memory intensive high-order PGD projection. The use of the HDG method for the spatial discretisation also guarantees that equal order of approximation can be used for all the variables circumventing the so-called Ladyzhenskaya–Babuška–Brezzi (LBB) condition. This is of special importance in this work, where geometrically parametrised domains are considered with curved boundaries. The use of the same degree of approximation for all the variables means that standard isoparametric elements can be used. In contrast, the work in [19], employing standard FEs, required the use of sub-parametric or super-parametric formulations in the presence of curved boundaries due to the different degree of approximation used for the velocity and pressure, as required to satisfy the LBB condition. Furthermore, the proposed HDG-PGD approach facilitates the imposition of the Dirichlet boundary conditions as in the HDG context all boundary conditions are weakly imposed.

The formulation is presented using Stokes flows as the model problem. However, it is worth mentioning that there has been a substantial effort in developing HDG methods for a variety of problems in different areas of science and engineering [26–33] and therefore, the proposed approach can be easily extended to a wide range of problems. It is also worth noting that the integration within a CAD environment proposed in [19] is also feasible given the recent development of a coupled HDG-NEFEM formulation for fluid [34] and solid mechanics [35].

The structure of the remainder of the paper is as follows. Section 2 presents the Stokes flow problem on a geometrically parametrised domain and the corresponding multi-dimensional parametric problem. The HDG formulation for the multi-dimensional parametric Stokes problem is described in Section 3. The proposed PGD rationale is described in detail in Section 4. Section 5 presents a series of numerical examples involving Stokes flow problems in two and three dimensions. Finally, Section 6 presents the conclusions of the work that has been presented.

2. Problem statement

2.1. The Stokes problem on a parametrised domain

Let us consider a parametrised domain $\Omega^{\boldsymbol{\mu}} \subset \mathbb{R}^{\mathtt{n_{sd}}}$, where $\mathtt{n_{sd}}$ is the number of spatial dimensions and $\boldsymbol{\mu} \in \boldsymbol{\mathcal{I}} \subset \mathbb{R}^{\mathtt{n_{pa}}}$ is a set of geometric parameters that controls the boundary representation of the domain, with $\mathtt{n_{pa}}$ being the number of geometric parameters. It is worth noting that the set of geometric parameters can be written as $\boldsymbol{\mathcal{I}} := \mathcal{I}^1 \times \mathcal{I}^2 \times \cdots \times \mathcal{I}^{\mathtt{n_{pa}}}$ with $\mu_j \in \mathcal{I}^j$ for $j = 1, \ldots, \mathtt{n_{pa}}$.

For any set of parameters $\boldsymbol{\mu}$, the goal is to find the parametric velocity, $\boldsymbol{u}(\boldsymbol{x}^{\boldsymbol{\mu}})$, and pressure, $p(\boldsymbol{x}^{\boldsymbol{\mu}})$, fields that satisfy the Stokes problem given by

$$
\begin{cases}
-\nabla\cdot(\nu\nabla\boldsymbol{u} - p\mathbf{I}_{\mathtt{n_{sd}}}) = \boldsymbol{s} & \text{in } \Omega^{\boldsymbol{\mu}},\\
\nabla\cdot\boldsymbol{u} = 0 & \text{in } \Omega^{\boldsymbol{\mu}},\\
\boldsymbol{u} = \boldsymbol{u}_D & \text{on } \Gamma_D^{\boldsymbol{\mu}},\\
\boldsymbol{n}^{\boldsymbol{\mu}}\cdot\left(\nu\nabla\boldsymbol{u} - p\mathbf{I}_{\mathtt{n_{sd}}}\right) = \boldsymbol{g}_N & \text{on } \Gamma_N^{\boldsymbol{\mu}},\\
\boldsymbol{u}\cdot\boldsymbol{D}^{\boldsymbol{\mu}} + \boldsymbol{n}^{\boldsymbol{\mu}}\cdot\left(\nu\nabla\boldsymbol{u} - p\mathbf{I}_{\mathtt{n_{sd}}}\right)\boldsymbol{E}^{\boldsymbol{\mu}} = \mathbf{0} & \text{on } \Gamma_S^{\boldsymbol{\mu}},
\end{cases}
\tag{1}
$$

where $\nu > 0$ is the kinematic viscosity, $\boldsymbol{s}$ is the volumetric source and $\boldsymbol{n}^{\boldsymbol{\mu}}$ is the outward unit normal vector to $\partial\Omega^{\boldsymbol{\mu}}$. The boundary of the domain, $\partial\Omega^{\boldsymbol{\mu}}$, is partitioned into the non-overlapping Dirichlet, $\Gamma_D^{\boldsymbol{\mu}}$, Neumann, $\Gamma_N^{\boldsymbol{\mu}}$, and slip, $\Gamma_S^{\boldsymbol{\mu}}$, boundaries such that $\overline{\partial\Omega}^{\boldsymbol{\mu}} = \overline{\Gamma}_D^{\boldsymbol{\mu}} \cup \overline{\Gamma}_N^{\boldsymbol{\mu}} \cup \overline{\Gamma}_S^{\boldsymbol{\mu}}$. On the Dirichlet boundary the velocity is given by $\boldsymbol{u}_D$. On the Neumann boundary the *pseudo-traction* is given by $\boldsymbol{g}_N$. Finally, on the slip boundary, the matrices $\boldsymbol{D}^{\boldsymbol{\mu}}$ and $\boldsymbol{E}^{\boldsymbol{\mu}}$ are given by $\boldsymbol{D}^{\boldsymbol{\mu}} = [\boldsymbol{n}^{\boldsymbol{\mu}}, \mathbf{0}_{\mathtt{n_{sd}}\times(\mathtt{n_{sd}}-1)}]$ and $\boldsymbol{E}^{\boldsymbol{\mu}} = [\mathbf{0}, \boldsymbol{t}_1^{\boldsymbol{\mu}}, \ldots, \boldsymbol{t}_{\mathtt{n_{sd}}-1}^{\boldsymbol{\mu}}]$, as detailed in [25]. The tangential vectors $\boldsymbol{t}_k^{\boldsymbol{\mu}}$, for $k = 1, \ldots \mathtt{n_{sd}} - 1$ are such that $\{\boldsymbol{n}^{\boldsymbol{\mu}}, \boldsymbol{t}_1^{\boldsymbol{\mu}}, \ldots, \boldsymbol{t}_{\mathtt{n_{sd}}-1}^{\boldsymbol{\mu}}\}$ form an orthonormal system of vectors.

The free divergence condition in Eq. (1) induces the compatibility condition

$$\langle 1, \boldsymbol{u}_D \cdot \boldsymbol{n}^{\boldsymbol{\mu}} \rangle_{\Gamma_D^{\boldsymbol{\mu}}} + \langle 1, \boldsymbol{u} \cdot \boldsymbol{n}^{\boldsymbol{\mu}} \rangle_{\partial\Omega^{\boldsymbol{\mu}} \setminus \Gamma_D^{\boldsymbol{\mu}}} = 0, \tag{2}$$

where $\langle \cdot, \cdot \rangle_S$ denotes the standard $\mathcal{L}_2$ scalar product in any domain $S \subset \partial\Omega^{\boldsymbol{\mu}}$.

In addition, it is worth noting that, if $\Gamma_N^{\boldsymbol{\mu}} = \emptyset$, an additional constraint to avoid the indeterminacy of the pressure is required. One common option [36–39] that is considered here, consists of imposing the mean pressure on the boundary of the domain, namely

$$\left\langle \frac{1}{|\partial\Omega^{\boldsymbol{\mu}}|} p, 1 \right\rangle_{\partial\Omega^{\boldsymbol{\mu}}} = 0. \tag{3}$$

2.2. The multi-dimensional parametric Stokes problem

The classical strategy to solve the parametric Stokes problem is to solve equation (1) for every set of parameters $\boldsymbol{\mu} \in \boldsymbol{\mathcal{I}}$. However, this strategy is not well suited when fast queries are required.

Reduced order models have demonstrated to be a viable alternative to compute multi-dimensional parametric solutions in an offline phase. Once the offline solution is available, the computation of the solution for a given set of parameters has a very small computational cost, being very well suited for applications where fast queries are required.

The multi-dimensional parametric problem arises from interpreting $\boldsymbol{\mu}$ as additional parametric coordinates, rather than parameters of the problem. In the context of the Stokes problem considered here, the strategy is to consider the velocity and pressure fields as functions in a multidimensional space, namely $\boldsymbol{u}(\boldsymbol{x}^{\boldsymbol{\mu}}, \boldsymbol{\mu})$ and $p(\boldsymbol{x}^{\boldsymbol{\mu}}, \boldsymbol{\mu})$. The multi-dimensional parametric Stokes problem can be written as

$$\begin{cases} -\nabla_{\boldsymbol{\mu}} \cdot (\nu \nabla_{\boldsymbol{\mu}} \boldsymbol{u} - p \mathbf{I}_{\mathtt{nsd}}) = \boldsymbol{s} & \text{in } \Omega^{\boldsymbol{\mu}} \times \boldsymbol{\mathcal{I}}, \\ \nabla_{\boldsymbol{\mu}} \cdot \boldsymbol{u} = 0 & \text{in } \Omega^{\boldsymbol{\mu}} \times \boldsymbol{\mathcal{I}}, \\ \boldsymbol{u} = \boldsymbol{u}_D & \text{on } \Gamma_D^{\boldsymbol{\mu}} \times \boldsymbol{\mathcal{I}}, \\ \boldsymbol{n}^{\boldsymbol{\mu}} \cdot \left(\nu \nabla_{\boldsymbol{\mu}} \boldsymbol{u} - p \mathbf{I}_{\mathtt{nsd}}\right) = \boldsymbol{g}_N & \text{on } \Gamma_N^{\boldsymbol{\mu}} \times \boldsymbol{\mathcal{I}}, \\ \boldsymbol{u} \cdot \boldsymbol{D}^{\boldsymbol{\mu}} + \boldsymbol{n}^{\boldsymbol{\mu}} \cdot \left(\nu \nabla_{\boldsymbol{\mu}} \boldsymbol{u} - p \mathbf{I}_{\mathtt{nsd}}\right) \boldsymbol{E}^{\boldsymbol{\mu}} = \boldsymbol{0} & \text{on } \Gamma_S^{\boldsymbol{\mu}} \times \boldsymbol{\mathcal{I}}. \end{cases} \tag{4}$$

For the multi-dimensional problem, the compatibility condition induced by the free divergence condition can be written as

$$\langle 1, \boldsymbol{u}_D \cdot \boldsymbol{n}^{\boldsymbol{\mu}} \rangle_{\Gamma_D^{\boldsymbol{\mu}} \times \boldsymbol{\mathcal{I}}} + \langle 1, \boldsymbol{u} \cdot \boldsymbol{n}^{\boldsymbol{\mu}} \rangle_{(\partial\Omega^{\boldsymbol{\mu}} \setminus \Gamma_D^{\boldsymbol{\mu}}) \times \boldsymbol{\mathcal{I}}} = 0 \tag{5}$$

and the additional constraint to avoid the indeterminacy of the pressure, required when $\Gamma_N^{\boldsymbol{\mu}} = \emptyset$, becomes

$$\left\langle \frac{1}{|\partial\Omega^{\boldsymbol{\mu}}|} p, 1 \right\rangle_{\partial\Omega^{\boldsymbol{\mu}} \times \boldsymbol{\mathcal{I}}} = 0. \tag{6}$$

3. Hybridisable discontinuous Galerkin formulation

Let us consider a subdivision of the domain $\Omega^{\boldsymbol{\mu}}$ in $\mathtt{n_{el}}$ disjoint subdomains $\Omega_e^{\boldsymbol{\mu}}$ such that

$$\overline{\Omega}^{\boldsymbol{\mu}} = \bigcup_{e=1}^{\mathtt{n_{el}}} \overline{\Omega}_e^{\boldsymbol{\mu}}. \tag{7}$$

The interior boundaries of the subdomains define the so-called mesh skeleton or internal interface $\Gamma^{\boldsymbol{\mu}}$ as

$$\Gamma^{\boldsymbol{\mu}} := \left[\bigcup_{e=1}^{\mathtt{n_{el}}} \partial\Omega_e^{\boldsymbol{\mu}} \right] \setminus \partial\Omega^{\boldsymbol{\mu}}. \tag{8}$$

A partition of the parametric domains $\mathcal{I}^j$, for $j = 1, \ldots, \mathtt{n_{pa}}$, in $\mathtt{n}_{\mathtt{el}}^j$ disjoint subdomains $\mathcal{I}_e^j$ such that

$$\overline{\mathcal{I}}^j = \bigcup_{e=1}^{\mathtt{n}_{\mathtt{el}}^j} \overline{\mathcal{I}}_e^j, \tag{9}$$

is also considered to use a Galerkin approach for the parametric problems. This is in contrast with other approaches that use collocation for the parametric problems.

This section briefly presents the HDG formulation for the multi-dimensional parametric Stokes problem. The presentation is based on previous work on HDG methods found in [36,37,39,40].

3.1. Mixed formulation

Introducing the so-called *mixed variable* $\boldsymbol{L} = -\nu \nabla_{\boldsymbol{\mu}} \boldsymbol{u}$, the Stokes problem can be written as a first-order system of equations in the broken computational domain, namely

$$\begin{cases} \boldsymbol{L}_e + \nu \nabla_{\boldsymbol{\mu}} \boldsymbol{u}_e = \boldsymbol{0} & \text{in } \Omega_e^{\boldsymbol{\mu}} \times \boldsymbol{\mathcal{I}}, \text{ and for } e = 1, \dots, \mathtt{n_{el}}, \\ \nabla_{\boldsymbol{\mu}} \cdot \left(\boldsymbol{L}_e + p_e \mathbf{I}_{\mathtt{n_{sd}}} \right) = \boldsymbol{s} & \text{in } \Omega_e^{\boldsymbol{\mu}} \times \boldsymbol{\mathcal{I}}, \text{ and for } e = 1, \dots, \mathtt{n_{el}}, \\ \nabla_{\boldsymbol{\mu}} \cdot \boldsymbol{u}_e = 0 & \text{in } \Omega_e^{\boldsymbol{\mu}} \times \boldsymbol{\mathcal{I}}, \text{ and for } e = 1, \dots, \mathtt{n_{el}}, \\ \boldsymbol{u}_e = \boldsymbol{u}_D & \text{on } \left(\partial \Omega_e^{\boldsymbol{\mu}} \cap \Gamma_D^{\boldsymbol{\mu}} \right) \times \boldsymbol{\mathcal{I}}, \\ \boldsymbol{n}^{\boldsymbol{\mu}} \cdot \left(\boldsymbol{L}_e + p_e \mathbf{I}_{\mathtt{n_{sd}}} \right) = -\boldsymbol{g}_N & \text{on } \left(\partial \Omega_e^{\boldsymbol{\mu}} \cap \Gamma_N^{\boldsymbol{\mu}} \right) \times \boldsymbol{\mathcal{I}}, \\ \boldsymbol{u}_e \cdot \boldsymbol{D}^{\boldsymbol{\mu}} - \boldsymbol{n}^{\boldsymbol{\mu}} \cdot \left(\boldsymbol{L}_e + p_e \mathbf{I}_{\mathtt{n_{sd}}} \right) \boldsymbol{E}^{\boldsymbol{\mu}} = \boldsymbol{0} & \text{on } \left(\partial \Omega_e^{\boldsymbol{\mu}} \cap \Gamma_S^{\boldsymbol{\mu}} \right) \times \boldsymbol{\mathcal{I}}, \\ [\![\boldsymbol{u} \otimes \boldsymbol{n}^{\boldsymbol{\mu}}]\!] = \boldsymbol{0} & \text{on } \Gamma^{\boldsymbol{\mu}} \times \boldsymbol{\mathcal{I}}, \\ [\![\boldsymbol{n}^{\boldsymbol{\mu}} \cdot \left(\boldsymbol{L} + p \mathbf{I}_{\mathtt{n_{sd}}} \right)]\!] = \boldsymbol{0} & \text{on } \Gamma^{\boldsymbol{\mu}} \times \boldsymbol{\mathcal{I}}, \end{cases} \tag{10}$$

where the last two equations, known as *transmission conditions*, impose the continuity of the velocity and the normal flux on the mesh skeleton. Following [41], the *jump* operator $[\![\cdot]\!]$ is defined as the sum from the left, Ω_l, and right, Ω_r, elements of a given portion of the interface $\Gamma^{\mu} \times \boldsymbol{\mathcal{I}}$, that is

$$[\![\odot]\!] = \odot_l + \odot_r. \tag{11}$$

3.2. Strong form of the local and global problems

The HDG method solves the mixed problem of Eq. (10) in two steps. First, the so-called *local problems* are considered

$$\begin{cases} \boldsymbol{L}_e + \nu \nabla_{\boldsymbol{\mu}} \boldsymbol{u}_e = \boldsymbol{0} & \text{in } \Omega_e^{\boldsymbol{\mu}} \times \boldsymbol{\mathcal{I}}, \text{ and for } e = 1, \dots, \mathtt{n_{el}}, \\ \nabla_{\boldsymbol{\mu}} \cdot \left(\boldsymbol{L}_e + p_e \mathbf{I}_{\mathtt{n_{sd}}} \right) = \boldsymbol{s} & \text{in } \Omega_e^{\boldsymbol{\mu}} \times \boldsymbol{\mathcal{I}}, \text{ and for } e = 1, \dots, \mathtt{n_{el}}, \\ \nabla_{\boldsymbol{\mu}} \cdot \boldsymbol{u}_e = 0 & \text{in } \Omega_e^{\boldsymbol{\mu}} \times \boldsymbol{\mathcal{I}}, \text{ and for } e = 1, \dots, \mathtt{n_{el}}, \\ \boldsymbol{u}_e = \boldsymbol{u}_D & \text{on } \left(\partial \Omega_e^{\boldsymbol{\mu}} \cap \Gamma_D^{\boldsymbol{\mu}} \right) \times \boldsymbol{\mathcal{I}}, \\ \boldsymbol{u}_e = \hat{\boldsymbol{u}} & \text{on } \left(\partial \Omega_e^{\boldsymbol{\mu}} \setminus \Gamma_D^{\boldsymbol{\mu}} \right) \times \boldsymbol{\mathcal{I}}, \\ \left\langle \dfrac{1}{|\partial \Omega_e^{\boldsymbol{\mu}}|} p_e, 1 \right\rangle_{\partial \Omega_e^{\boldsymbol{\mu}} \times \boldsymbol{\mathcal{I}}} = \rho_e, & \text{for } e = 1, \dots, \mathtt{n_{el}}, \end{cases} \tag{12}$$

where $\hat{\boldsymbol{u}}$ is the so-called hybrid variable, which is an independent variable representing the trace of the solution on the element faces, and ρ_e is the mean value of the pressure on the boundary $\partial \Omega_e$. It is worth noting that the local problem is a pure Dirichlet problem and therefore, the last condition in Eq. (12) is introduced to ensure the uniqueness of the pressure. The local problems can be solved independently, element by element, to write $\boldsymbol{L}_e$, $\boldsymbol{u}_e$ and p_e in terms of $\hat{\boldsymbol{u}}$ and ρ_e along the interface $\Gamma^{\boldsymbol{\mu}} \cup \Gamma_N^{\boldsymbol{\mu}} \cup \Gamma_S^{\boldsymbol{\mu}}$.

Second, the so-called *global problem* is defined to impose the continuity of the normal flux on the inter-element faces and the Neumann and slip boundary conditions, namely

$$\begin{cases} [\![\boldsymbol{n}^{\boldsymbol{\mu}} \cdot \left(\boldsymbol{L} + p \mathbf{I}_{\mathtt{n_{sd}}} \right)]\!] = \boldsymbol{0} & \text{on } \Gamma^{\boldsymbol{\mu}} \times \boldsymbol{\mathcal{I}}, \\ \boldsymbol{n}^{\boldsymbol{\mu}} \cdot \left(\boldsymbol{L}_e + p_e \mathbf{I}_{\mathtt{n_{sd}}} \right) = -\boldsymbol{g}_N & \text{on } \left(\partial \Omega_e^{\boldsymbol{\mu}} \cap \Gamma_N^{\boldsymbol{\mu}} \right) \times \boldsymbol{\mathcal{I}}, \\ \boldsymbol{u}_e \cdot \boldsymbol{D}^{\boldsymbol{\mu}} - \boldsymbol{n}^{\boldsymbol{\mu}} \cdot \left(\boldsymbol{L}_e + p_e \mathbf{I}_{\mathtt{n_{sd}}} \right) \boldsymbol{E}^{\boldsymbol{\mu}} = \boldsymbol{0} & \text{on } \left(\partial \Omega_e^{\boldsymbol{\mu}} \cap \Gamma_S^{\boldsymbol{\mu}} \right) \times \boldsymbol{\mathcal{I}}. \end{cases} \tag{13}$$

It is worth noting that, due to the unique definition of the hybrid variable on each face and the Dirichlet boundary condition in the local problems, there is no need to enforce the continuity of the solution in the global problem.

The constraint of Eq. (5), induced by the incompressibility condition, is also considered in the global problem and written in terms of the hybrid variable as

$$\langle 1, \boldsymbol{u}_D \cdot \boldsymbol{n}^{\boldsymbol{\mu}} \rangle_{\Gamma_D^{\boldsymbol{\mu}} \times \boldsymbol{\mathcal{I}}} + \langle 1, \hat{\boldsymbol{u}} \cdot \boldsymbol{n}^{\boldsymbol{\mu}} \rangle_{(\partial \Omega^{\boldsymbol{\mu}} \setminus \Gamma_D^{\boldsymbol{\mu}}) \times \boldsymbol{\mathcal{I}}} = 0. \tag{14}$$

3.3. Weak form of the local and global problems

The following discrete functional spaces are introduced:

$$\begin{aligned}
\mathcal{V}^h(\Omega^{\boldsymbol{\mu}}) &:= \{v \in \mathcal{L}_2(\Omega^{\boldsymbol{\mu}}) : v|_{\Omega_e^{\boldsymbol{\mu}}} \in \mathcal{P}^k(\Omega_e^{\boldsymbol{\mu}})\ \forall \Omega_e^{\boldsymbol{\mu}},\ e = 1, \dots, \mathtt{n_{el}}\},\\
\widehat{\mathcal{V}}^h(S) &:= \{\hat{v} \in [\mathcal{L}_2(S)]^{\mathtt{n_{sd}}} : \hat{v}|_{\Gamma_i^{\boldsymbol{\mu}}} \in \mathcal{P}^k(\Gamma_i^{\boldsymbol{\mu}})\ \forall \Gamma_i^{\boldsymbol{\mu}} \subset S \subseteq \Gamma^{\boldsymbol{\mu}} \cup \partial \Omega^{\boldsymbol{\mu}}\},\\
\mathcal{L}^h(\mathcal{I}^j) &:= \{v \in \mathcal{L}_2(\mathcal{I}^j) : v|_{\mathcal{I}_e^j} \in \mathcal{P}^k(\mathcal{I}_e^j)\ \forall \mathcal{I}_e^j,\ e = 1, \dots, \mathtt{n}_{\mathtt{el}}^j\},\\
\boldsymbol{\mathcal{L}}^h(\boldsymbol{\mathcal{I}}) &:= \mathcal{L}^h(\mathcal{I}^1) \otimes \cdots \otimes \mathcal{L}^h(\mathcal{I}^{\mathtt{n_{pa}}}),\\
\mathcal{V}_{\boldsymbol{\mu}}^h &:= \mathcal{V}^h(\Omega^{\boldsymbol{\mu}}) \otimes \boldsymbol{\mathcal{L}}^h(\boldsymbol{\mathcal{I}}),\\
\widehat{\boldsymbol{\mathcal{V}}}_{\boldsymbol{\mu}}^h &:= \left[\widehat{\mathcal{V}}^h(\Gamma^{\boldsymbol{\mu}} \cup \Gamma_N^{\boldsymbol{\mu}} \cup \Gamma_S^{\boldsymbol{\mu}}) \otimes \boldsymbol{\mathcal{L}}^h(\boldsymbol{\mathcal{I}})\right]^{\mathtt{n_{sd}}},\\
\boldsymbol{\mathcal{V}}_{\boldsymbol{\mu}}^h &:= \left[\mathcal{V}^h(\Omega^{\boldsymbol{\mu}}) \otimes \boldsymbol{\mathcal{L}}^h(\boldsymbol{\mathcal{I}})\right]^{\mathtt{n_{sd}}},\\
\boldsymbol{\mathcal{W}}_{\boldsymbol{\mu}}^h &:= \left[\mathcal{V}^h(\Omega^{\boldsymbol{\mu}}) \otimes \boldsymbol{\mathcal{L}}^h(\boldsymbol{\mathcal{I}})\right]^{\mathtt{n_{sd}} \times \mathtt{n_{sd}}},
\end{aligned}$$

where $\mathcal{P}^k(\Omega_e^{\boldsymbol{\mu}})$, $\mathcal{P}^k(\Gamma_i^{\boldsymbol{\mu}})$ and $\mathcal{P}^k(\mathcal{I}_e^j)$ stand for the spaces of polynomial functions of complete degree at most k in $\Omega_e^{\boldsymbol{\mu}}$, on $\Gamma_i^{\boldsymbol{\mu}}$ and in $\mathcal{I}_e^j$ respectively.

The weak form of the local problems, for $e = 1, \dots, \mathtt{n_{el}}$, reads: given $\boldsymbol{u}_D$ on $\Gamma_D^{\boldsymbol{\mu}}$ and $\hat{\boldsymbol{u}}^h$ on $\Gamma^{\boldsymbol{\mu}} \cup \Gamma_N^{\boldsymbol{\mu}} \cup \Gamma_S^{\boldsymbol{\mu}}$, find $(\boldsymbol{L}_e^h, \boldsymbol{u}_e^h, p_e^h) \in \boldsymbol{\mathcal{W}}_{\boldsymbol{\mu}}^h \times \boldsymbol{\mathcal{V}}_{\boldsymbol{\mu}}^h \times \mathcal{V}_{\boldsymbol{\mu}}^h$ that satisfy

$$\begin{aligned}
A_{LL}(\boldsymbol{W}, \boldsymbol{L}_e^h) + A_{Lu}(\boldsymbol{W}, \boldsymbol{u}_e^h) &= L_L(\boldsymbol{W}) + A_{L\hat{u}}(\boldsymbol{W}, \hat{\boldsymbol{u}}^h),\\
A_{uL}(\boldsymbol{v}, \boldsymbol{L}_e^h) + A_{uu}(\boldsymbol{v}, \boldsymbol{u}_e^h) + A_{up}(\boldsymbol{v}, p_e^h) &= L_u(\boldsymbol{v}) + A_{u\hat{u}}(\boldsymbol{v}, \hat{\boldsymbol{u}}^h),\\
A_{pu}(v, \boldsymbol{u}_e^h) &= L_p(v) + A_{p\hat{u}}(v, \hat{\boldsymbol{u}}^h),\\
A_{\rho p}(1, p_e^h) &= A_{\rho\rho}(1, \rho_e^h),
\end{aligned} \tag{15}$$

for all $(\boldsymbol{W}, \boldsymbol{v}, v) \in \boldsymbol{\mathcal{W}}_{\boldsymbol{\mu}}^h \times \boldsymbol{\mathcal{V}}_{\boldsymbol{\mu}}^h \times \mathcal{V}_{\boldsymbol{\mu}}^h$, where the multi-dimensional bilinear and linear forms of the local problem are given by

$$\begin{aligned}
A_{LL}(\boldsymbol{W}, \boldsymbol{L}) &:= -\left(\boldsymbol{W}, \nu^{-1}\boldsymbol{L}\right)_{\Omega_e^{\boldsymbol{\mu}} \times \boldsymbol{\mathcal{I}}}, & A_{Lu}(\boldsymbol{W}, \boldsymbol{u}) &:= \left(\nabla_{\boldsymbol{\mu}} \cdot \boldsymbol{W}, \boldsymbol{u}\right)_{\Omega_e^{\boldsymbol{\mu}} \times \boldsymbol{\mathcal{I}}},\\
A_{L\hat{u}}(\boldsymbol{W}, \hat{\boldsymbol{u}}) &:= \langle \boldsymbol{n}^{\boldsymbol{\mu}} \cdot \boldsymbol{W}, \hat{\boldsymbol{u}} \rangle_{(\partial \Omega_e^{\boldsymbol{\mu}} \setminus \Gamma_D^{\boldsymbol{\mu}}) \times \boldsymbol{\mathcal{I}}}, & A_{uL}(\boldsymbol{v}, \boldsymbol{L}) &:= \left(\boldsymbol{v}, \nabla_{\boldsymbol{\mu}} \cdot \boldsymbol{L}\right)_{\Omega_e^{\boldsymbol{\mu}} \times \boldsymbol{\mathcal{I}}},\\
A_{uu}(\boldsymbol{v}, \boldsymbol{u}) &:= \langle \boldsymbol{v}, \boldsymbol{\tau}^{\boldsymbol{\mu}} \boldsymbol{u} \rangle_{\partial \Omega_e^{\boldsymbol{\mu}} \times \boldsymbol{\mathcal{I}}}, & A_{up}(\boldsymbol{v}, p) &:= \left(\boldsymbol{v}, \nabla_{\boldsymbol{\mu}} p\right)_{\Omega_e^{\boldsymbol{\mu}} \times \boldsymbol{\mathcal{I}}},\\
A_{u\hat{u}}(\boldsymbol{v}, \hat{\boldsymbol{u}}) &:= \langle \boldsymbol{v}, \boldsymbol{\tau}^{\boldsymbol{\mu}} \hat{\boldsymbol{u}} \rangle_{(\partial \Omega_e^{\boldsymbol{\mu}} \setminus \Gamma_D^{\boldsymbol{\mu}}) \times \boldsymbol{\mathcal{I}}}, & A_{pu}(v, \boldsymbol{u}) &:= \left(\nabla_{\boldsymbol{\mu}} v, \boldsymbol{u}\right)_{\Omega_e^{\boldsymbol{\mu}} \times \boldsymbol{\mathcal{I}}},\\
A_{p\hat{u}}(v, \hat{\boldsymbol{u}}) &:= \langle v, \hat{\boldsymbol{u}} \cdot \boldsymbol{n}^{\boldsymbol{\mu}} \rangle_{(\partial \Omega_e^{\boldsymbol{\mu}} \setminus \Gamma_D^{\boldsymbol{\mu}}) \times \boldsymbol{\mathcal{I}}}, & A_{\rho p}(w, p) &:= \langle w, |\partial \Omega_e^{\boldsymbol{\mu}}|^{-1} p \rangle_{\partial \Omega_e^{\boldsymbol{\mu}} \times \boldsymbol{\mathcal{I}}},\\
A_{\rho\rho}(w, \rho) &:= \left(w, \rho\right)_{\boldsymbol{\mathcal{I}}}, &&
\end{aligned} \tag{16}$$

and

$$\begin{aligned}
L_L(\boldsymbol{W}) &:= \langle \boldsymbol{n}^{\boldsymbol{\mu}} \cdot \boldsymbol{W}, \boldsymbol{u}_D \rangle_{(\partial \Omega_e^{\boldsymbol{\mu}} \cap \Gamma_D^{\boldsymbol{\mu}}) \times \boldsymbol{\mathcal{I}}}, \quad L_u(\boldsymbol{v}) := \left(\boldsymbol{v}, \boldsymbol{s}\right)_{\Omega_e^{\boldsymbol{\mu}} \times \boldsymbol{\mathcal{I}}} + \langle \boldsymbol{v}, \boldsymbol{\tau}^{\boldsymbol{\mu}} \boldsymbol{u}_D \rangle_{(\partial \Omega_e^{\boldsymbol{\mu}} \cap \Gamma_D^{\boldsymbol{\mu}}) \times \boldsymbol{\mathcal{I}}},\\
L_p(v) &:= \langle v, \boldsymbol{u}_D \cdot \boldsymbol{n}^{\boldsymbol{\mu}} \rangle_{(\partial \Omega_e^{\boldsymbol{\mu}} \cap \Gamma_D^{\boldsymbol{\mu}}) \times \boldsymbol{\mathcal{I}}},
\end{aligned} \tag{17}$$

respectively, where $(\cdot, \cdot)_D$ denotes the standard $\mathcal{L}_2$ scalar product in a generic subdomain D and $\boldsymbol{\tau}^{\boldsymbol{\mu}}$ is the stabilisation tensor, whose selection has an important influence on the accuracy, stability and convergence properties

of the resulting HDG method [21,38,42,43]. The choice of the stabilisation tensor for geometrically parametrised problems will be discussed in the next section.

Similarly, the weak form of the global problem is: find $\hat{\boldsymbol{u}}^h \in \widehat{\boldsymbol{\mathcal{V}}}^h_{\boldsymbol{\mu}}$ and $\rho^h \in \mathbb{R}^{\mathtt{n_{el}}} \otimes \boldsymbol{\mathcal{L}}^h(\boldsymbol{\mathcal{I}})$ that satisfies

$$\begin{aligned}\sum_{e=1}^{\mathtt{n_{el}}} \left\{ A_{\hat{u}L}(\hat{\boldsymbol{v}}, \boldsymbol{L}^h_e) + A_{\hat{u}u}(\hat{\boldsymbol{v}}, \boldsymbol{u}^h_e) + A_{\hat{u}p}(\hat{\boldsymbol{v}}, p^h_e) + A_{\hat{u}\hat{u}}(\hat{\boldsymbol{v}}, \hat{\boldsymbol{u}}^h) \right\} &= \sum_{e=1}^{\mathtt{n_{el}}} \left\{ L_{\hat{u}}(\hat{\boldsymbol{v}}) \right\}, \\ A_{p\hat{u}}(1, \hat{\boldsymbol{u}}^h) &= -L_p(1),\end{aligned} \tag{18}$$

for all $\hat{\boldsymbol{v}} \in \widehat{\boldsymbol{\mathcal{V}}}^h_{\boldsymbol{\mu}}$, where the multi-dimensional bilinear and linear forms of the global problem are given by

$$\begin{aligned} A_{\hat{u}L}(\hat{\boldsymbol{v}}, \boldsymbol{L}) &:= \langle \hat{\boldsymbol{v}}, \boldsymbol{n}^{\boldsymbol{\mu}} \cdot \boldsymbol{L} \rangle_{(\partial\Omega^{\boldsymbol{\mu}}_e \setminus (\Gamma^{\boldsymbol{\mu}}_D \cup \Gamma^{\boldsymbol{\mu}}_S)) \times \boldsymbol{\mathcal{I}}} - \langle \hat{\boldsymbol{v}}, \boldsymbol{n}^{\boldsymbol{\mu}} \cdot \boldsymbol{L}\boldsymbol{E}^{\boldsymbol{\mu}} \rangle_{(\partial\Omega^{\boldsymbol{\mu}}_e \cap \Gamma^{\boldsymbol{\mu}}_S) \times \boldsymbol{\mathcal{I}}} \\ A_{\hat{u}u}(\hat{\boldsymbol{v}}, \boldsymbol{u}) &:= \langle \hat{\boldsymbol{v}}, \boldsymbol{\tau}^{\boldsymbol{\mu}} \boldsymbol{u} \rangle_{(\partial\Omega^{\boldsymbol{\mu}}_e \setminus (\Gamma^{\boldsymbol{\mu}}_D \cup \Gamma^{\boldsymbol{\mu}}_S)) \times \boldsymbol{\mathcal{I}}} - \langle \hat{\boldsymbol{v}}, (\boldsymbol{\tau}^{\boldsymbol{\mu}} \boldsymbol{u}) \cdot \boldsymbol{E}^{\boldsymbol{\mu}} \rangle_{(\partial\Omega^{\boldsymbol{\mu}}_e \cap \Gamma^{\boldsymbol{\mu}}_S) \times \boldsymbol{\mathcal{I}}} \\ A_{\hat{u}p}(\hat{\boldsymbol{v}}, p) &:= \langle \hat{\boldsymbol{v}}, p\boldsymbol{n}^{\boldsymbol{\mu}} \rangle_{(\partial\Omega^{\boldsymbol{\mu}}_e \setminus (\Gamma^{\boldsymbol{\mu}}_D \cup \Gamma^{\boldsymbol{\mu}}_S)) \times \boldsymbol{\mathcal{I}}} \\ A_{\hat{u}\hat{u}}(\hat{\boldsymbol{v}}, \hat{\boldsymbol{u}}) &:= -\langle \hat{\boldsymbol{v}}, \boldsymbol{\tau}^{\boldsymbol{\mu}} \hat{\boldsymbol{u}} \rangle_{(\partial\Omega^{\boldsymbol{\mu}}_e \setminus (\Gamma^{\boldsymbol{\mu}}_D \cup \Gamma^{\boldsymbol{\mu}}_S)) \times \boldsymbol{\mathcal{I}}} + \langle \hat{\boldsymbol{v}}, \hat{\boldsymbol{u}} \cdot \boldsymbol{D}^{\boldsymbol{\mu}} + (\boldsymbol{\tau}^{\boldsymbol{\mu}} \hat{\boldsymbol{u}}) \cdot \boldsymbol{E}^{\boldsymbol{\mu}} \rangle_{(\partial\Omega^{\boldsymbol{\mu}}_e \cap \Gamma^{\boldsymbol{\mu}}_S) \times \boldsymbol{\mathcal{I}}} \end{aligned} \tag{19}$$

and

$$L_{\hat{u}}(\hat{\boldsymbol{v}}) := -\langle \hat{\boldsymbol{v}}, \boldsymbol{g}_N \rangle_{(\partial\Omega^{\boldsymbol{\mu}}_e \cap \Gamma^{\boldsymbol{\mu}}_N) \times \boldsymbol{\mathcal{I}}}, \tag{20}$$

respectively.

The local problem of Eq. (15) is used to write the velocity, $\boldsymbol{u}_e$, pressure, p_e, and gradient of the velocity $\boldsymbol{L}_e$, as a function of the hybrid variable, $\hat{u}$, and the mean value of the pressure in each element, ρ_e. Inserting these expressions in the global problem of Eq. (18) leads to a global problem with $\hat{u}$, and ρ being the only unknowns. Once the global problem is solved, the local problem can be solved, element-by-element, to retrieve the velocity, pressure and the gradient of the velocity in each element.

4. The proper generalised decomposition strategy

The solution of the parametric problem of dimension $\mathtt{n_{sd}} + \mathtt{n_{pa}}$, presented in the previous section, with the standard HDG approach is usually not affordable, even for a relatively small number of parameters. To circumvent the *curse of dimensionality*, this section proposes the use of the PGD framework. As it will be shown in this section, the use of an HDG formulation has important advantages compared to other formulations such as standard finite elements [19].

To simplify the presentation, the subindex $_e$ and the superindex ^{h} used in the previous section to specify the element and the discrete approximations will be omitted here, unless they are needed to follow the development.

4.1. Separated spatial mapping to obtain generalised solutions

As discussed in detail in [19,44,45], the solution of the parametric problem described in Section 3 requires that the bilinear and linear forms in the weak form can be expressed, or well approximated, by a sum of products of parametric functions and operators that are parameter-independent. To enforce the affine parameter dependence, the integrals appearing in the weak form must involve domains that are not dependent upon the parameters. Following the work of [16,17,19], a mapping between a parameter-independent reference domain, Ω, and the geometrically parametrised domain is considered, namely

$$\begin{aligned} \boldsymbol{\mathcal{M}}_{\boldsymbol{\mu}} &: \Omega \times \boldsymbol{\mathcal{I}} \longrightarrow \Omega^{\boldsymbol{\mu}} \\ &(\boldsymbol{x}, \boldsymbol{\mu}) \longmapsto \boldsymbol{x}^{\boldsymbol{\mu}} = \boldsymbol{\mathcal{M}}_{\boldsymbol{\mu}}(\boldsymbol{x}, \boldsymbol{\mu}). \end{aligned} \tag{21}$$

The coordinates of the reference, or *undeformed*, domain are denoted by $\boldsymbol{x}$ whereas the coordinates of the parametric, or *deformed*, domain are denoted by $\boldsymbol{x}^{\boldsymbol{\mu}}$. To ensure the affine parameter dependence, the mapping is assumed to be given in separated form as

$$\boldsymbol{\mathcal{M}}_{\boldsymbol{\mu}}(\boldsymbol{x}, \boldsymbol{\mu}) = \sum_{k=1}^{\mathtt{n_M}} \mathbf{M}^k(\boldsymbol{x}) \phi^k(\boldsymbol{\mu}), \tag{22}$$

where $\mathtt{n_M}$ is the number of terms required to express the mapping in a separable form.

Remark 1. To simplify the presentation here, it is assumed that the separated representation of the mapping is given analytically. As mentioned earlier, a general strategy to construct a separable mapping was described in [19] using an exact boundary description of the computational domain by means of NURBS.

The separated representation of the mapping leads to the following separated representation of its Jacobian

$$\mathbf{J}_{\boldsymbol{\mu}}(\boldsymbol{x},\boldsymbol{\mu}) = \frac{\partial \boldsymbol{x}^{\boldsymbol{\mu}}}{\partial \boldsymbol{x}}(\boldsymbol{x},\boldsymbol{\mu}) = \sum_{k=1}^{\mathtt{n_M}} \mathbf{J}^k(\boldsymbol{x})\phi^k(\boldsymbol{\mu}). \tag{23}$$

In addition, the separated description of the mapping and its Jacobian can be used to obtain a separated expression of the determinant and the adjoint of the Jacobian using the Leibniz formula and the Leverrier's algorithm as explained in detail in [19]. The separated expression of the determinant of the Jacobian and its adjoint are written in compact form as

$$\det(\mathbf{J}_{\boldsymbol{\mu}})(\boldsymbol{x},\boldsymbol{\mu}) = \sum_{k=1}^{\mathtt{n_d}} D^k(\boldsymbol{x})\theta^k(\boldsymbol{\mu}) \tag{24}$$

and

$$\operatorname{adj}(\mathbf{J}_{\boldsymbol{\mu}})(\boldsymbol{x},\boldsymbol{\mu}) = \sum_{k=1}^{\mathtt{n_a}} \mathbf{A}^k(\boldsymbol{x})\vartheta^k(\boldsymbol{\mu}), \tag{25}$$

respectively.

It is worth noting that the number of terms required to write the determinant and the adjoint in a separated form, $\mathtt{n_d}$ and $\mathtt{n_a}$ respectively, is higher than the number of terms required to describe the mapping in a separated form $\mathtt{n_M}$.

4.2. Affine parameter dependence of the HDG bilinear and linear forms

Introducing the mapping $\boldsymbol{\mathcal{M}}_{\boldsymbol{\mu}}$ of Eq. (21) into the weak form of the local and global problems, it is possible to write the integrals over the reference domain, Ω, and its boundary, $\partial\Omega$, not dependent on the parameters $\boldsymbol{\mu}$. The bilinear and linear forms for the local problems can be written as

$$\begin{aligned}
A_{LL}(\boldsymbol{W},\boldsymbol{L}) &= -\left(\boldsymbol{W}, \nu^{-1}\det(\mathbf{J}_{\boldsymbol{\mu}})\boldsymbol{L}\right)_{\Omega_e\times\boldsymbol{\mathcal{I}}}, & A_{Lu}(\boldsymbol{W},\boldsymbol{u}) &= \left(\operatorname{adj}(\mathbf{J}_{\boldsymbol{\mu}})\boldsymbol{\nabla}\cdot\boldsymbol{W},\boldsymbol{u}\right)_{\Omega_e\times\boldsymbol{\mathcal{I}}},\\
A_{L\hat{u}}(\boldsymbol{W},\hat{\boldsymbol{u}}) &= \langle \operatorname{adj}(\mathbf{J}_{\boldsymbol{\mu}})\boldsymbol{n}\cdot\boldsymbol{W},\hat{\boldsymbol{u}}\rangle_{(\partial\Omega_e\setminus\Gamma_D)\times\boldsymbol{\mathcal{I}}}, & A_{uL}(\boldsymbol{v},\boldsymbol{L}) &= \left(\boldsymbol{v},\operatorname{adj}(\mathbf{J}_{\boldsymbol{\mu}})\boldsymbol{\nabla}\cdot\boldsymbol{L}\right)_{\Omega_e\times\boldsymbol{\mathcal{I}}},\\
A_{uu}(\boldsymbol{v},\boldsymbol{u}) &= \langle \boldsymbol{v},\boldsymbol{\tau}\boldsymbol{u}\rangle_{\partial\Omega_e\times\boldsymbol{\mathcal{I}}}, & A_{up}(\boldsymbol{v},p) &= \left(\boldsymbol{v},\operatorname{adj}(\mathbf{J}_{\boldsymbol{\mu}})\boldsymbol{\nabla}p\right)_{\Omega_e\times\boldsymbol{\mathcal{I}}},\\
A_{u\hat{u}}(\boldsymbol{v},\hat{\boldsymbol{u}}) &= \langle \boldsymbol{v},\boldsymbol{\tau}\hat{\boldsymbol{u}}\rangle_{(\partial\Omega_e\setminus\Gamma_D)\times\boldsymbol{\mathcal{I}}}, & A_{pu}(v,\boldsymbol{u}) &= \left(\operatorname{adj}(\mathbf{J}_{\boldsymbol{\mu}})\boldsymbol{\nabla}v,\boldsymbol{u}\right)_{\Omega_e\times\boldsymbol{\mathcal{I}}},\\
A_{p\hat{u}}(v,\hat{\boldsymbol{u}}) &= \langle v,\hat{\boldsymbol{u}}\cdot\operatorname{adj}(\mathbf{J}_{\boldsymbol{\mu}})\boldsymbol{n}\rangle_{(\partial\Omega_e\setminus\Gamma_D)\times\boldsymbol{\mathcal{I}}}, & A_{\rho p}(w,p) &= \langle w,|\partial\Omega_e|^{-1}p\rangle_{\partial\Omega_e\times\boldsymbol{\mathcal{I}}},\\
A_{\rho\rho}(w,\rho) &= \left(w,\rho\right)_{\boldsymbol{\mathcal{I}}}, & &
\end{aligned} \tag{26}$$

and

$$\begin{aligned}
L_L(\boldsymbol{W}) &= \langle \operatorname{adj}(\mathbf{J}_{\boldsymbol{\mu}})\boldsymbol{n}\cdot\boldsymbol{W},\boldsymbol{u}_D\rangle_{(\partial\Omega_e\cap\Gamma_D)\times\boldsymbol{\mathcal{I}}}, & L_u(\boldsymbol{v}) &= \left(\boldsymbol{v},\det(\mathbf{J}_{\boldsymbol{\mu}})\boldsymbol{s}\right)_{\Omega_e\times\boldsymbol{\mathcal{I}}} + \langle \boldsymbol{v},\boldsymbol{\tau}\boldsymbol{u}_D\rangle_{(\partial\Omega_e\cap\Gamma_D)\times\boldsymbol{\mathcal{I}}},\\
L_p(v) &= \langle v,\boldsymbol{u}_D\cdot\operatorname{adj}(\mathbf{J}_{\boldsymbol{\mu}})\boldsymbol{n}\rangle_{(\partial\Omega_e\cap\Gamma_D)\times\boldsymbol{\mathcal{I}}}, & &
\end{aligned} \tag{27}$$

respectively, where the adjoint operator is defined as $\operatorname{adj}(\boldsymbol{A}) = \det(\boldsymbol{A})\,\boldsymbol{A}^{-1}$ and the stabilisation parameter in the deformed domain is chosen as

$$\boldsymbol{\tau}^{\boldsymbol{\mu}} := \frac{1}{\|\operatorname{adj}(\mathbf{J}_{\boldsymbol{\mu}})\boldsymbol{n}\|}\boldsymbol{\tau}. \tag{28}$$

The scaling factor $\|\operatorname{adj}(\mathbf{J}_{\boldsymbol{\mu}})\boldsymbol{n}\|$ in Eq. (28) accounts for the increased or decreased area of the deformed face, $\partial\Omega_e^{\boldsymbol{\mu}}$, with respect to the reference one, $\partial\Omega_e$. This definition, inspired by the expression of the penalty coefficient in

classical interior penalty DG methods [46], ensures that the larger the deformation of the face, the smaller the value of $\boldsymbol{\tau}^{\boldsymbol{\mu}}$ is. This ensures that a weaker continuity is imposed for large deformations and it is justified by the expected loss of accuracy in the hybrid variable when the mapping introduces a large deformation.

Following previous work on HDG methods for Stokes problems [39], the stabilisation parameter in the reference domain is selected as $\boldsymbol{\tau} = (\tau\nu/\ell)\mathbf{I}_{\mathtt{n_{sd}}}$, where τ is a numerical parameter, selected as $\tau = 10$ in this work, and ℓ is a characteristic length of the domain.

Remark 2. As mentioned above, it holds that $\|\operatorname{adj}(\mathbf{J}_{\boldsymbol{\mu}})\boldsymbol{n}\| = |\partial\Omega_e^{\boldsymbol{\mu}}|/|\partial\Omega_e|$. Hence, no parametric dependence appears in the arguments of the bilinear form $A_{\rho p}$.

Analogously, the bilinear and linear forms for the global problem can be written as

$$\begin{aligned}
A_{\hat{u}L}(\hat{\boldsymbol{v}}, \boldsymbol{L}) &= \langle \hat{\boldsymbol{v}}, \operatorname{adj}(\mathbf{J}_{\boldsymbol{\mu}})\boldsymbol{n} \cdot \boldsymbol{L} \rangle_{(\partial\Omega_e \setminus (\Gamma_D \cup \Gamma_S)) \times \boldsymbol{\mathcal{I}}} - \langle \hat{\boldsymbol{v}}, \operatorname{adj}(\mathbf{J}_{\boldsymbol{\mu}})\boldsymbol{n} \cdot \boldsymbol{L}\boldsymbol{E} \rangle_{(\partial\Omega_e \cap \Gamma_S) \times \boldsymbol{\mathcal{I}}} \\
A_{\hat{u}u}(\hat{\boldsymbol{v}}, \boldsymbol{u}) &= \langle \hat{\boldsymbol{v}}, \boldsymbol{\tau}\boldsymbol{u} \rangle_{(\partial\Omega_e \setminus (\Gamma_D \cup \Gamma_S)) \times \boldsymbol{\mathcal{I}}} - \langle \hat{\boldsymbol{v}}, (\boldsymbol{\tau}\boldsymbol{u}) \cdot \boldsymbol{E} \rangle_{(\partial\Omega_e \cap \Gamma_S) \times \boldsymbol{\mathcal{I}}} \\
A_{\hat{u}p}(\hat{\boldsymbol{v}}, p) &= \langle \hat{\boldsymbol{v}}, p \operatorname{adj}(\mathbf{J}_{\boldsymbol{\mu}})\boldsymbol{n} \rangle_{(\partial\Omega_e \setminus (\Gamma_D \cup \Gamma_S)) \times \boldsymbol{\mathcal{I}}} \\
A_{\hat{u}\hat{u}}(\hat{\boldsymbol{v}}, \hat{\boldsymbol{u}}) &= -\langle \hat{\boldsymbol{v}}, \boldsymbol{\tau}\hat{\boldsymbol{u}} \rangle_{(\partial\Omega_e \setminus (\Gamma_D \cup \Gamma_S)) \times \boldsymbol{\mathcal{I}}} + \langle \hat{\boldsymbol{v}}, \hat{\boldsymbol{u}} \cdot \operatorname{adj}(\mathbf{J}_{\boldsymbol{\mu}})\boldsymbol{D} + (\boldsymbol{\tau}\hat{\boldsymbol{u}}) \cdot \boldsymbol{E} \rangle_{(\partial\Omega_e \cap \Gamma_S) \times \boldsymbol{\mathcal{I}}}
\end{aligned} \tag{29}$$

and

$$L_{\hat{u}}(\hat{\boldsymbol{v}}) = -\langle \hat{\boldsymbol{v}}, \boldsymbol{g}_N \rangle_{(\partial\Omega_e \cap \Gamma_N) \times \boldsymbol{\mathcal{I}}}, \tag{30}$$

respectively.

Remark 3. The derivation of the terms on the slip boundary in (29) follows from the relationship $\langle \hat{\boldsymbol{v}}, \boldsymbol{n}^{\boldsymbol{\mu}} \cdot \boldsymbol{H} \rangle_{(\partial\Omega_e^{\boldsymbol{\mu}} \cap \Gamma_S^{\boldsymbol{\mu}}) \times \boldsymbol{\mathcal{I}}} = \langle \hat{\boldsymbol{v}}, \operatorname{adj}(\mathbf{J}_{\boldsymbol{\mu}})\boldsymbol{n} \cdot \boldsymbol{H} \rangle_{(\partial\Omega_e \cap \Gamma_S) \times \boldsymbol{\mathcal{I}}}$ and the definition (28). The slip boundary condition is used here to enforce a symmetry condition and therefore, it is assumed that the orientation of the vectors $\{\boldsymbol{n}^{\boldsymbol{\mu}}, \boldsymbol{t}_1^{\boldsymbol{\mu}}, \ldots, \boldsymbol{t}_{\mathtt{n_{sd}}-1}^{\boldsymbol{\mu}}\}$ is preserved by the mapping $\boldsymbol{\mathcal{M}}_{\boldsymbol{\mu}}$. It is worth noting that this does not imply that $\Gamma_S^{\boldsymbol{\mu}} = \Gamma_S$ as it will be shown with numerical examples.

Remark 4. As is typical in the context of shape optimisation [47], in (30) it is assumed that Neumann boundaries, where a traction (or pseudo-traction) is imposed, are fixed, that is, $\Gamma_N^{\boldsymbol{\mu}} = \Gamma_N$. On the contrary, deformable Neumann boundaries, also known as *free boundaries*, are traction-free, whence $\boldsymbol{g}_N$ is null.

4.3. Separated representation of the data

As usual in a PGD context, the data is assumed to be given in separated form. For the Stokes problem under consideration, this means that the Dirichlet and Neumann data and the source term can be written as

$$\begin{aligned}
\boldsymbol{u}_D &= \sum_{l=1}^{\mathtt{n_D}} \boldsymbol{g}_D^l(\boldsymbol{x}) \lambda_D^l(\boldsymbol{\mu}), \\
\boldsymbol{g}_N &= \sum_{l=1}^{\mathtt{n_N}} \boldsymbol{g}_N^l(\boldsymbol{x}) \lambda_N^l(\boldsymbol{\mu}), \\
\boldsymbol{s} &= \sum_{l=1}^{\mathtt{n_S}} \boldsymbol{g}_S^l(\boldsymbol{x}) \lambda_S^l(\boldsymbol{\mu}).
\end{aligned} \tag{31}$$

Even if the data is not directly given in this form, it is possible to obtain a good approximation in a separated form, see [6].

4.4. Separated representation of the primal, mixed and hybrid variables

The standard PGD approach consists of assuming a separated representation of all the variables. For instance, for the velocity field, it is assumed that its PGD approximation can be written as

$$\boldsymbol{u}_{\mathtt{PGD}}^m(\boldsymbol{x}, \boldsymbol{\mu}) = \sum_{k=1}^{m} \tilde{\boldsymbol{f}}_u^{\,k}(\boldsymbol{x})\, \tilde{\psi}^k(\boldsymbol{\mu}),$$

where $\tilde{\boldsymbol{f}}_u^{\,k}$ and $\tilde{\psi}^k$ are the kth spatial and parametric modes respectively and the total number of modes is a priori unknown and automatically determined by the algorithm based on a user-defined tolerance, as described in the next section.

In practice, it is advantageous [19] to write the separated approximation as

$$\boldsymbol{u}^m_{\text{PGD}}(\boldsymbol{x},\boldsymbol{\mu}) = \sigma_u^m\, \boldsymbol{f}_u^m(\boldsymbol{x})\, \psi^m(\boldsymbol{\mu}) + \boldsymbol{u}^{m-1}_{\text{PGD}}(\boldsymbol{x},\boldsymbol{\mu}), \tag{32}$$

where $\boldsymbol{f}_u^m$ and ψ^m are the normalised mth spatial and parametric modes, respectively, and σ_u^m is the amplitude of the mth mode, namely $\boldsymbol{f}_u^m := \tilde{\boldsymbol{f}}_u^{\,m}/\|\tilde{\boldsymbol{f}}_u^{\,m}\|$, $\psi^m := \tilde{\psi}^m/\|\tilde{\psi}^m\|$ and $\sigma_u^m := \|\tilde{\boldsymbol{f}}_u^{\,m}\|\|\tilde{\psi}^m\|$.

This alternative expression enables to directly use the amplitude of the modes, σ_u^m, to determine when it is feasible to stop adding new modes. In addition, as explained in detail in the next section, the expression of equation (32) suggests that the modes are computed sequentially. So, assuming that the first $m-1$ modes are known, the next section will focus on detailing how the new mode m is computed.

In this work, the implementation follows the *predictor–corrector* PGD rationale, which has been shown [11] to improve the original algorithm, because it applies the alternating direction method to the Jacobian of the high-dimensional nonlinear problem. This improves the convergence for each mode because it is easier to select the initial prediction and provides a faster convergence.

Each variable of the HDG formulation, presented in Section 3, is written as a rank-m separable approximation, that is

$$\begin{aligned}
\boldsymbol{L}^m_{\text{PGD}}(\boldsymbol{x},\boldsymbol{\mu}) &= \sigma_L^m[\boldsymbol{F}_L^m(\boldsymbol{x})\,\psi^m(\boldsymbol{\mu}) + \Delta\boldsymbol{L}^m_{\text{PGD}}(\boldsymbol{x},\boldsymbol{\mu})] + \boldsymbol{L}^{m-1}_{\text{PGD}}(\boldsymbol{x},\boldsymbol{\mu}),\\
\boldsymbol{u}^m_{\text{PGD}}(\boldsymbol{x},\boldsymbol{\mu}) &= \sigma_u^m[\boldsymbol{f}_u^m(\boldsymbol{x})\,\psi^m(\boldsymbol{\mu}) + \Delta\boldsymbol{u}^m_{\text{PGD}}(\boldsymbol{x},\boldsymbol{\mu})] + \boldsymbol{u}^{m-1}_{\text{PGD}}(\boldsymbol{x},\boldsymbol{\mu}),\\
p^m_{\text{PGD}}(\boldsymbol{x},\boldsymbol{\mu}) &= \sigma_p^m[f_p^m(\boldsymbol{x})\,\psi^m(\boldsymbol{\mu}) + \Delta p^m_{\text{PGD}}(\boldsymbol{x},\boldsymbol{\mu})] + p^{m-1}_{\text{PGD}}(\boldsymbol{x},\boldsymbol{\mu}),\\
\hat{\boldsymbol{u}}^m_{\text{PGD}}(\boldsymbol{x},\boldsymbol{\mu}) &= \sigma_{\hat{u}}^m[\boldsymbol{f}_{\hat{u}}^m(\boldsymbol{x})\,\psi^m(\boldsymbol{\mu}) + \Delta\hat{\boldsymbol{u}}^m_{\text{PGD}}(\boldsymbol{x},\boldsymbol{\mu})] + \hat{\boldsymbol{u}}^{m-1}_{\text{PGD}}(\boldsymbol{x},\boldsymbol{\mu}),\\
\rho^m_{\text{PGD}}(\boldsymbol{x},\boldsymbol{\mu}) &= \sigma_\rho^m[f_\rho^m(\boldsymbol{x})\,\psi^m(\boldsymbol{\mu}) + \Delta\rho^m_{\text{PGD}}(\boldsymbol{x},\boldsymbol{\mu})] + \rho^{m-1}_{\text{PGD}}(\boldsymbol{x},\boldsymbol{\mu}),
\end{aligned} \tag{33}$$

where $\sigma_L^m\boldsymbol{F}_L^m\psi^m$, $\sigma_u^m\boldsymbol{f}_u^m\psi^m$, $\sigma_p^m f_p^m\psi^m$, $\sigma_{\hat{u}}^m\boldsymbol{f}_{\hat{u}}^m\psi^m$ and $\sigma_\rho^m f_\rho^m\psi^m$ are the predictors of the mth mode in the PGD expansion, whereas $\sigma_L^m\Delta\boldsymbol{L}^m_{\text{PGD}}$, $\sigma_u^m\Delta\boldsymbol{u}^m_{\text{PGD}}$, $\sigma_p^m\Delta p^m_{\text{PGD}}$, $\sigma_{\hat{u}}^m\Delta\hat{\boldsymbol{u}}^m_{\text{PGD}}$ and $\sigma_\rho^m\Delta\rho^m_{\text{PGD}}$ are the corresponding correction terms. Introducing the variation Δ, the correctors are defined as

$$\begin{aligned}
\Delta\boldsymbol{L}^m_{\text{PGD}}(\boldsymbol{x},\boldsymbol{\mu}) &:= \Delta\boldsymbol{F}_L(\boldsymbol{x})\,\psi^m(\boldsymbol{\mu}) + \boldsymbol{F}_L^m(\boldsymbol{x})\,\Delta\psi(\boldsymbol{\mu}) + \Delta\boldsymbol{F}_L(\boldsymbol{x})\,\Delta\psi(\boldsymbol{\mu}),\\
\Delta\boldsymbol{u}^m_{\text{PGD}}(\boldsymbol{x},\boldsymbol{\mu}) &:= \Delta\boldsymbol{f}_u(\boldsymbol{x})\,\psi^m(\boldsymbol{\mu}) + \boldsymbol{f}_u^m(\boldsymbol{x})\,\Delta\psi(\boldsymbol{\mu}) + \Delta\boldsymbol{f}_u(\boldsymbol{x})\,\Delta\psi(\boldsymbol{\mu}),\\
\Delta p^m_{\text{PGD}}(\boldsymbol{x},\boldsymbol{\mu}) &:= \Delta f_p(\boldsymbol{x})\,\psi^m(\boldsymbol{\mu}) + f_p^m(\boldsymbol{x})\,\Delta\psi(\boldsymbol{\mu}) + \Delta f_p(\boldsymbol{x})\,\Delta\psi(\boldsymbol{\mu}),\\
\Delta\hat{\boldsymbol{u}}^m_{\text{PGD}}(\boldsymbol{x},\boldsymbol{\mu}) &:= \Delta\boldsymbol{f}_{\hat{u}}(\boldsymbol{x})\,\psi^m(\boldsymbol{\mu}) + \boldsymbol{f}_{\hat{u}}^m(\boldsymbol{x})\,\Delta\psi(\boldsymbol{\mu}) + \Delta\boldsymbol{f}_{\hat{u}}(\boldsymbol{x})\,\Delta\psi(\boldsymbol{\mu}),\\
\Delta\rho^m_{\text{PGD}}(\boldsymbol{x},\boldsymbol{\mu}) &:= \Delta f_\rho(\boldsymbol{x})\,\psi^m(\boldsymbol{\mu}) + f_\rho^m(\boldsymbol{x})\,\Delta\psi(\boldsymbol{\mu}) + \Delta f_\rho(\boldsymbol{x})\,\Delta\psi(\boldsymbol{\mu}),
\end{aligned} \tag{34}$$

where the last term denotes a high-order variation and it is henceforth neglected.

Each term, or *mode*, of the PGD approximation is the product of a function that depends upon the spatial coordinates and a function that depends upon the parameters. In addition, the parametric functions are assumed to be the product of functions that depend upon a single parameter, namely

$$\psi^m(\boldsymbol{\mu}) = \prod_{j=1}^{\mathtt{n_{pa}}} \psi_j^m(\mu_j). \tag{35}$$

Remark 5. This work considers the so-called *single-parameter* approach, where the parametric function of the mth mode, ψ^m, is the same for all the variables. Other approaches, including a different parametric function for each variable or even the use of vector-valued parametric functions in the approximation of vector fields are discussed in [48]. It is worth noting that using the same parametric function for all the variables is particularly beneficial in the context of HDG due to the large number of functions involved, not only velocity and pressure but also the trace of the velocity, the velocity gradient and the mean value of the pressure.

The tangent manifold for $\boldsymbol{L}$ is characterised by choosing $\boldsymbol{W}$ as variations of $\boldsymbol{F}_L\psi$, that is

$$\boldsymbol{W} = \delta\boldsymbol{F}_L\psi^m + \sigma_L^m\boldsymbol{F}_L^m\delta\psi, \tag{36}$$

for $\delta\boldsymbol{F}_L \in \boldsymbol{\mathcal{W}}^h := \left[\mathcal{V}^h(\Omega)\right]^{\mathtt{n_{sd}}\times\mathtt{n_{sd}}}$ and $\delta\psi \in \boldsymbol{\mathcal{L}}^h(\mathcal{I})$. Similarly, the tangent manifolds for $\boldsymbol{u}$, p, $\hat{\boldsymbol{u}}$ and ρ are characterised by choosing

$$\begin{aligned}
\boldsymbol{v} &= \delta\boldsymbol{f}_u\psi^m + \sigma_u^m\boldsymbol{f}_u^m\delta\psi, \quad v = \delta f_p\psi^m + \sigma_p^m f_p^m\delta\psi,\\
\hat{\boldsymbol{v}} &= \delta\boldsymbol{f}_{\hat{u}}\psi^m + \sigma_{\hat{u}}^m\boldsymbol{f}_{\hat{u}}^m\delta\psi, \quad w = \delta f_\rho\psi^m + \sigma_\rho^m f_\rho^m\delta\psi,
\end{aligned} \tag{37}$$

for $\delta\boldsymbol{f}_u \in \boldsymbol{\mathcal{V}}^h := \left[\mathcal{V}^h(\Omega)\right]^{\mathtt{n_{sd}}}$, $\delta f_p \in \mathcal{V}^h$, $\delta\boldsymbol{f}_{\hat{u}} \in \widehat{\boldsymbol{\mathcal{V}}}^h := \left[\widehat{\mathcal{V}}^h(\Gamma\cup\Gamma_N\cup\Gamma_S)\right]^{\mathtt{n_{sd}}}$ and $\delta f_\rho \in \mathbb{R}^{\mathtt{n_{el}}}$.

4.5. Alternating direction scheme

With the separated structure of the PGD approximations, the weighting functions and the bilinear and linear HDG forms described in the previous sections, it is possible to drastically reduce the complexity of the problem. The PGD uses a fixed-point iteration scheme for the high-dimensional nonlinear problem solved with an alternating direction strategy to reduce the computational cost (iterating along low-dimensional problems).

First, in the so-called *spatial iteration*, the parametric function of the mth mode is assumed known and the spatial functions are determined. As it will be shown, this step requires to solve a system of equations with a very similar structure to the non-parametric HDG problem. Second, in the so-called *parametric iteration*, the parametric function is computed using the spatial functions determined in the first step. This process is repeated until convergence is achieved. It is worth noting that the order of the spatial and parametric iterations can be swapped without affecting the alternating direction algorithm.

Let us assume that we have computed the first $m-1$ modes and it is of interest to compute the mth mode. In the next two sections, the alternating direction strategy to compute the spatial and parametric modes is detailed.

4.5.1. The spatial iteration

In the spatial iteration, it is assumed that the parametric function ψ^m and the spatial predictions $\sigma_L^m\boldsymbol{F}_L^m$, $\sigma_u^m\boldsymbol{f}_u^m$, $\sigma_p^m f_p^m$, $\sigma_{\hat{u}}^m\boldsymbol{f}_{\hat{u}}^m$ and $\sigma_\rho^m f_\rho^m$ are known and the goal is to compute the corresponding corrections $\sigma_L^m\Delta\boldsymbol{F}_L$, $\sigma_u^m\Delta\boldsymbol{f}_u$, $\sigma_p^m\Delta f_p$, $\sigma_{\hat{u}}^m\Delta\boldsymbol{f}_{\hat{u}}$ and $\sigma_\rho^m\Delta f_\rho$. As usual in a PGD context, it is assumed that no previous knowledge of the solution is available and therefore, the trivial initial guess of $\psi^m = 1$ is employed for the parametric function.

Taking into account that $\delta\psi = 0$ when ψ^m is known and introducing the expression of the PGD approximations and the weighting functions in the weak form of the HDG local problems, the following weak form of the local problem for the spatial iteration is obtained: find $(\sigma_L^m\Delta\boldsymbol{F}_L, \sigma_u^m\Delta\boldsymbol{f}_u, \sigma_p^m\Delta f_p) \in \boldsymbol{\mathcal{W}}^h\times\boldsymbol{\mathcal{V}}^h\times\mathcal{V}^h$ that satisfy

$$\begin{aligned}
&\sum_{k=1}^{\mathtt{n_d}}\beta_\theta^k\mathcal{A}_{LL}^k(\delta\boldsymbol{F}_L, \sigma_L^m\Delta\boldsymbol{F}_L) + \sum_{k=1}^{\mathtt{n_a}}\beta_\vartheta^k\mathcal{A}_{Lu}^k(\delta\boldsymbol{F}_L, \sigma_u^m\Delta\boldsymbol{f}_u)\\
&\qquad = \mathcal{R}_L^m(\delta\boldsymbol{F}_L\psi^m) + \sum_{k=1}^{\mathtt{n_a}}\beta_\vartheta^k\mathcal{A}_{L\hat{u}}^k(\delta\boldsymbol{F}_L, \sigma_{\hat{u}}^m\Delta\boldsymbol{f}_{\hat{u}}),\\
&\sum_{k=1}^{\mathtt{n_a}}\beta_\vartheta^k\mathcal{A}_{uL}^k(\delta\boldsymbol{f}_u, \sigma_L^m\Delta\boldsymbol{F}_L) + \beta\mathcal{A}_{uu}(\delta\boldsymbol{f}_u, \sigma_u^m\Delta\boldsymbol{f}_u) + \sum_{k=1}^{\mathtt{n_a}}\beta_\vartheta^k\mathcal{A}_{up}^k(\delta\boldsymbol{f}_u, \sigma_p^m\Delta f_p)\\
&\qquad = \mathcal{R}_u^m(\delta\boldsymbol{f}_u\psi^m) + \beta\mathcal{A}_{u\hat{u}}(\delta\boldsymbol{f}_u, \sigma_{\hat{u}}^m\Delta\boldsymbol{f}_{\hat{u}}),\\
&\sum_{k=1}^{\mathtt{n_a}}\beta_\vartheta^k\mathcal{A}_{pu}^k(\delta f_p, \sigma_u^m\Delta\boldsymbol{f}_u) = \mathcal{R}_p^m(\delta f_p\psi^m) + \sum_{k=1}^{\mathtt{n_a}}\beta_\vartheta^k\mathcal{A}_{p\hat{u}}^k(\delta f_p, \sigma_{\hat{u}}^m\Delta\boldsymbol{f}_{\hat{u}})\\
&\qquad \beta\mathcal{A}_{\rho p}^k(1, \sigma_p^m\Delta f_p) = \mathcal{R}_{\overline{p}}^m(\psi^m) + \beta\mathcal{A}_{\rho\rho}(1, \sigma_\rho^m\Delta f_\rho),
\end{aligned} \tag{38}$$

for all $(\delta\boldsymbol{F}_L, \delta\boldsymbol{f}_u, \delta f_p) \in \boldsymbol{\mathcal{W}}^h\times\boldsymbol{\mathcal{V}}^h\times\mathcal{V}^h$.

The bilinear and linear forms of the local problem are detailed in Eq. (A.1), in Appendix A, and Eq. (B.1), in Appendix B, respectively. The constants in Eq. (38) are given by

$$\beta_\theta^k := \mathcal{A}_\theta^k(\psi^m, \psi^m) \qquad \beta_\vartheta^k := \mathcal{A}_\vartheta^k(\psi^m, \psi^m), \qquad \beta := \mathcal{A}(\psi^m, \psi^m), \tag{39}$$

where the bilinear forms involved in the definitions of these constants are introduced in Eq. (A.3), in Appendix A.

As mentioned earlier, in Remark 5, this work considers the same parametric function for all the variables. It is worth noting that this choice reduces the number of different constants in Eq. (38).

Similarly, the weak form of the global problem is: find $\sigma_{\hat{u}}^m \Delta \boldsymbol{f}_{\hat{u}} \in \widehat{\boldsymbol{\mathcal{V}}}^h$ and $\sigma_\rho^m \Delta f_\rho \in \mathbb{R}^{\mathtt{n_{el}}}$ that satisfy

$$\sum_{e=1}^{\mathtt{n_{el}}} \left\{ \sum_{k=1}^{\mathtt{n_a}} \beta_\vartheta^k \mathcal{A}_{\hat{u}L}^k(\delta \boldsymbol{f}_{\hat{u}}, \sigma_L^m \Delta \boldsymbol{F}_L) + \beta \mathcal{A}_{\hat{u}u}(\delta \boldsymbol{f}_{\hat{u}}, \sigma_u^m \Delta \boldsymbol{f}_u) + \sum_{k=1}^{\mathtt{n_a}} \beta_\vartheta^k \mathcal{A}_{\hat{u}p}^k(\delta \boldsymbol{f}_{\hat{u}}, \sigma_p^m \Delta f_p) + \beta \mathcal{A}_{\hat{u}\hat{u}}(\delta \boldsymbol{f}_{\hat{u}}, \quad \sigma_{\hat{u}}^m \Delta \boldsymbol{f}_{\hat{u}}) + \sum_{k=1}^{\mathtt{n_a}} \beta_\vartheta^k \mathcal{A}_{\hat{u}\hat{u}}^k(\delta \boldsymbol{f}_{\hat{u}}, \sigma_{\hat{u}}^m \Delta \boldsymbol{f}_{\hat{u}}) \right\} = \sum_{e=1}^{\mathtt{n_{el}}} \mathcal{R}_{\hat{u}}^m(\delta \boldsymbol{f}_{\hat{u}} \psi^m), \tag{40a}$$

for all $\delta \boldsymbol{f}_{\hat{u}} \in \widehat{\boldsymbol{\mathcal{V}}}^h$, with the incompressibility constraint

$$\sum_{k=1}^{\mathtt{n_a}} \beta_\vartheta^k \mathcal{A}_{p\hat{u}}^k(1, \sigma_{\hat{u}}^m \Delta \boldsymbol{f}_{\hat{u}}) = \mathcal{R}_\rho^m(\psi^m), \quad e = 1, \ldots, \mathtt{n_{el}}. \tag{40b}$$

The bilinear and linear forms of the global problem are detailed in Eq. (A.2), in Appendix A, and Eq. (B.2), in Appendix B, respectively.

4.5.2. The parametric iteration

After computing the spatial corrections following the procedure described in the previous section, the spatial modes are updated, namely

$$\begin{aligned}
\sigma_L^m \boldsymbol{F}_L^m &\leftarrow \sigma_L^m \boldsymbol{F}_L^m + \sigma_L^m \Delta \boldsymbol{F}_L, \\
\sigma_u^m \boldsymbol{f}_u^m &\leftarrow \sigma_u^m \boldsymbol{f}_u^m + \sigma_u^m \Delta \boldsymbol{f}_u, \\
\sigma_p^m f_p^m &\leftarrow \sigma_p^m f_p^m + \sigma_p^m \Delta f_p, \\
\sigma_{\hat{u}}^m \boldsymbol{f}_{\hat{u}}^m &\leftarrow \sigma_{\hat{u}}^m \boldsymbol{f}_{\hat{u}}^m + \sigma_{\hat{u}}^m \Delta \boldsymbol{f}_{\hat{u}}, \\
\sigma_\rho^m f_\rho^m &\leftarrow \sigma_\rho^m f_\rho^m + \sigma_\rho^m \Delta f_\rho,
\end{aligned} \tag{41}$$

where the constant $\sigma_\diamond^m$ on the left hand side denotes the amplitude of the newly computed mth mode of the function $\diamond$, e.g. $\sigma_p^m \leftarrow \|\sigma_p^m f_p^m + \sigma_p^m \Delta f_p\|$.

In the parametric iteration, the goal is to compute the parametric correction $\Delta\psi$ given the prediction ψ^m and the known spatial functions in (41). Following the assumption that such functions are known, it holds that $\delta \boldsymbol{F}_L = \delta \boldsymbol{f}_u = \delta f_p = \delta \boldsymbol{f}_{\hat{u}} = \delta f_\rho = 0$. Introducing the expression of the PGD approximations and the weighting functions in the weak form of the HDG local problems, the following weak form of the local problem for the spatial iteration is obtained: find $\Delta\psi \in \boldsymbol{\mathcal{L}}^h(\boldsymbol{\mathcal{I}})$ such that

$$\begin{aligned}
\sum_{k=1}^{\mathtt{n_d}} \gamma_{LL}^k \mathcal{A}_\vartheta^k(\delta\psi, \Delta\psi) + \sum_{k=1}^{\mathtt{n_a}} \gamma_{Lu}^k \mathcal{A}_\vartheta^k(\delta\psi, \Delta\psi) &= \mathcal{R}_L^m(\sigma_L^m \boldsymbol{F}_L^m \delta\psi) + \sum_{k=1}^{\mathtt{n_a}} \gamma_{L\hat{u}}^k \mathcal{A}_\vartheta^k(\delta\psi, \Delta\psi), \\
\sum_{k=1}^{\mathtt{n_a}} \gamma_{uL}^k \mathcal{A}_\vartheta^k(\delta\psi, \Delta\psi) + \gamma_{uu} \mathcal{A}(\delta\psi, \Delta\psi) + \sum_{k=1}^{\mathtt{n_a}} \gamma_{up}^k \mathcal{A}_\vartheta^k(\delta\psi, \Delta\psi) &= \mathcal{R}_u^m(\sigma_u^m \boldsymbol{f}_u^m \delta\psi) + \gamma_{u\hat{u}} \mathcal{A}(\delta\psi, \psi^m), \\
\sum_{k=1}^{\mathtt{n_a}} \gamma_{pu}^k \mathcal{A}_\vartheta^k(\delta\psi, \Delta\psi) &= \mathcal{R}_p^m(\sigma_p^m f_p^m \delta\psi) + \sum_{k=1}^{\mathtt{n_a}} \gamma_{p\hat{u}}^k \mathcal{A}_\vartheta^k(\delta\psi, \Delta\psi), \\
\gamma_{\rho p} \mathcal{A}(\delta\psi, \Delta\psi) &= \mathcal{R}_{\overline{p}}^m(\delta\psi) + \gamma_{\rho\rho} \mathcal{A}(\delta\psi, \Delta\psi),
\end{aligned} \tag{42}$$

for all $\delta\psi \in \boldsymbol{\mathcal{L}}^h(\boldsymbol{\mathcal{I}})$,

Similarly, the weak form of the global problem is: find $\Delta\psi \in \boldsymbol{\mathcal{L}}^h(\boldsymbol{\mathcal{I}})$ that satisfies

$$\begin{aligned}\sum_{e=1}^{\mathtt{nel}}\Bigg\{\sum_{k=1}^{\mathtt{na}}\gamma_{\hat{u}L}^k\mathcal{A}_\vartheta^k(\delta\psi,\Delta\psi)+\gamma_{\hat{u}u}\mathcal{A}(\delta\psi,\Delta\psi)+\sum_{k=1}^{\mathtt{na}}\gamma_{\hat{u}p}^k\mathcal{A}_\vartheta^k(\delta\psi,\Delta\psi)\\ +\gamma_{\hat{u}\hat{u}}\mathcal{A}(\delta\psi,\Delta\psi)+\sum_{k=1}^{\mathtt{na}}\gamma_{\hat{u}\hat{u}}^k\mathcal{A}_\vartheta^k(\delta\psi,\Delta\psi)\Bigg\}=\sum_{e=1}^{\mathtt{nel}}\mathcal{R}_{\hat{u}}^m(\sigma_{\hat{u}}^m\boldsymbol{f}_{\hat{u}}^m\delta\psi),\\ \sum_{k=1}^{\mathtt{na}}\gamma_{\rho\hat{u}}^k\mathcal{A}_\vartheta^k(\delta\psi,\psi^m)=\mathcal{R}_\rho^m(\delta\psi),\end{aligned}\tag{43}$$

for all $\delta\psi \in \boldsymbol{\mathcal{L}}^h(\boldsymbol{\mathcal{I}})$.

The constants in Eqs. (42) and (43) are defined as

$$\begin{aligned}&\gamma_{LL}^k:=\mathcal{A}_{LL}^k(\sigma_L^m\boldsymbol{F}_L^m,\sigma_L^m\boldsymbol{F}_L^m),\quad &&\gamma_{Lu}^k:=\mathcal{A}_{Lu}^k(\sigma_L^m\boldsymbol{F}_L^m,\sigma_u^m\boldsymbol{f}_u^m),\quad &&\gamma_{L\hat{u}}^k:=\mathcal{A}_{L\hat{u}}^k(\sigma_L^m\boldsymbol{F}_L^m,\sigma_{\hat{u}}^m\boldsymbol{f}_{\hat{u}}^m),\\ &\gamma_{uL}^k:=\mathcal{A}_{uL}^k(\sigma_u^m\boldsymbol{f}_u^m,\sigma_L^m\boldsymbol{F}_L^m),\quad &&\gamma_{uu}:=\mathcal{A}_{uu}(\sigma_u^m\boldsymbol{f}_u^m,\sigma_u^m\boldsymbol{f}_u^m),\quad &&\gamma_{up}^k:=\mathcal{A}_{up}^k(\sigma_u^m\boldsymbol{f}_u^m,\sigma_p^m f_p^m),\\ &\gamma_{u\hat{u}}:=\mathcal{A}_{u\hat{u}}(\sigma_u^m\boldsymbol{f}_u^m,\sigma_{\hat{u}}^m\boldsymbol{f}_{\hat{u}}^m),\quad &&\gamma_{pu}^k:=\mathcal{A}_{pu}^k(\sigma_p^m f_p^m,\sigma_u^m\boldsymbol{f}_u^m),\quad &&\gamma_{p\hat{u}}^k:=\mathcal{A}_{p\hat{u}}^k(\sigma_p^m f_p^m,\sigma_{\hat{u}}^m\boldsymbol{f}_{\hat{u}}^m),\\ &\gamma_{\rho p}:=\mathcal{A}_{\rho p}(1,\sigma_p^m f_p^m),\quad &&\gamma_{\rho\rho}:=\mathcal{A}_{\rho\rho}(1,\sigma_\rho^m f_\rho^m),\quad &&\gamma_{\hat{u}L}^k:=\mathcal{A}_{\hat{u}L}^k(\sigma_{\hat{u}}^m\boldsymbol{f}_{\hat{u}}^m,\sigma_L^m\boldsymbol{F}_L^m),\\ &\gamma_{\hat{u}u}:=\mathcal{A}_{\hat{u}u}(\sigma_{\hat{u}}^m\boldsymbol{f}_{\hat{u}}^m,\sigma_u^m\boldsymbol{f}_u^m),\quad &&\gamma_{\hat{u}p}^k:=\mathcal{A}_{\hat{u}p}^k(\sigma_{\hat{u}}^m\boldsymbol{f}_{\hat{u}}^m,\sigma_p^m f_p^m),\quad &&\gamma_{\hat{u}\hat{u}}:=\mathcal{A}_{\hat{u}\hat{u}}(\sigma_{\hat{u}}^m\boldsymbol{f}_{\hat{u}}^m,\sigma_{\hat{u}}^m\boldsymbol{f}_{\hat{u}}^m),\\ &\gamma_{\hat{u}\hat{u}}^k:=\mathcal{A}_{\hat{u}\hat{u}}^k(\sigma_{\hat{u}}^m\boldsymbol{f}_{\hat{u}}^m,\sigma_{\hat{u}}^m\boldsymbol{f}_{\hat{u}}^m),\quad &&\gamma_{\rho\hat{u}}^k:=\mathcal{A}_{p\hat{u}}^k(1,\sigma_{\hat{u}}^m\boldsymbol{f}_{\hat{u}}^m).\end{aligned}\tag{44}$$

The choice of a single parameter approximation implies that we can combine Eqs. (42) and (43) to obtain the following parametric problem: find $\Delta\psi \in \boldsymbol{\mathcal{L}}^h(\boldsymbol{\mathcal{I}})$ that satisfies

$$\sum_{k=1}^{\mathtt{nd}}\gamma_{LL}^k\mathcal{A}_\theta^k(\delta\psi,\Delta\psi)+\sum_{k=1}^{\mathtt{na}}\gamma_\vartheta^k\mathcal{A}_\vartheta^k(\delta\psi,\Delta\psi)+\gamma\,\mathcal{A}(\delta\psi,\Delta\psi)=\mathcal{R}^m(\delta\psi),\tag{45}$$

for all $\delta\psi \in \boldsymbol{\mathcal{L}}^h(\boldsymbol{\mathcal{I}})$, where

$$\begin{aligned}\gamma_\vartheta^k&:=\gamma_{Lu}^k-\gamma_{L\hat{u}}^k+\gamma_{uL}^k+\gamma_{up}^k+\gamma_{pu}^k-\gamma_{p\hat{u}}^k+\gamma_{\hat{u}L}^k+\gamma_{\hat{u}p}^k+\gamma_{\hat{u}\hat{u}}^k+\gamma_{\rho\hat{u}}^k,\\ \gamma&:=\gamma_{uu}-\gamma_{u\hat{u}}+\gamma_{\rho p}-\gamma_{\rho\rho}+\gamma_{\hat{u}u}+\gamma_{\hat{u}\hat{u}},\\ \mathcal{R}^m(\delta\psi)&:=\mathcal{R}_L^m(\sigma_L^m\boldsymbol{F}_L^m\delta\psi)+\mathcal{R}_u^m(\sigma_u^m\boldsymbol{f}_u^m\delta\psi)+\mathcal{R}_p^m(\sigma_p^m f_p^m\delta\psi)+\mathcal{R}_{\overline{p}}^m(\delta\psi)+\mathcal{R}_{\hat{u}}^m(\sigma_{\hat{u}}^m\boldsymbol{f}_{\hat{u}}^m\delta\psi)+\mathcal{R}_\rho^m(\delta\psi).\end{aligned}\tag{46}$$

Remark 6. Alternative formulations of the parametric problem may be devised, e.g. by considering only equation (42) or (43). In this work, Eq. (45) has been considered in the parametric iteration in order to account for the information of both the local and the global HDG problems.

As detailed in Eq. (35), the parametric iteration involves $\mathtt{n_{pa}}$ geometric parameters. To reduce the size of the problem of the parametric iteration, $\mathtt{n_{pa}}$ one-dimensional problems are solved sequentially, as commonly done in a PGD framework [8].

4.6. The HDG-PGD algorithm

The HDG solver for geometrically parametrised Stokes equation is described in Algorithm 1. Differently from traditional PGD strategies relying on continuous Galerkin approximations, Dirichlet boundary conditions do not require a special treatment in the context of HDG-PGD. More precisely, Dirichlet conditions are imposed in a weak sense and appear in the linear forms (17) of the HDG local problem.

In the greedy enrichment loop, first a predictor of the spatial mode is computed as the solution of the HDG global and local problems using a guess for the parametric mode (Algorithm 1 - Steps 3–5). Then, the alternating direction scheme computes the corrections of the parametric (Algorithm 1 - Steps 8–10) and spatial mode (Algorithm 1 - Steps 11–14) solving a parametric linear system and the HDG global and local problems, respectively. As usual

Algorithm 1 The HDG-PGD implementation

Require: For the greedy enrichment loop, the value $\eta^\star$ of the tolerance. For the alternating direction iterations, the values $\eta_{\hat{u}}$ and $\eta^r_\circ$ of the tolerances for the mode amplitude $\sigma_{\hat{u}}$ and the residuals $r_\circ$ obtained from the linear forms in Appendix B, respectively. For the spatial and parametric problems, the typical values $\text{typ}_\circ$ of the residuals. $\circ = \hat{u}, \psi$.

1: Set $m \leftarrow 1$ and initialise the amplitude of the spatial mode $\sigma^1_{\hat{u}} \leftarrow 1$.
2: **while** $\sigma^m_{\hat{u}} > \eta^\star \sigma^1_{\hat{u}}$ **do**
3: Set $q \leftarrow 1$ and initialise the parametric predictor $\psi^m \leftarrow 1$.
4: Compute the spatial constants (39).
5: Solve the HDG global (40a)–(40b) and local problems (38).
6: Initialise $\varepsilon_{\hat{u}} \leftarrow 1$, $\varepsilon^r_\circ \leftarrow \text{typ}_\circ$.
7: **while** $\varepsilon_{\hat{u}} > \eta_{\hat{u}}$ or $\varepsilon^r_\circ > \eta^r_\circ$ **do**
8: Compute the parametric constants (44).
9: Solve the parametric linear system (45).
10: Update the parametric predictor $\psi^m \leftarrow (\psi^m + \Delta\psi)/\|\psi^m + \Delta\psi\|$.
11: Compute the spatial constants (39).
12: Solve the HDG global (40a)–(40b) and local problems (38).
13: Normalise the spatial predictor $\sigma^m_{\hat{u}} \leftarrow \|\sigma^m_{\hat{u}} \boldsymbol{f}^m_{\hat{u}} + \sigma^m_{\hat{u}} \Delta \boldsymbol{f}_{\hat{u}}\|$.
14: Update the spatial predictor $\sigma^m_{\hat{u}} \boldsymbol{f}^m_{\hat{u}} \leftarrow \sigma^m_{\hat{u}} \boldsymbol{f}^m_{\hat{u}} + \sigma^m_{\hat{u}} \Delta \boldsymbol{f}_{\hat{u}}$.
15: Update the stopping criteria for the mode amplitude $\varepsilon_{\hat{u}} \leftarrow \|\sigma^m_{\hat{u}} \Delta \boldsymbol{f}_{\hat{u}}\|/\sigma^m_{\hat{u}}$ and the residuals $\varepsilon^r_\circ \leftarrow \|r_\circ\|$.
16: Increase the counter of the alternating direction iterations $q \leftarrow q + 1$.
17: **end while**
18: Increase the mode counter $m \leftarrow m + 1$.
19: **end while**

when solving a nonlinear system of equations, the nonlinear iterations of the alternating direction scheme stop when the amplitude $\sigma^m_{\hat{u}} \Delta \boldsymbol{f}_{\hat{u}}$ of the correction is negligible with respect to the amplitude $\sigma^m_{\hat{u}}$ of the current mode and the residuals of the spatial and parametric problems are below a given tolerance (Algorithm 1 - Steps 7 and 15). The stopping criterion for the greedy enrichment algorithm relies on the relative amplitude $\sigma^m_{\hat{u}}$ of the current mode being negligible with respect to the first mode $\sigma^1_{\hat{u}}$ (Algorithm 1 - Step 2). Alternative stopping criteria based on normalising the amplitude of the current mode with respect to the cumulative amplitudes of the previous modes have also been considered in the literature, see e.g. [11]. Note that for the purpose of normalisation (Algorithm 1 - Step 14), an appropriate norm needs to be defined and the $\mathcal{L}_\infty$ norm has been utilised for the simulations in Section 5.

4.6.1. Discretisation of the spatial and parametric problems

The discretisation of the local problems of the spatial iteration using an isoparametric formulation with equal interpolation for all the variables [23,33,34], leads to a system of equations for each element with the following structure:

$$\begin{bmatrix} \mathbf{A}_{LL} & \mathbf{A}_{Lu} & \mathbf{0} & \mathbf{0} \\ \mathbf{A}^T_{Lu} & \mathbf{A}_{uu} & \mathbf{A}_{up} & \mathbf{0} \\ \mathbf{0} & \mathbf{A}^T_{up} & \mathbf{0} & \boldsymbol{a}^T_{\rho p} \\ \mathbf{0} & \mathbf{0} & \boldsymbol{a}_{\rho p} & 0 \end{bmatrix}_e \begin{Bmatrix} \mathbf{F}_L \\ \mathbf{F}_u \\ \mathbf{F}_p \\ \mathrm{F}_\zeta \end{Bmatrix}_e = \begin{Bmatrix} \mathbf{f}_L \\ \mathbf{f}_u \\ \mathbf{f}_p \\ 0 \end{Bmatrix}_e + \begin{bmatrix} \mathbf{A}_{L\hat{u}} \\ \mathbf{A}_{u\hat{u}} \\ \mathbf{A}_{p\hat{u}} \\ \mathbf{0} \end{bmatrix}_e \mathbf{F}_{\hat{u}} + \begin{Bmatrix} \mathbf{0} \\ \mathbf{0} \\ \mathbf{0} \\ 1 \end{Bmatrix}_e \mathrm{F}_\rho, \tag{47}$$

where $\mathbf{F}_L$, $\mathbf{F}_u$, $\mathbf{F}_p$ and $\mathbf{F}_{\hat{u}}$ denote the nodal values of the unknown spatial functions $\sigma^m_L \Delta \boldsymbol{F}_L$, $\sigma^m_u \Delta \boldsymbol{f}_u$, $\sigma^m_p \Delta f_p$ and $\sigma^m_{\hat{u}} \Delta \boldsymbol{f}_{\hat{u}}$ respectively and the constraint on the mean value F_ρ of the pressure on the element boundaries is enforced using the Lagrange multiplier F_ζ.

The only difference between the local system obtained in the spatial iteration of the proposed HDG-PGD approach and the local system of a standard HDG method [33,34] lies in the construction of the blocks forming the matrices $\mathbf{A}_{\odot\circledcirc}$ and vectors $\mathbf{f}_\odot$. As an example, let us consider the matrix $\mathbf{A}_{LL}$. In the proposed HDG-PGD

framework, this matrix is defined as

$$(\mathbf{A}_{LL})_{IJ} = -\sum_{k=1}^{\mathtt{n_d}} \beta_\theta^k \left(N_I, \nu^{-1} D^k N_J\right)_{\Omega_e} \mathbf{I}_{\mathtt{n_{sd}}\times\mathtt{n_{sd}}} \tag{48}$$

whereas in a standard HDG approach, the corresponding matrix is defined as

$$(\mathbf{A}_{LL})_{IJ} = -\left(N_I, \nu^{-1} N_J\right)_{\Omega_e} \mathbf{I}_{\mathtt{n_{sd}}\times\mathtt{n_{sd}}}. \tag{49}$$

In the above expressions $\{N_I\}$ denotes the set of shape functions used to define the spatial approximation of the mixed variable.

Similarly, the discretisation of the global problem of the spatial iteration leads to a system of equations for the trace of the velocity on the element boundaries and the mean value of the pressure in each element, namely

$$\begin{gathered}\sum_{e=1}^{\mathtt{n_{el}}} \left\{ \begin{bmatrix} \mathbf{A}_{\hat{u}L} & \mathbf{A}_{\hat{u}u} & \mathbf{A}_{\hat{u}p} \end{bmatrix}_e \begin{Bmatrix} \mathbf{F}_L \\ \mathbf{F}_u \\ \mathbf{F}_p \end{Bmatrix}_e + [\mathbf{A}_{\hat{u}\hat{u}}]_e \, \mathbf{F}_{\hat{u}} \right\} = \sum_{e=1}^{\mathtt{n_{el}}} [\mathbf{f}_{\hat{u}}]_e, \\ \mathbf{1}^T \, [\mathbf{A}_{p\hat{u}}]_e \mathbf{F}_{\hat{u}} = -\mathbf{1}^T \, [\mathbf{f}_p]_e.\end{gathered} \tag{50}$$

As usual in an HDG context, the local problem of Eq. (47) is used to express the spatial part of the gradient of the velocity, the velocity and the pressure in terms of the spatial part of the trace of the velocity and the mean pressure. Introducing these expressions into the global problem, leads to the global system

$$\begin{bmatrix} \widehat{\mathbf{K}} & \mathbf{G} \\ \mathbf{G}^T & \mathbf{0} \end{bmatrix} \begin{Bmatrix} \mathbf{F}_{\hat{u}} \\ \mathbf{F}_\rho \end{Bmatrix} = \begin{Bmatrix} \hat{\mathbf{f}}_{\hat{u}} \\ \hat{\mathbf{f}}_\rho \end{Bmatrix}, \tag{51}$$

where the only unknowns are the spatial parts of the trace of the velocity and the mean pressure.

In a similar fashion, the discretisation of the parametric problem (45) using Lagrange shape functions leads to an algebraic system of equations whose unknowns are the nodal values of the parametric modes.

4.6.2. A remark for a computationally efficient implementation

The evaluation of the right hand sides of the PGD spatial and parametric iterations tends to become computationally expensive when approximations with a large number of modes are considered. Indeed, the number of terms involved in such computation experiences a geometric growth rate during the iterations of the greedy algorithm.

In order to ease the computational burden of the overall algorithm, the number of terms in the modal approximations $\boldsymbol{u}^m_{\mathtt{PGD}}$, $p^m_{\mathtt{PGD}}$, $\boldsymbol{L}^m_{\mathtt{PGD}}$, $\hat{\boldsymbol{u}}^m_{\mathtt{PGD}}$ and $\rho^m_{\mathtt{PGD}}$ is reduced. It is well known that the terms in the PGD reduced basis are not orthogonal to each other and repeated information may appear. Hence, orthogonal separable approximations featuring $\widetilde{m} < m$ modes are constructed via the PGD compression [20,49], that is, a least-squares higher-order projection minimising the $\mathcal{L}_2$ norm of the difference between target and test functions, namely

$$\begin{aligned}
\boldsymbol{L}^{\widetilde{m}}_{\mathtt{PGD}} &= \underset{\boldsymbol{W}\in\boldsymbol{\mathcal{W}}^h}{\arg\min} \, \|\boldsymbol{W} - \boldsymbol{L}^m_{\mathtt{PGD}}\|_{\mathcal{L}_2(\Omega\times\boldsymbol{\mathcal{I}})}, \\
\boldsymbol{u}^{\widetilde{m}}_{\mathtt{PGD}} &= \underset{\boldsymbol{v}\in\boldsymbol{\mathcal{V}}^h}{\arg\min} \, \|\boldsymbol{v} - \boldsymbol{u}^m_{\mathtt{PGD}}\|_{\mathcal{L}_2(\Omega\times\boldsymbol{\mathcal{I}})}, \\
p^{\widetilde{m}}_{\mathtt{PGD}} &= \underset{v\in\mathcal{V}^h}{\arg\min} \, \|v - p^m_{\mathtt{PGD}}\|_{\mathcal{L}_2(\Omega\times\boldsymbol{\mathcal{I}})}, \\
\hat{\boldsymbol{u}}^{\widetilde{m}}_{\mathtt{PGD}} &= \underset{\hat{\boldsymbol{v}}\in\widehat{\boldsymbol{\mathcal{V}}}^h}{\arg\min} \, \|\hat{\boldsymbol{v}} - \hat{\boldsymbol{u}}^m_{\mathtt{PGD}}\|_{\mathcal{L}_2(\Gamma\cup\Gamma_N\cup\Gamma_S\times\boldsymbol{\mathcal{I}})}, \\
\rho^{\widetilde{m}}_{\mathtt{PGD}} &= \underset{q\in\mathbb{R}^{\mathtt{n_{el}}}\otimes\boldsymbol{\mathcal{L}}^h(\boldsymbol{\mathcal{I}})}{\arg\min} \, \|q - \rho^m_{\mathtt{PGD}}\|_{\mathcal{L}_2(\mathbb{R}^{\mathtt{n_{el}}}\times\boldsymbol{\mathcal{I}})}.
\end{aligned}$$

From a practical point of view, the PGD compression is applied during the enrichment strategy described in Algorithm 1. A trade-off between the cost of performing the greedy iterations with a larger number of modes and the extra cost required by the PGD compression needs to be achieved. For the simulations in Section 5, PGD compression is applied every ten new computed modes for the analytical examples and every five for the microfluidics test cases.

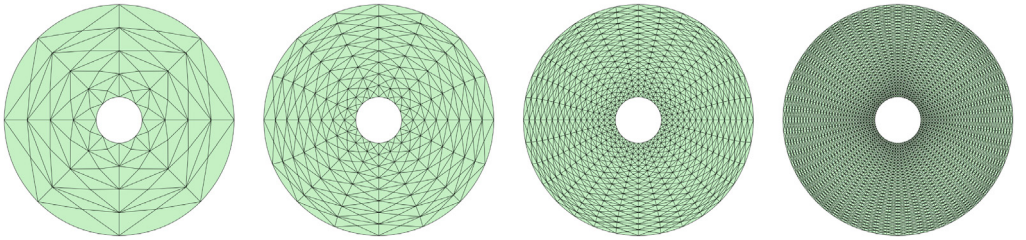

(a) Mesh 1 (b) Mesh 2 (c) Mesh 3 (d) Mesh 4

Fig. 1. Coaxial Couette flow: Four triangular meshes of the reference domain.

5. Numerical examples

This section presents four numerical examples. The first two examples are used to validate the implementation of the proposed approach as well as to study a number of properties of the proposed ROM. The last two examples consider two applications taken from the biomechanics community and involve the Stokes flow around a micro-swimmer formed by two spheres and the flow around a sphere in a corrugated channel. All the examples consider geometric parameters as extra coordinates within the proposed PGD approach.

5.1. Coaxial Couette flow

The first example considers the well known coaxial Couette flow problem [50], consisting of the flow confined within two infinite coaxial circular cylinders with radius R_{in} and R_{out} respectively, with $R_{\text{in}} < R_{\text{out}}$. The boundary conditions introduce the known angular velocities, Ω_{in} and Ω_{out}, at R_{in} and R_{out}, respectively. The problem has analytical solution, given by the azimuthal component of the velocity as

$$v_\phi = \frac{R_{\text{out}}^2\Omega_{\text{out}} - R_{\text{in}}^2\Omega_{\text{in}}}{R_{\text{out}}^2 - R_{\text{in}}^2} r + \frac{(\Omega_{\text{in}} - \Omega_{\text{out}})R_{\text{out}}^2 R_{\text{in}}^2}{R_{\text{out}}^2 - R_{\text{in}}^2}\frac{1}{r} \tag{52}$$

where r is the distance to the axis of the cylinders.

To demonstrate the applicability of the proposed ROM the problem is considered in two dimensions, with $\Omega^\mu = \{\boldsymbol{x}^{\boldsymbol{\mu}} \in \mathbb{R}^2 \mid \mu_1 \leq r^\mu \leq R_{\text{out}}\}$, with $R_{\text{out}} = 5$ and $\mu_1 \in \mathcal{I} = \mathcal{I}^1 = [1, 3]$ and where $r^\mu = \sqrt{(x_1^\mu)^2 + (x_2^\mu)^2}$. The reference domain is chosen to be $\Omega = \{\boldsymbol{x} \in \mathbb{R}^2 \mid 1 \leq r \leq R_{\text{out}}\}$ and the mapping between the reference and the geometrically parametrised domains is defined by the general separable expression of Eq. (21) with the mapping of Eq. (22) given by

$$\begin{aligned} \mathbf{M}^1(\boldsymbol{x}) &= \frac{1}{r}\boldsymbol{x} \qquad & \psi^1(\mu) &= \frac{R_{\text{out}}(\mu - 1)}{R_{\text{out}} - 1}, \\ \mathbf{M}^2(\boldsymbol{x}) &= \boldsymbol{x} \qquad & \psi^2(\mu) &= \frac{R_{\text{out}} - \mu}{R_{\text{out}} - 1}, \end{aligned} \tag{53}$$

where $r = \sqrt{x_1^2 + x_2^2}$. The Jacobian of the mapping is also written in the general separated form of Eq. (23), with

$$\mathbf{J}^1(\boldsymbol{x}) = \frac{1}{r^3}\begin{bmatrix} x_2^2 & -x_1x_2 \\ -x_1x_2 & x_1^2 \end{bmatrix}, \qquad \mathbf{J}^2(\boldsymbol{x}) = \mathbf{I}_2. \tag{54}$$

For the numerical experiments in this section, four triangular meshes of the reference domain are generated, as shown in Fig. 1. The meshes have 128, 512, 2048 and 8192 elements respectively.

The proposed HDG-PGD framework is used to obtain the generalised solution of the parametric Stokes problem. The first four normalised modes of the magnitude of the velocity field are displayed in Fig. 2. The computation was performed using the second mesh shown in Fig. 1 with a degree of approximation $k = 4$ for all the variables and with a mesh of 1000 elements in the parametric dimension with also $k = 4$. As usual in the context of ROMs,

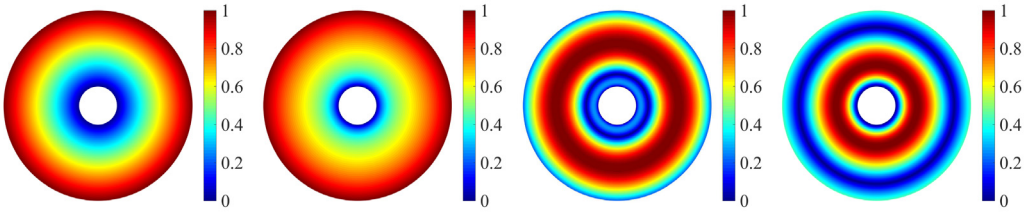

(a) $m = 1$ (b) $m = 2$ (c) $m = 3$ (d) $m = 4$

Fig. 2. Coaxial Couette flow: First four normalised spatial modes of the velocity field.

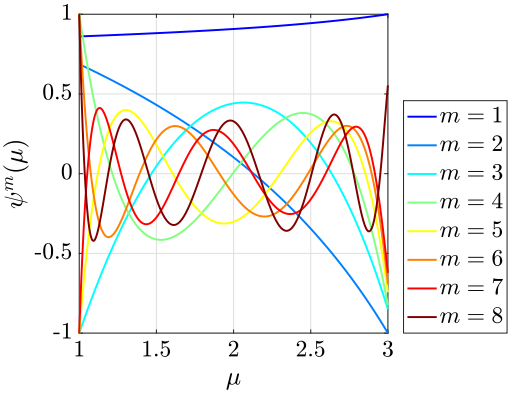

Fig. 3. Coaxial Couette flow: First eight normalised parametric modes.

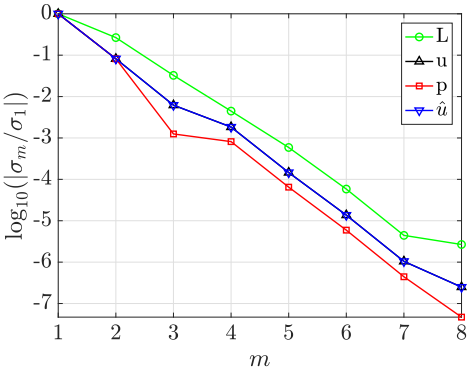

Fig. 4. Coaxial Couette flow: Convergence of the mode amplitudes.

the first modes capture the most relevant and global features of the solution whereas the features captured for the next modes only introduce localised features.

Fig. 3 shows the first eight normalised parametric modes computed. It can be observed that the first three modes are smooth, whereas the next modes, that have a less relevant contribution to the generalised solution, show a more oscillatory character.

To quantify the importance of the modes on the generalised solution, Fig. 4 shows the relative amplitudes of the modes with respect to the amplitude of the first mode for all the variables. It can be clearly observed that the fourth mode has an amplitude that is already more than 100 times smaller than the amplitude of the first mode. After computing only nine modes the relative amplitude is already of the order of 10^{-6}. It is worth noting that in

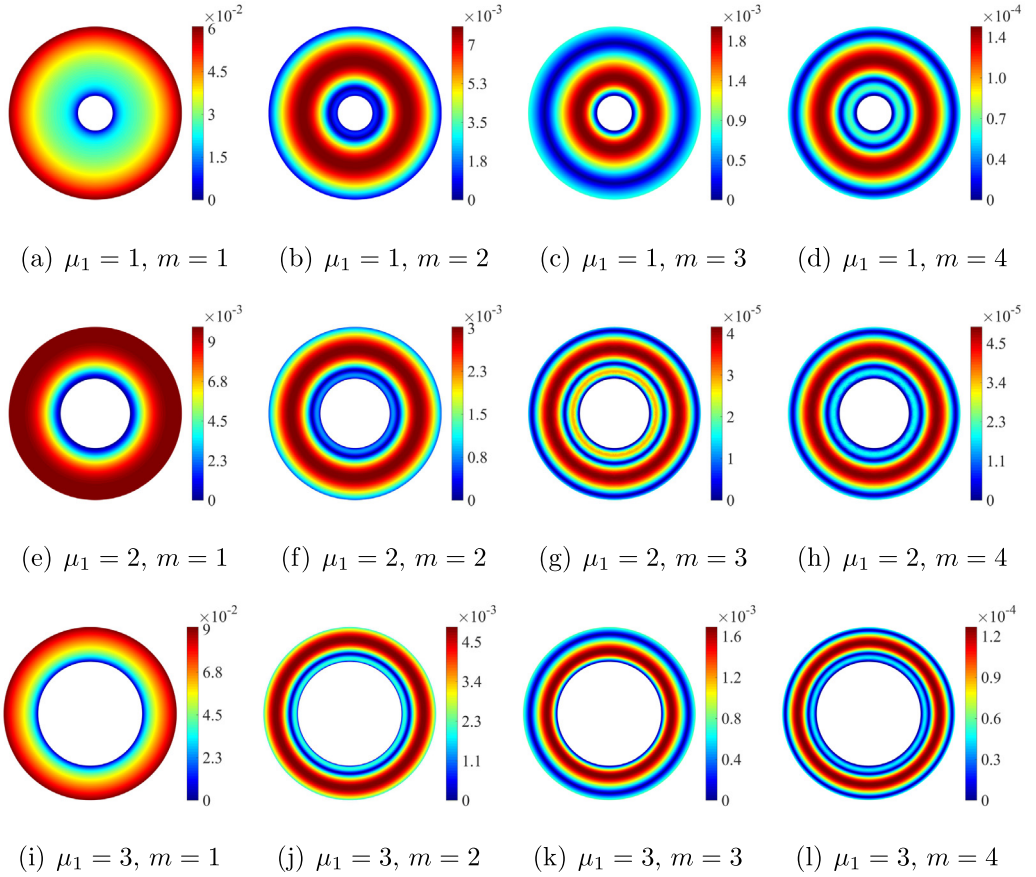

Fig. 5. Coaxial Couette flow: Absolute value of the error of the velocity magnitude using n PGD modes and for different values of the geometric parameter μ_1. A quartic approximation is used for all variables in the second mesh of Fig. 1.

practice it is not required to add modes with such a lower relative amplitude with respect to the first mode, but in this first example nine modes are computed to show the rapid decrease in their amplitudes.

Once the generalised solution is computed, it is of interest to quantify its accuracy. Fig. 5 shows the absolute value of the error of the velocity magnitude using as the number of modes is increased for three relevant configurations corresponding to the parameter $\mu_1 = 1$, $\mu_1 = 2$ and $\mu_1 = 3$. The results show that with only one PGD mode an absolute error below 10^{-1} is already obtained for all three configurations, with more accurate results for the case with $\mu_1 = 2$. With two PGD modes the error drops substantially, being less than 7×10^{-3} in all cases, and with only three PGD modes the error is below 2×10^{-4} for the three configurations considered.

To further illustrate the accuracy of the proposed HDG-PGD approach, the relative error in the $\mathcal{L}_2(\Omega \times \boldsymbol{\mathcal{I}})$ norm, defined as

$$\varepsilon_{\texttt{PGD}} = \left(\frac{\int_{\mathcal{I}_1} \int_{\Omega} (\boldsymbol{u}_{\texttt{PGD}} - \boldsymbol{u}) \cdot (\boldsymbol{u}_{\texttt{PGD}} - \boldsymbol{u}) d\Omega \, d\mu}{\int_{\mathcal{I}_1} \int_{\Omega} \boldsymbol{u} \cdot \boldsymbol{u} \, d\Omega \, d\mu} \right)^{1/2}, \tag{55}$$

is studied and compared to the error of the full order HDG approach. Fig. 6 shows the evolution of $\varepsilon_{\texttt{PGD}}$, for all the variables, as the number of PGD modes is increased, for different meshes using a quadratic degree of approximation. The discontinuous lines in Fig. 6 show the relative error of the full order HDG method, measured in the $\mathcal{L}_2(\Omega \times \boldsymbol{\mathcal{I}})$ norm. It is worth noting that the computation of the error for the full order approach requires the computation of a large number of solutions. More precisely, the number of HDG solutions required is equal to the number of elements in the parametric space multiplied by number of integrations points in each element.

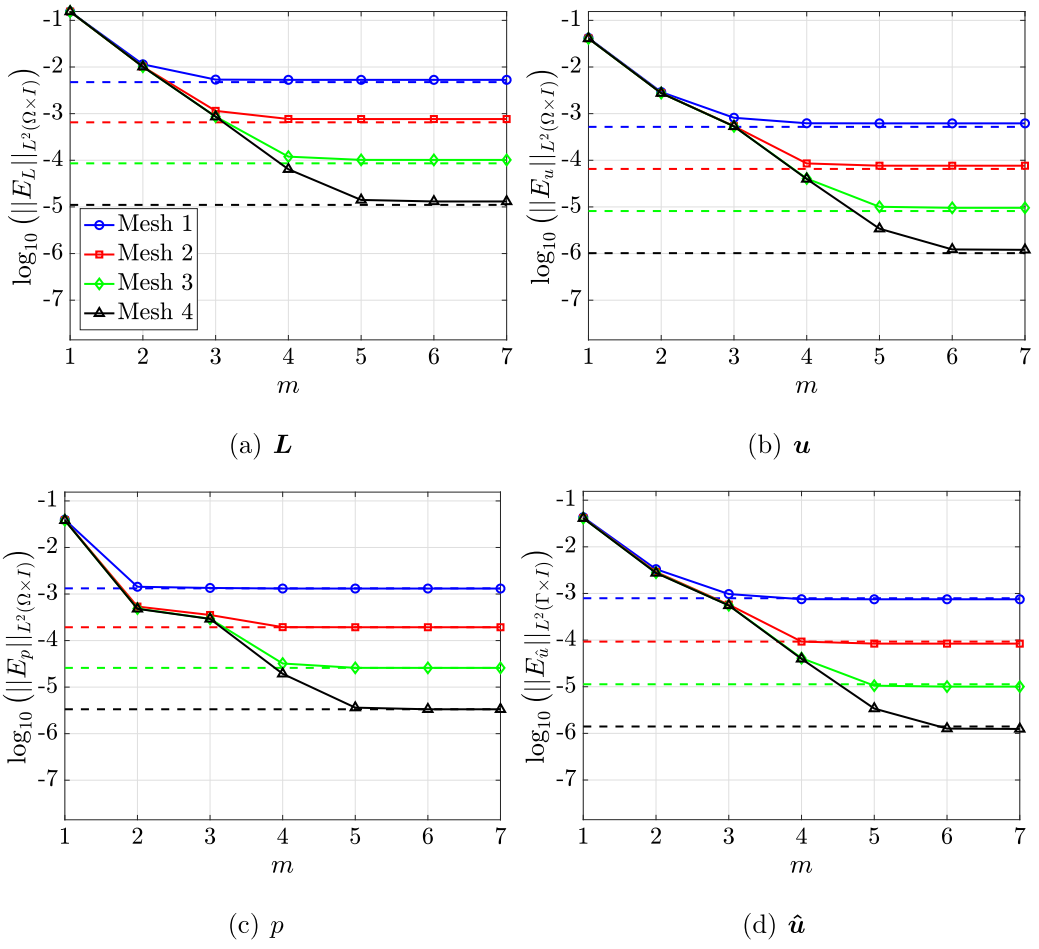

Fig. 6. Coaxial Couette flow: convergence of the $\mathcal{L}_2$ norm of the error for $\boldsymbol{L}$, $\boldsymbol{u}$, p and $\hat{\boldsymbol{u}}$ as the number of PGD modes is increased. A quadratic approximation is used for all the variables.

The results show that the error of the proposed ROM converges monotonically to the error of the full order approach as the number of modes is increased. In all cases the number of PGD modes required to reach the maximum accuracy on a given mesh is lower than six. Furthermore, the results in Fig. 6 illustrate the increased level of accuracy obtained as the spatial and parametric discretisations are refined. Analogous results, not reported here for brevity, are obtained for lower and higher orders of approximation.

Next, the optimal rate of convergence of the proposed HDG-PDG method is studied by performing a mesh convergence study. Fig. 7 shows the evolution of the relative error in the $\mathcal{L}_2(\Omega \times \mathcal{I})$ norm as a function of the characteristic element size, h, for different orders of approximation and for all the variables of the HDG formulation. The optimal rate of convergence, equal to h^{k+1}, is approximately observed for all the variables. In each case, the minimum number of PGD modes required to achieve the accuracy of the full order method is selected, as previously discussed when presenting the results of Fig. 6.

Finally, it is worth mentioning the differences between the proposed HDG-PGD approach presented here and the recently proposed PGD approach for geometrically parametrised domains in [19] using standard finite elements for the spatial discretisation. First, the current approach does not require the higher order PGD projection to separate the inverse of the determinant of the Jacobian, given the first-order character of the problem solved with HDG. Second, the current approach enables the use of the same degree of approximation for velocity and pressure, contrary to the standard FE approach where specific choices are required to satisfy the LBB condition. In the context of

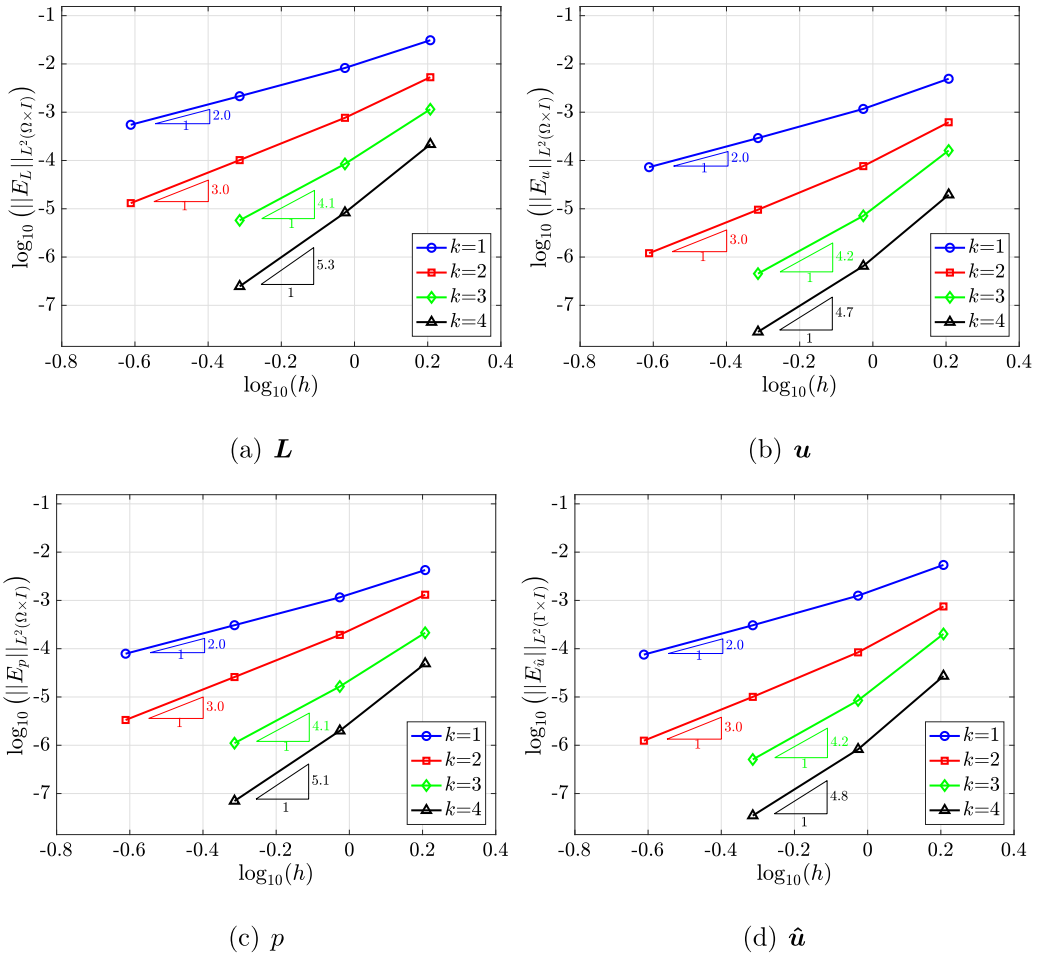

Fig. 7. Coaxial Couette flow: mesh convergence of the $\mathcal{L}_2$ norm of the error for $\boldsymbol{L}$, $\boldsymbol{u}$, p and $\hat{\boldsymbol{u}}$.

geometrically parametrised domains with curved boundaries this implies that the current approach enables the use of isoparametric elements whereas super-parametric or sub-parametric elements are required in the FE context. Third, the weak imposition of the Dirichlet boundary conditions, as usually done in a DG context, facilitates the construction of the generalised solution without the need for specific choices for the modes that satisfy the Dirichlet boundary conditions, as required by other approaches. Finally, the results in Fig. 7 can be compared to the results in [19].

5.2. Axisymmetric Stokes flow past a sphere

The second example considers the Stokes flow past a sphere, a typical test case for axisymmetric Stokes flow solvers. The domain of interest is selected as the region confined by two concentric spheres with radius R_{in} and R_{out} respectively, with $R_{\text{in}} < R_{\text{out}}$. This problem also has analytical solution, given, in polar coordinates, by the following velocity and pressure fields

$$\begin{aligned} u_r &= \frac{v_\infty}{2r^3}\left(2r^3 - 3R_{\text{in}}r^2 + R_{\text{in}}^3\right)\cos\theta, \\ u_\theta &= -\frac{v_\infty}{4r^3}\left(4r^3 - 3R_{\text{in}}r^2 + R_{\text{in}}^3\right)\sin\theta, \\ p &= p_\infty - \frac{3}{2r^2}\nu v_\infty R_{\text{in}}\cos\theta, \end{aligned} \tag{56}$$

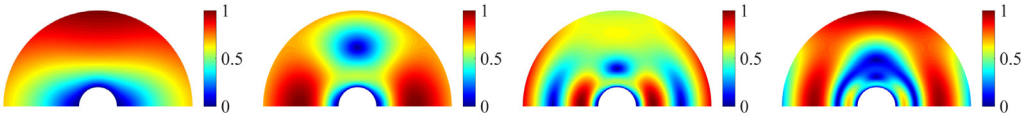

(a) $m = 1$ (b) $m = 2$ (c) $m = 3$ (d) $m = 4$

Fig. 8. Axisymmetric flow past a sphere: First four normalised spatial modes of the norm of the velocity field.

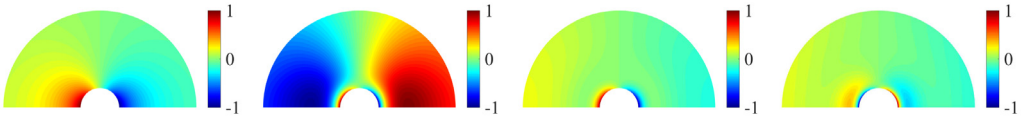

(a) $m = 1$ (b) $m = 2$ (c) $m = 3$ (d) $m = 4$

Fig. 9. Axisymmetric flow past a sphere: First four normalised spatial modes of the pressure field.

where v_∞ and p_∞ are the magnitude of the velocity and the pressure of the undisturbed flow, far away from the obstacle. A typical quantity of interest in this problem is the drag force, whose exact value is given by $F_D = 6\pi \nu v_\infty R_{\text{in}}$

Similar to the previous example, the geometric parameter considered here is the radius of the inner sphere. The parametric domain considers the axial symmetry of the problem is defined as $\Omega^\mu = \{\boldsymbol{x}^{\boldsymbol{\mu}} \in \mathbb{R}^2 \mid x_2^\mu \geq 0$ and $\mu_1 \leq r^\mu \leq R_{\text{out}}\}$, with $R_{\text{out}} = 5$ and $\mu_1 \in \mathcal{I} = \mathcal{I}^1 = [1, 3]$. The reference domain is chosen to be $\Omega = \{\boldsymbol{x} \in \mathbb{R}^2 \mid x_2 \geq 0$ and $1 \leq r \leq R_{\text{out}}\}$. The mapping between the reference and the geometrically parametrised domains is exactly the same mapping utilised in the previous example, given by the two terms in Eq. (53).

A no-slip boundary condition is imposed on the inner sphere, a Dirichlet boundary condition corresponding to the exact solution on the outer boundary and axial symmetry is imposed on the rest of the boundary. The axial symmetry is imposed by selecting $\alpha = \beta = 0$ in the matrices $\boldsymbol{D}^{\boldsymbol{\mu}}$ and $\boldsymbol{E}^{\boldsymbol{\mu}}$ in Eq. (1). As mentioned earlier, in Remark 3, the portion of the boundary where the axial symmetry is imposed depends on the geometric parameter, but the normal and tangent to the boundary are independent on the geometric changes. Therefore, the matrices $\boldsymbol{D}$ and $\boldsymbol{E}$ do not depend upon the geometric parameters.

The proposed ROM is used to obtain the generalised solution of the parametric axisymmetric Stokes problem. The first four normalised modes of the magnitude of the velocity field and the pressure are shown in Figs. 8 and 9.

The computation was performed using the second mesh with a degree of approximation $k = 4$ for all the variables and with a mesh of 1000 elements in the parametric dimension with also $k = 4$. Fig. 10 shows the first eight normalised parametric modes computed. It is worth noting that despite the different nature of the flow and the axisymmetric boundary condition, the parametric modes have a similar behaviour when compared to the modes obtained in the previous example. This is mainly attributed to the geometric parameter describing an analogous variation of the computational domain.

As in the previous example, the evolution of the relative amplitude of the modes is shown in 11. The rapid decrease shows that it is possible to compute a generalised solution to this problem with a very small number of modes. With eight modes the relative amplitude is already below 10^{-5}.

Next, the optimal rate of convergence of the proposed HDG-PGD method are studied by performing a mesh convergent study. Fig. 12 shows the evolution of the relative error in the $\mathcal{L}_2(\Omega \times \mathcal{I})$ norm as a function of the characteristic element size, h, for different orders of approximation and for all the variables of the HDG formulation. The optimal rate of convergence, equal to h^{k+1}, is approximately observed for all the variables.

Finally, the accuracy of the HDG-PGD approach on the drag force is studied for three different configurations corresponding to $\mu_1 = 1$, $\mu_1 = 2$ and $\mu_1 = 3$. Fig. 13 shows evolution of the error in the drag force as the number of degrees of freedom is increased for the three different geometric configurations and for different orders of approximation.

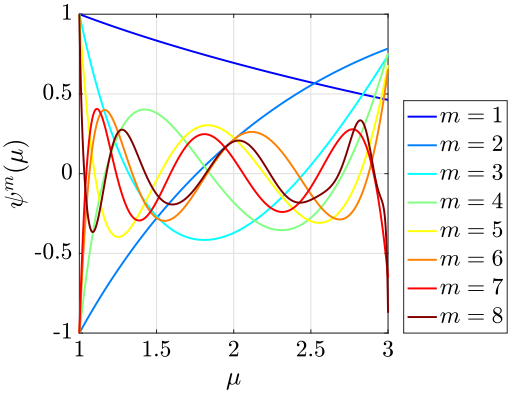

Fig. 10. Axisymmetric flow past a sphere: First eight normalised parametric modes.

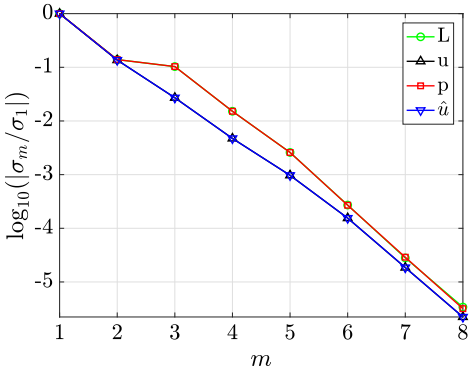

Fig. 11. Axisymmetric flow past a sphere: Convergence of the mode amplitudes.

The number of degrees of freedom refers to the size of the HDG global problem as this is the most time consuming part of the spatial iteration.

The results show the variation of the drag force induced by the variation of the geometric parameter and how the generalised solution produces accurate results for any value of the geometric parameter. In all cases, convergence to exact value is observed, and the superiority of using high-order approximations is clearly appreciated. For the first configuration, the results in Fig. 13(a) show that with a linear approximation requires the solution of a global problem with 24,832 degrees of freedom to obtain relative error in the drag force of 0.0181. In contrast , using a quartic approximation, the error in the first mesh is 0.0021, solving a global problem with only 416 degrees of freedom, that is an error one order of magnitude lower with almost 20 times less degrees of freedom.

The results also show that for higher values of the geometric parameter the solution is slightly more difficult to capture and the number of degrees of freedom required is slightly higher. In fact, the advantages of high-order approximations are more noticeable for the case of $\mu_1 = 3$.

Finally, it is worth mentioning that when objective is to compute a given quantity of interest, such as the drag force, the adoption of a goal oriented PGD approach would be beneficial to incorporate the required accuracy of a quantity of interest in the stopping criteria.

5.3. Axisymmetric Stokes flow around two micro-swimmers

The next example considers the Stokes flow around the so-called *push-me-push-you microswimmer*, proposed in [51]. This swimmer consists of two spherical bladders that have the ability to change their mutual distance and individual volume, whilst maintaining the total volume of the two spheres. The swimmer is placed in a cylindrical channel of length L and diameter D.

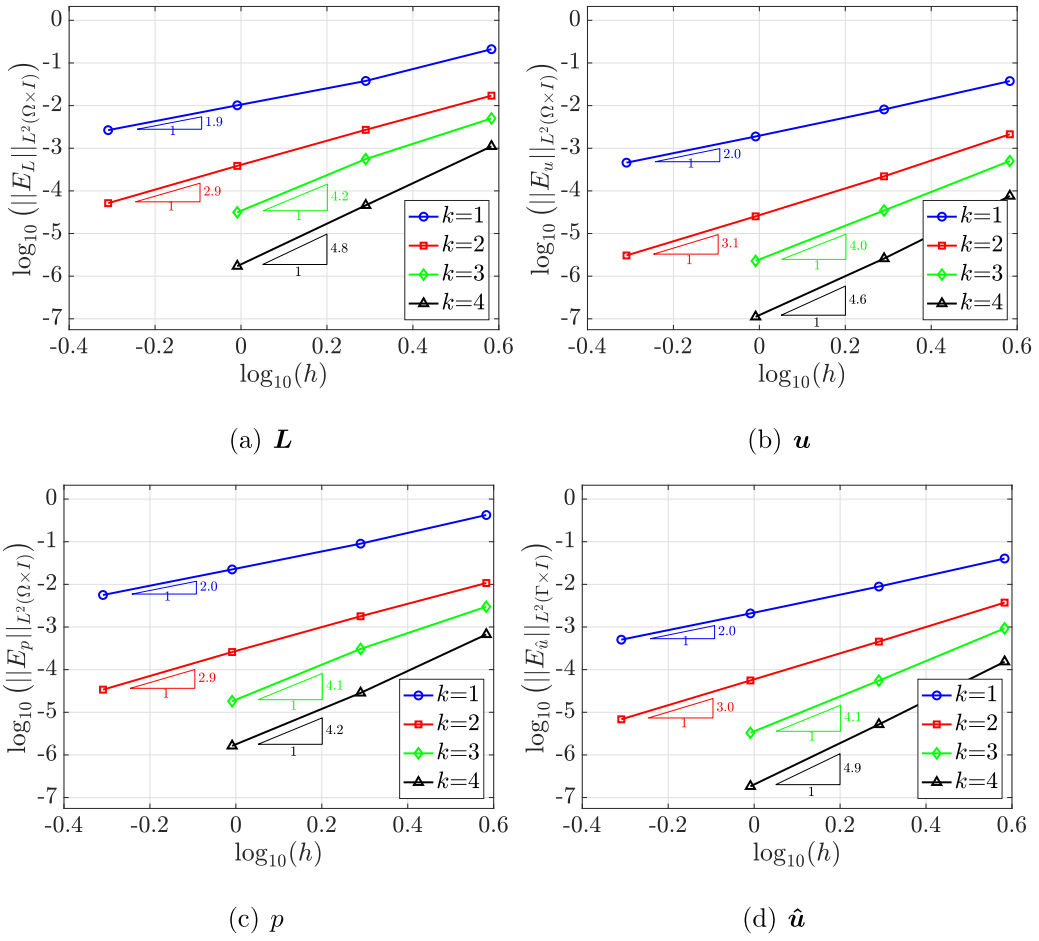

Fig. 12. Axisymmetric flow past a sphere: mesh convergence of the $\mathcal{L}_2$ norm of the error for $\boldsymbol{L}$, $\boldsymbol{u}$, p and $\hat{\boldsymbol{u}}$.

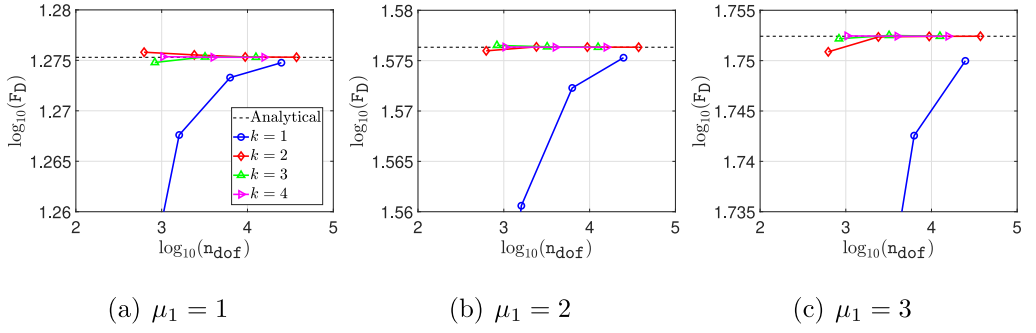

Fig. 13. Axisymmetric flow past a sphere: evolution of the error in the drag force as the number of modes is increased for three different geometric configurations.

Two geometric parameters are considered in this example. The first one, $\mu_1 \in \mathcal{I}_1 = [-1, 1]$, controls the radius of the two spheres in such a way that the total volume of the two spheres is maintained. The second parameter, $\mu_2 \in \mathcal{I}_2 = [-3, 2]$, controls the distance between the centre of the two spheres. The value of $\mu_1 = -1$ corresponds to the configuration where the radius of the first sphere is $R_1 = 0.3096$ and the radius of the second sphere is $R_2 = 0.116$, whereas the value of $\mu = 1$ corresponds to the opposite situation, with $R_1 = 0.116$ and $R_2 = 0.3096$.

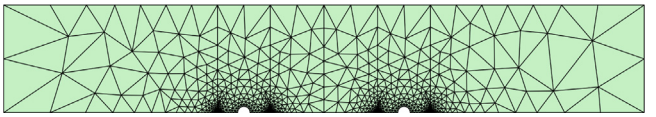

Fig. 14. Axisymmetric flow around two micro-swimmers: Computational mesh.

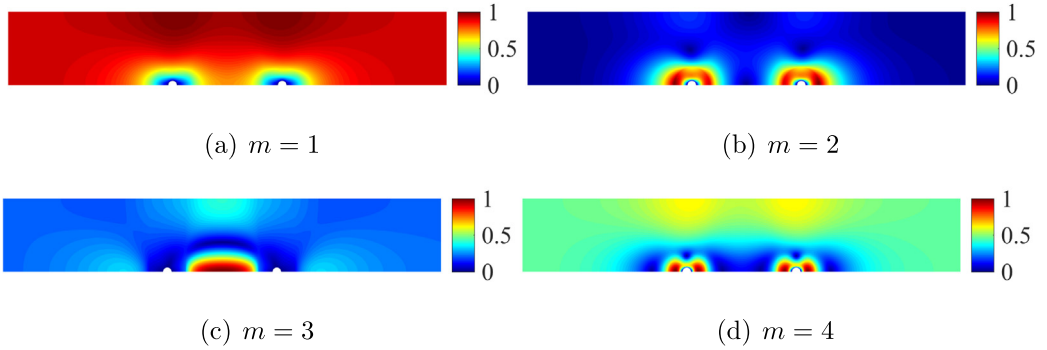

Fig. 15. Axisymmetric flow around two micro-swimmers: First four normalised spatial modes of the velocity field.

The value of $\mu_2 = -3$ corresponds to the case where the distance between the spheres is maximum, with the centres of the spheres placed at $(-3, 0)$ and $(3, 0)$ respectively. The value of $\mu_2 = 2$ corresponds to the case where the distance between the spheres is minimum, with the centres of the spheres placed at $(-0.5, 0)$ and $(0.5, 0)$ respectively.

Using the axial symmetry of the problem, the reference domain is chosen as $\Omega = ([-L, L] \times [0, H]) \setminus \left(\mathcal{B}^+ \cup \mathcal{B}^-\right)$, where

$$\mathcal{B}^{\pm} = \{\boldsymbol{x} \in \mathbb{R}^2 \mid \|\boldsymbol{x} \pm \boldsymbol{x}_0\| \leq R_{\text{ref}}\}, \tag{57}$$

where $L = 6$, $H = 2$, $\boldsymbol{x}_0 = (1.5, 0)$ and $R_{\text{ref}} = 0.116$. Fig. 14 shows the triangular mesh of the reference domain used for this numerical example. The mesh has 1426 elements, leading to a system in the HDG global problem of 22,260 equations for a degree of approximation $k = 4$.

On the left part of the boundary a Dirichlet boundary condition, corresponding to a horizontal velocity of magnitude one, is imposed. On the right part of the boundary a homogeneous Neumann boundary condition is imposed. On the surface of the two spheres a no-slip boundary condition is enforced and on the rest of the boundary a slip boundary condition is imposed.

The geometric mapping used in this example is detailed in Appendix C.

The first four spatial modes for the velocity and pressure computed with the proposed HDG-PGD are shown in Figs. 15 and 16. The computation was performed using the mesh of Fig. 14 with a degree of approximation $k = 4$ for all the variables and with a mesh of 10,000 elements in each parametric dimension with also $k = 4$. It is worth noting that the cost of the one-dimensional parametric problems is negligible when compared to the cost of the spatial iteration. Therefore, a large number of elements is used in the parametric dimension to ensure that the variation induced by the geometric parameters are captured with no a priori knowledge of the solution.

Fig. 17 shows the first eight normalised parametric modes computed.

Contrary to the previous examples, in this example there are more parametric modes that have an important influence over the whole range of values for both μ_1 and μ_2. For instance, in Fig. 17(a) the first, third, fifth and six parametric modes have a normalised value near one for the whole range of values of μ_1. A similar behaviour is observed for the second parameter μ_2. In addition, the second parameter, corresponding to the distance between the spheres it can be observed that many of the modes have a much more relevant influence near $\mu_2 = 2$. This is expected as this configuration corresponds to the case where the distance between the spheres is minimum and therefore induces an important variation in the flow field because the first sphere will influence the flow that is reaching the second sphere.

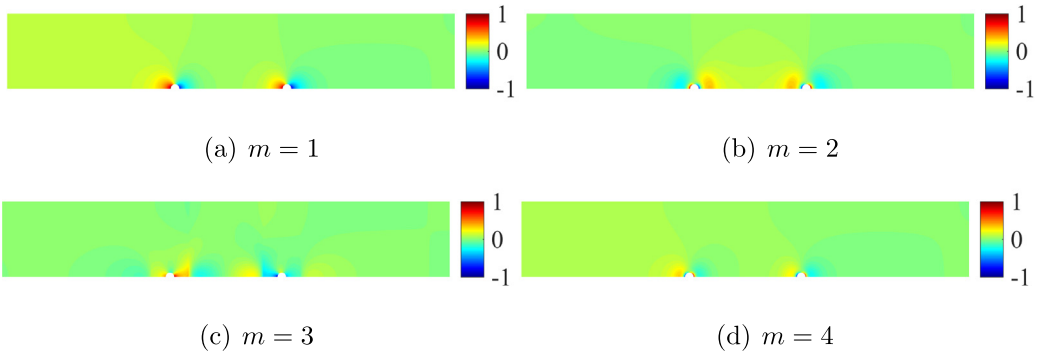

Fig. 16. Axisymmetric flow around two micro-swimmers: First four normalised spatial modes of the pressure field.

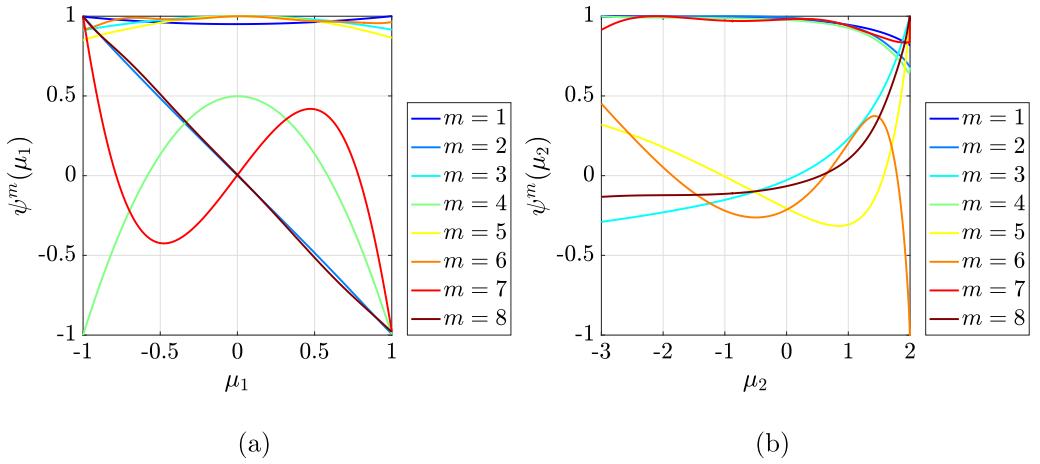

Fig. 17. Axisymmetric flow around two micro-swimmers: First eight normalised parametric modes.

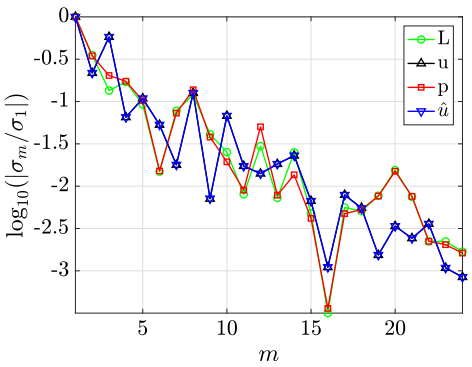

Fig. 18. Axisymmetric flow around two micro-swimmers: Convergence of the mode amplitudes.

The evolution of the relative amplitude of the modes is displayed in Fig. 18. The results show that with 24 modes all the relative amplitude of the hybrid variable, used to check convergence, is below 10^{-3}. A slower decrease of the relative amplitudes when compared with the previous examples can be observed. This is attributed to two factors. First, this problem considers two geometric parameters and, second, the range of variation of the distance is relatively high when compared to the minimum radius of the spheres.

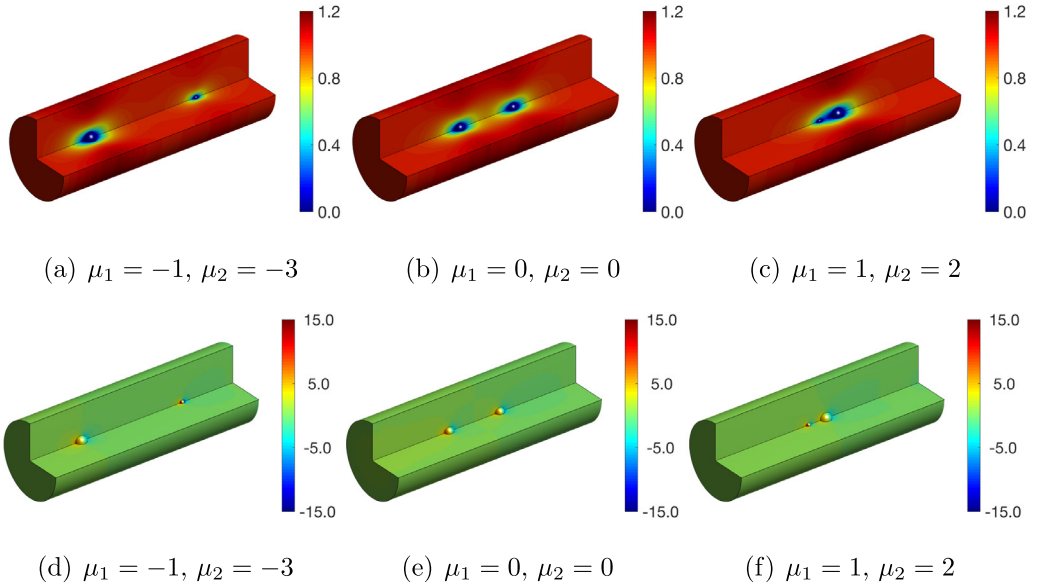

Fig. 19. Axisymmetric flow around two micro-swimmers: Velocity (top) and pressure (bottom) fields for three different geometric configurations.

To illustrate the variation in the geometry induced by the parameters as well as the different flow features that are induced by the geometric changes, Fig. 19 shows the magnitude of the velocity and the pressure fields in the three dimensional domain for three different configurations.

The first configuration, shown in Figs. 19(a) and 19(d), corresponds to the case where the distance between the spheres is maximum and the sphere closer to the inflow boundary has maximum radius. The opposite scenario, with the distance between spheres is minimum and the sphere closer to the inflow boundary has minimum radius is shown in Figs. 19(c) and 19(f). Finally, the configuration displayed in Figs. 19(b) and 19(e) corresponds to the case when the distance between the spheres is half the maximum value and the radius of both spheres is the same.

To analyse the accuracy of the proposed approach, Fig. 20 compares the drag force on the two spheres as a function of the μ_2, controlling the distance between the spheres, and for three different configurations of the μ_1, controlling the radius of both spheres. The results obtained with the HDG-PGD approach are compared to the results of the standard HDG method on a reference mesh. Both solutions show an excellent agreement in all cases, with an overlap between the symbols used to plot the results of the standard HDG method and the discontinuous line used to plot the results of the proposed PGD approach.

Finally, to stress the potential of the proposed approach, Fig. 21 shows the drag force on the two spheres and the total drag as a function of both geometric parameters. This figure shows that generalised solution computed with the HDG-PGD approach can be used to rapidly explore the whole space of parameters and used to find optimal strokes, of interest in many applications [52].

5.4. Stokes flow around a sphere in a corrugated channel

The last example, inspired from the studies in [53,54], considers the flow past a sphere placed in a corrugated channel. The corrugated channel has a height of 1 μm and the undulatory profile is defined by the expression

$$y = \begin{cases} \frac{1}{2}\left(f_\omega + f_n\right) + \frac{1}{2}\left(f_\omega - f_n\right)\cos\left(\frac{16\pi x}{7L}\right) & \text{if} \quad |x| < \frac{7}{16}L, \\ f_n & \text{if} \quad \frac{7}{16}L \leq |x| \leq \frac{1}{2}L, \end{cases} \tag{58}$$

where $L = 12.5$ μm, $f_\omega = 2$ μm and the value of f_n controls the oscillation of the boundary. A sphere of radius R, centred at the origin, is placed inside the corrugated channel.

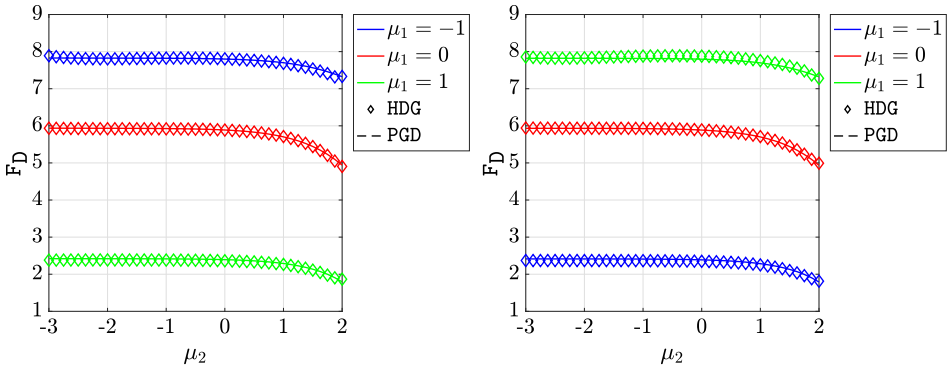

(a) First sphere (b) Second sphere

Fig. 20. Axisymmetric flow around two micro-swimmers: Comparison of the drag computed on the first and second sphere with the proposed HDG-PGD approach against a reference solution for different configurations. Symbols are used to plot the results of the standard HDG method whereas the discontinuous line shows the results of the proposed PGD approach. The overlap between both shows the excellent agreement provided by the proposed PGD approach.

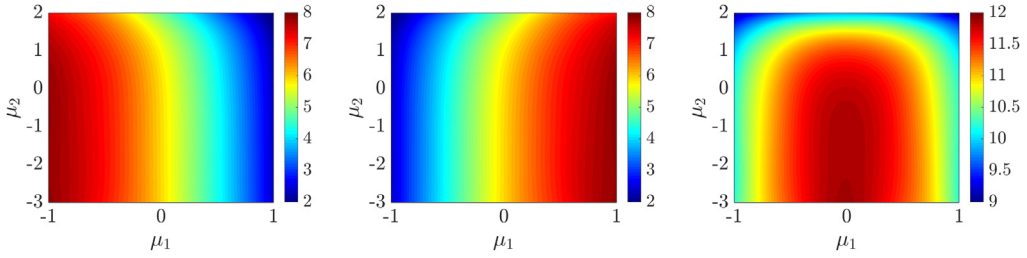

(a) First sphere (b) Second sphere (c) Total

Fig. 21. Axisymmetric flow around two micro-swimmers: Drag force on the individual spheres and the total drag over the two spheres.

A Dirichlet boundary condition is imposed at one end of the channel, given by $\boldsymbol{u}_D(\boldsymbol{x}) = \left\{64(x_2^2-1/4)(x_3^2-1/4), 0, 0\right\}^T$, and a homogeneous Neumann boundary condition is imposed at the other end. A homogeneous Dirichlet boundary condition is on the rest of the boundary of the domain, corresponding to material walls.

To demonstrate the applicability and potential of the proposed methodology in three dimensions, two geometric parameters are considered. The first parameter $\mu_1 \in [-1, 1]$ is used to control the radius of the sphere, defined as $R(\mu_1) = (\mu_1 + 2)/10$. The second parameter $\mu_2 \in [0, 2]$ controls the amplitude of the corrugated channel, given by $f_n = 1/2 + \mu_2$. The geometry of the reference domain, corresponding to $\mu_1 = \mu_2 = 0$, is shown in Fig. 22(a).

Exploiting the symmetry of the problem, a mesh of a quarter of the domain is considered, with 2191 tetrahedral elements, as depicted in Fig. 22(b).

The geometric mapping used in this example is detailed in Appendix D.

The first four spatial modes for the velocity and pressure computed with the proposed HDG-PGD are shown in Figs. 23 and 24. The computation was performed using the mesh of Fig. 22(a) with a degree of approximation $k = 3$ for all the variables and with a mesh of 10,000 elements in each parametric dimension with also $k = 3$.

Fig. 25 shows the first six normalised parametric modes computed.

Compared to previous examples, the results show that more modes have an influence over the whole range of parameters, illustrating the more complex nature of this three dimensional example.

The evolution of the relative amplitude of the modes is displayed in Fig. 26. In this example, 12 modes are required to ensure the relative amplitude of the hybrid variable, used to check convergence, is below 10^{-3}.

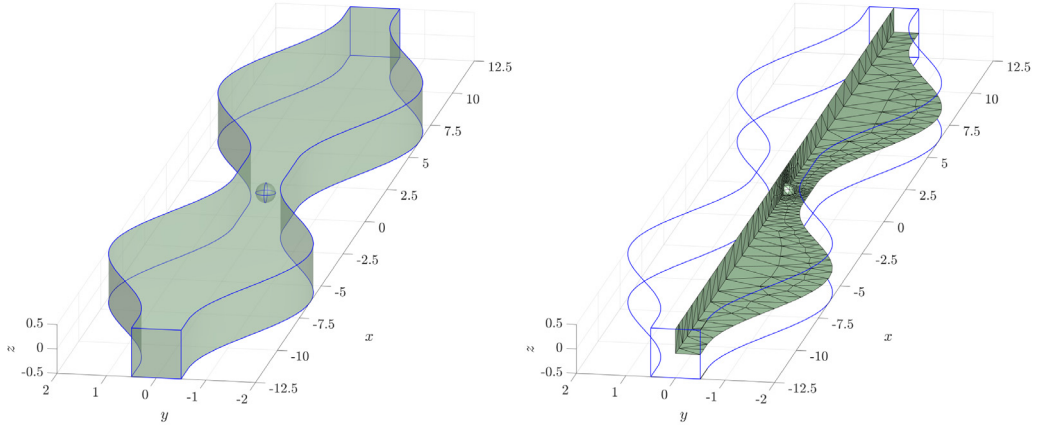

(a) Geometry (b) Mesh

Fig. 22. Flow around a sphere in a corrugated channel: Geometry of the domain and computational mesh of a quarter of the domain.

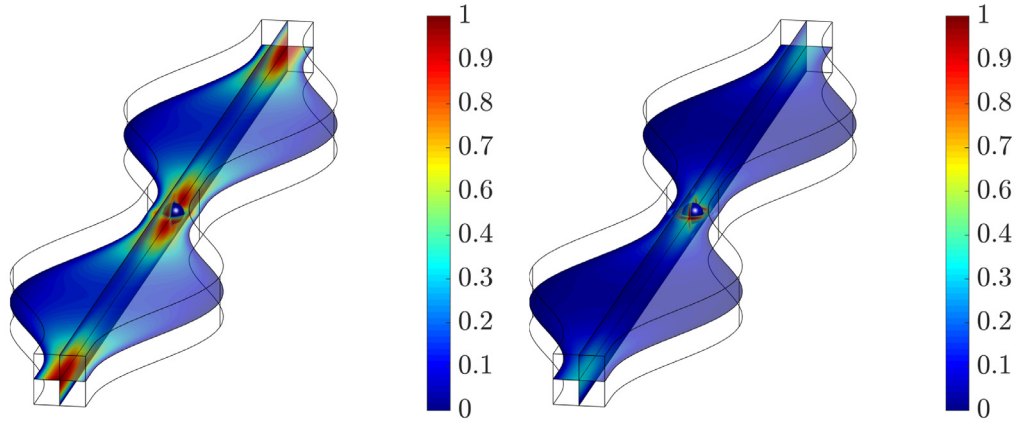

(a) $m = 1$ (b) $m = 2$

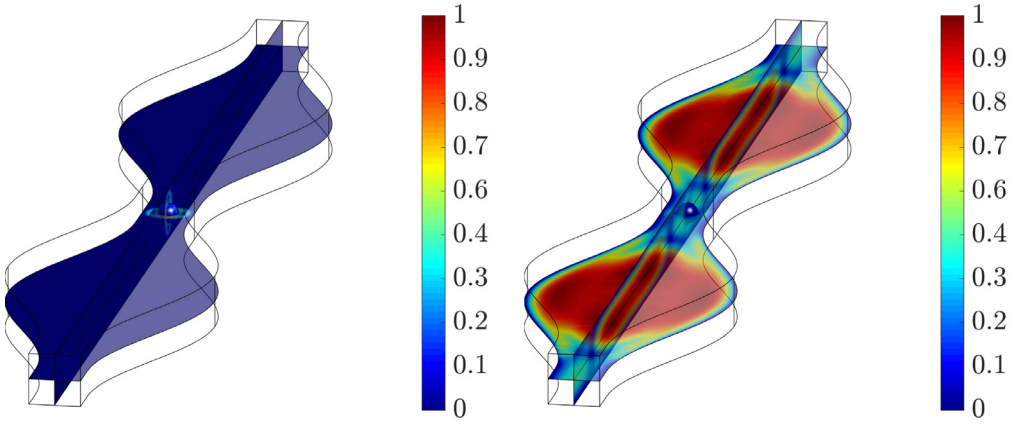

(c) $m = 3$ (d) $m = 4$

Fig. 23. Flow around a sphere in a corrugated channel: First four normalised spatial modes of the velocity field.

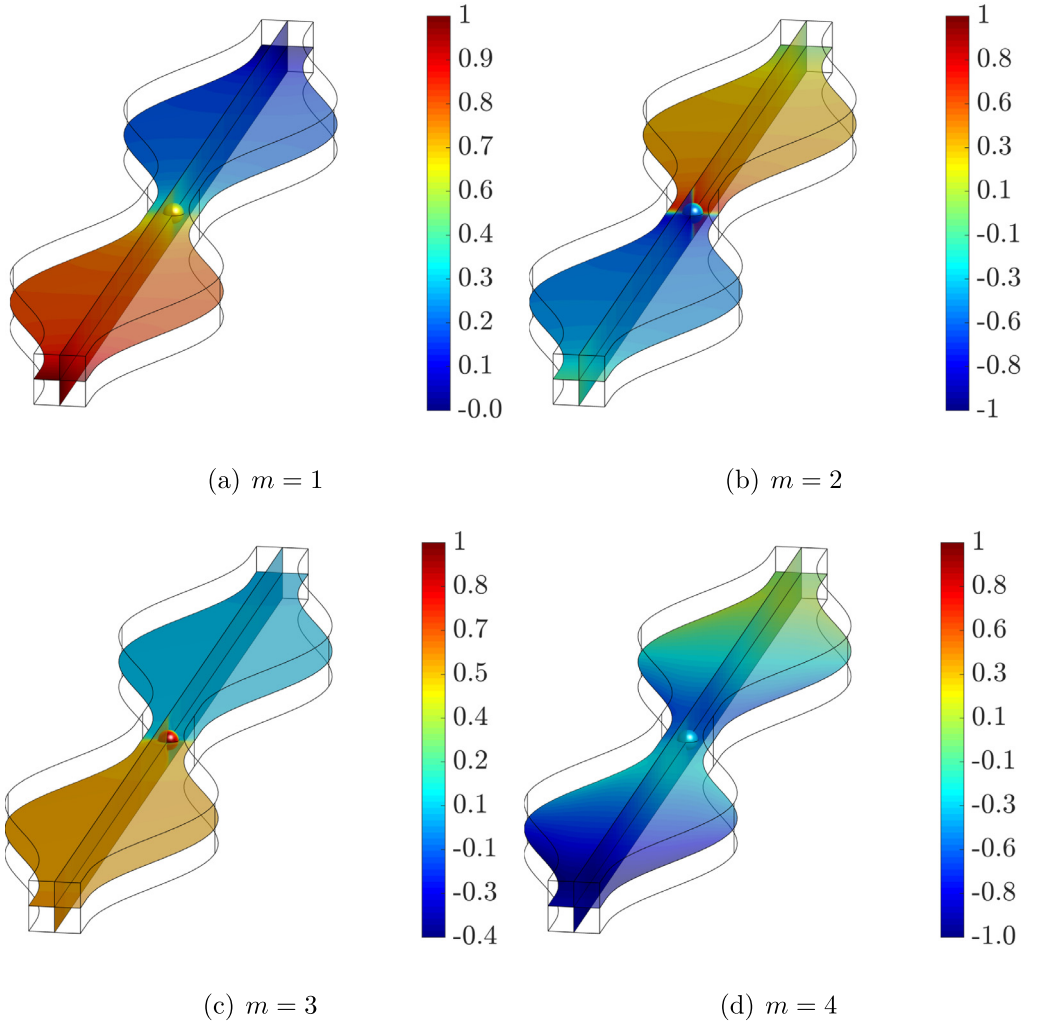

Fig. 24. Flow around a sphere in a corrugated channel: First four normalised spatial modes of the pressure field.

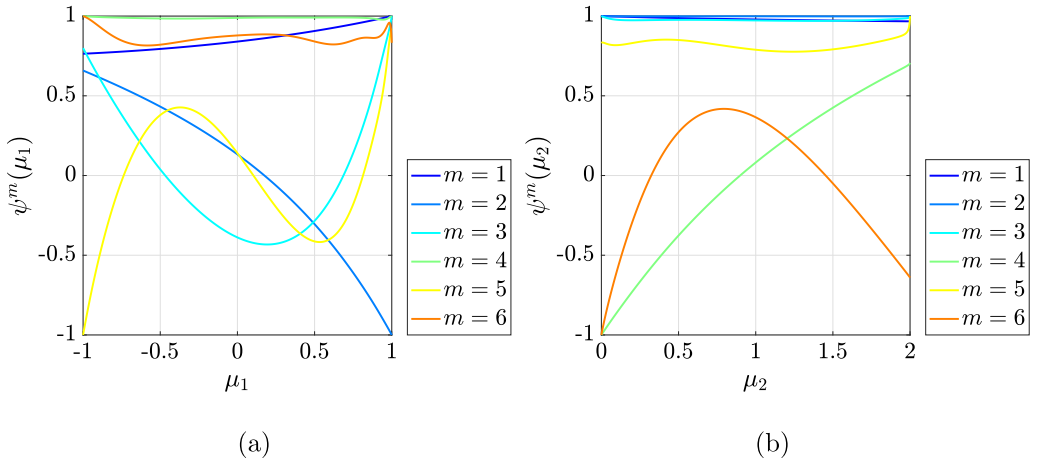

Fig. 25. Flow around a sphere in a corrugated channel: First six normalised parametric modes.

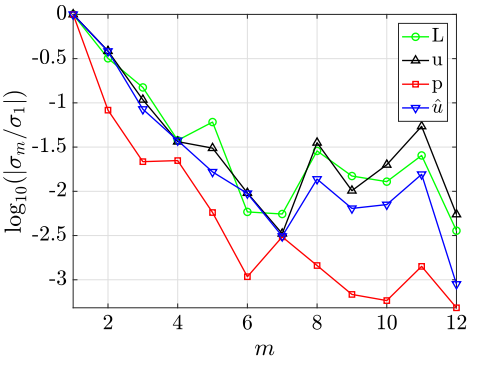

Fig. 26. Flow around a sphere in a corrugated channel: Convergence of the mode amplitudes.

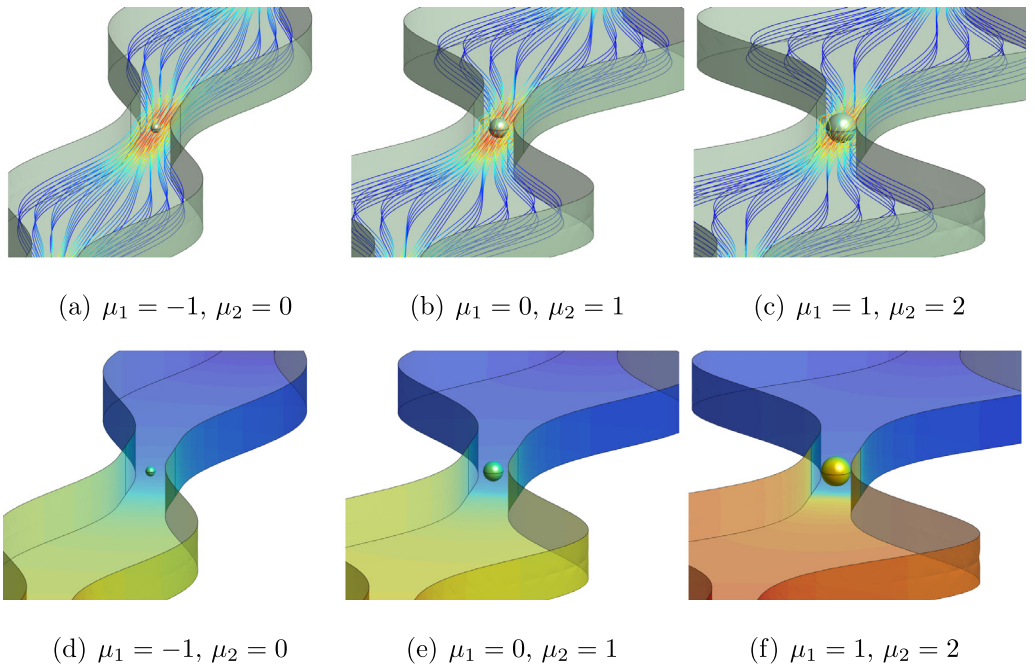

(a) $\mu_1 = -1,\ \mu_2 = 0$ (b) $\mu_1 = 0,\ \mu_2 = 1$ (c) $\mu_1 = 1,\ \mu_2 = 2$

(d) $\mu_1 = -1,\ \mu_2 = 0$ (e) $\mu_1 = 0,\ \mu_2 = 1$ (f) $\mu_1 = 1,\ \mu_2 = 2$

Fig. 27. Flow around a sphere in a corrugated channel: Velocity (top) and pressure (bottom) fields for three different geometric configurations.

Fig. 27 shows the magnitude of the velocity and the pressure fields in the channel for three different configurations. The results illustrate the variation in the velocity and pressure fields as the amplitude of the channel and the radius of the sphere is increased.

To assess the accuracy of the computed generalised solution computed with the proposed approach, a reference solution is computed for the three configurations displayed in Fig. 27. The reference solutions are computed on a much finer mesh with a standard HDG solver. As a quantity of interest, the drag on the sphere is measured. Fig. 28 shows the evolution of the error of the drag force as the number of PGD modes is increased. To further analyse the accuracy of the computed generalised solution, the error of an HDG solution, computed in each configuration using the same spatial resolution as the one used in the HDG-PGD formulation is considered. The results show that the error of the HDG-PGD approach tends to the error of the HDG solution computed for each configuration, showing the ability of the proposed approach to accurately capture the solution for different geometric configurations.

As mentioned in the previous example, the proposed approach provides a generalised solution that can be used to perform fast queries of different quantities of interest. To illustrate the potential of the developed HDG-PGD

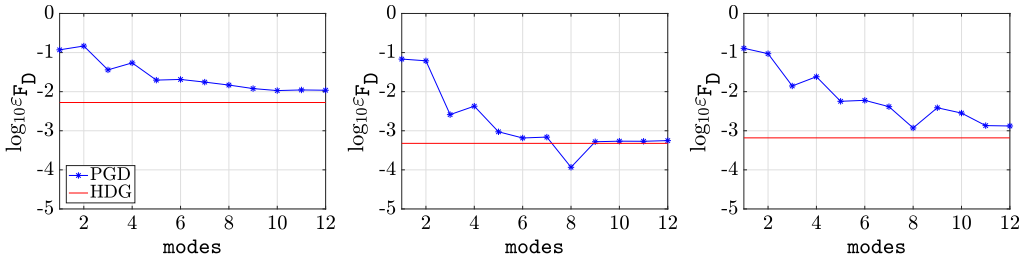

(a) $\mu_1 = -1$, $\mu_2 = 0$ (b) $\mu_1 = 0$, $\mu_2 = 1$ (c) $\mu_1 = 1$, $\mu_2 = 2$

Fig. 28. Flow around a sphere in a corrugated channel: Evolution of the error on the drag force as the number of PGD modes is increased. The horizontal line denotes the reference error computed on a finer mesh with the standard HDG method.

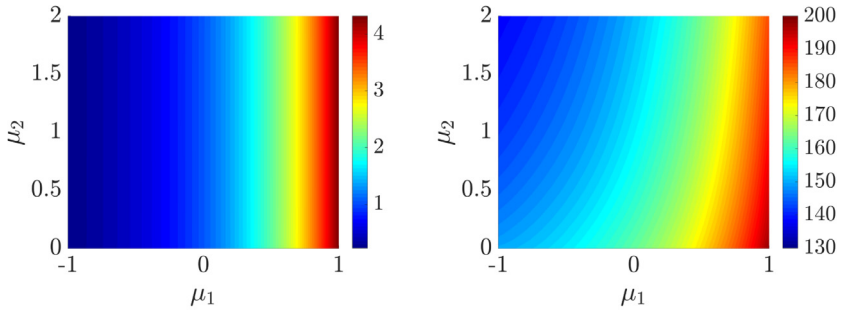

(a) Drag (b) Pressure drop

Fig. 29. Flow around a sphere in a corrugated channel: Drag force on the sphere and difference between the pressure at the inlet and the outlet.

approach, Fig. 29 shows the drag force on the sphere and the pressure drop, measured as the difference between the pressure at the inlet and outlet, as a function of the geometric parameters μ_1 and μ_2. The results show that the drag force is not sensitive to the variation of the amplitude of the channel oscillation but very dependent on the radius of the sphere. In contrast, the pressure drop shows a dependency on both geometric parameters.

6. Concluding remarks

A reduced order model approach based on the PGD and the HDG methods is being presented for the solution of geometrically parametrised Stokes flow problems. The mixed formulation, characteristic of HDG methods, is shown to provide advantages as the weak formulation can be written in a separated form, without using to the memory intensive high-order PGD projection. In addition, the adoption of an HDG formulation enables the use of equal order of approximation for all the variables circumventing the LBB condition. This is advantageous in the context of geometrically parametrised problems in complex domains as it enables the use of standard isoparametric formulations. Finally, the use of a DG formulation implies that no special treatment of the Dirichlet boundary conditions is required.

Two numerical examples with analytical solution are used to demonstrate the optimal mesh convergence properties of the proposed approach. These examples are also used to illustrate that the accuracy of the PGD approach, with enough computed modes, matches the accuracy provided by the standard HDG method when computing the solution for a given parameter. The examples also quantify the number of required modes to reach a given accuracy when the velocity, pressure and gradient of the velocity are of interest and when the drag force is of interest. Finally, these examples also provide evidence of the superiority of high order elements when compared to low order elements.

The ability of the proposed approach to compute generalised solutions involving geometric parameters has been illustrated for problems relevant to the microfluidics community. The examples consider geometric parameters that

involve substantial changes of the geometry and induce sizeable changes in the flow features and the relevant quantities of interest. The two examples presented show the potential in the solution of axisymmetric and three dimensional problems with two geometric parameters.

The proposed methodology can be extended to nonlinear problems following the rationale presented in [11].

Declaration of competing interest

The authors declare that they have no known competing financial interests or personal relationships that could have appeared to influence the work reported in this paper.

Acknowledgements

This work was partially supported by the European Union's Horizon 2020 research and innovation programme under the Marie Skłodowska-Curie Actions (Grant number: 675919) that financed the Ph.D. fellowship of L.B. and by the Spanish Ministry of Economy and Competitiveness (Grant number: DPI2017-85139-C2-2-R). M.G. and A.H. are also grateful for the support provided by the Spanish Ministry of Economy and Competitiveness through the Severo Ochoa programme for centres of excellence in RTD (Grant number: CEX2018-000797-S) and the Generalitat de Catalunya (Grant number: 2017-SGR-1278). R.S. also acknowledges the support of the Engineering and Physical Sciences Research Council (Grant number: EP/P033997/1).

Appendix A. Bilinear forms of the HDG-PGD weak formulation

The bilinear forms introduced in the spatial iteration are given by

$$
\begin{aligned}
&\mathcal{A}^k_{LL}(\delta\boldsymbol{F}_L, \boldsymbol{F}_L) \coloneqq -\left(\delta\boldsymbol{F}_L, \nu^{-1} D^k \boldsymbol{F}_L\right)_{\Omega_e}, && \mathcal{A}^k_{Lu}(\delta\boldsymbol{F}_L, \boldsymbol{f}_u) \coloneqq \left(\mathbf{A}^k\boldsymbol{\nabla}\cdot\delta\boldsymbol{F}_L, \boldsymbol{f}_u\right)_{\Omega_e},\\
&\mathcal{A}^k_{L\hat{u}}(\delta\boldsymbol{F}_L, \boldsymbol{f}_{\hat{u}}) \coloneqq \langle \mathbf{A}^k\boldsymbol{n}\cdot\delta\boldsymbol{F}_L, \boldsymbol{f}_{\hat{u}}\rangle_{\partial\Omega_e\setminus\Gamma_D}, && \mathcal{A}^k_{uL}(\delta\boldsymbol{f}_u, \boldsymbol{F}_L) \coloneqq \left(\delta\boldsymbol{f}_u, \mathbf{A}^k\boldsymbol{\nabla}\cdot\boldsymbol{F}_L\right)_{\Omega_e},\\
&\mathcal{A}_{uu}(\delta\boldsymbol{f}_u, \boldsymbol{f}_u) \coloneqq \langle \delta\boldsymbol{f}_u, \boldsymbol{\tau}\boldsymbol{f}_u\rangle_{\partial\Omega_e}, && \mathcal{A}^k_{up}(\delta\boldsymbol{f}_u, f_p) \coloneqq \left(\delta\boldsymbol{f}_u, \mathbf{A}^k\boldsymbol{\nabla} f_p\right)_{\Omega_e},\\
&\mathcal{A}_{u\hat{u}}(\delta\boldsymbol{f}_u, \boldsymbol{f}_{\hat{u}}) \coloneqq \langle \delta\boldsymbol{f}_u, \boldsymbol{\tau}\boldsymbol{f}_{\hat{u}}\rangle_{\partial\Omega_e\setminus\Gamma_D} && \mathcal{A}^k_{pu}(\delta f_p, \boldsymbol{f}_u) \coloneqq \left(\mathbf{A}^k\boldsymbol{\nabla}\delta f_p, \boldsymbol{f}_u\right)_{\Omega_e},\\
&\mathcal{A}^k_{p\hat{u}}(\delta f_p, \boldsymbol{f}_{\hat{u}}) \coloneqq \langle \delta f_p, \boldsymbol{f}_{\hat{u}}\cdot\mathbf{A}^k\boldsymbol{n}\rangle_{\partial\Omega_e\setminus\Gamma_D}, && \mathcal{A}_{\rho p}(\delta f_\rho, f_p) \coloneqq \langle \delta f_\rho, |\partial\Omega_e|^{-1} f_p\rangle_{\partial\Omega_e},\\
&\mathcal{A}_{\rho\rho}(\delta f_\rho, f_\rho) \coloneqq \delta f_\rho\, f_\rho,
\end{aligned}
\tag{A.1}
$$

for the HDG local problems and by

$$
\begin{aligned}
&\mathcal{A}^k_{\hat{u}L}(\delta\boldsymbol{f}_{\hat{u}}, \boldsymbol{F}_L) \coloneqq \langle \delta\boldsymbol{f}_{\hat{u}}, \mathbf{A}^k\boldsymbol{n}\cdot\boldsymbol{F}_L\rangle_{\partial\Omega_e\setminus(\Gamma_D\cup\Gamma_S)} - \langle \delta\boldsymbol{f}_{\hat{u}}, \mathbf{A}^k\boldsymbol{n}\cdot\boldsymbol{F}_L\boldsymbol{E}\rangle_{\partial\Omega_e\cap\Gamma_S},\\
&\mathcal{A}_{\hat{u}u}(\delta\boldsymbol{f}_{\hat{u}}, \boldsymbol{f}_u) \coloneqq \langle \delta\boldsymbol{f}_{\hat{u}}, \boldsymbol{\tau}\boldsymbol{f}_u\rangle_{\partial\Omega_e\setminus(\Gamma_D\cup\Gamma_S)} - \langle \delta\boldsymbol{f}_{\hat{u}}, (\boldsymbol{\tau}\boldsymbol{f}_u)\cdot\boldsymbol{E}\rangle_{\partial\Omega_e\cap\Gamma_S},\\
&\mathcal{A}^k_{\hat{u}p}(\delta\boldsymbol{f}_{\hat{u}}, f_p) \coloneqq \langle \delta\boldsymbol{f}_{\hat{u}}, f_p\mathbf{A}^k\boldsymbol{n}\rangle_{\partial\Omega_e\setminus(\Gamma_D\cup\Gamma_S)},\\
&\mathcal{A}_{\hat{u}\hat{u}}(\delta\boldsymbol{f}_{\hat{u}}, \boldsymbol{f}_{\hat{u}}) \coloneqq -\langle \delta\boldsymbol{f}_{\hat{u}}, \boldsymbol{\tau}\boldsymbol{f}_{\hat{u}}\rangle_{\partial\Omega_e\setminus(\Gamma_D\cup\Gamma_S)} + \langle \delta\boldsymbol{f}_{\hat{u}}, (\boldsymbol{\tau}\boldsymbol{f}_{\hat{u}})\cdot\boldsymbol{E}\rangle_{\partial\Omega_e\cap\Gamma_S},\\
&\mathcal{A}^k_{\hat{u}\hat{u}}(\delta\boldsymbol{f}_{\hat{u}}, \boldsymbol{f}_{\hat{u}}) \coloneqq \langle \delta\boldsymbol{f}_{\hat{u}}, \boldsymbol{f}_{\hat{u}}\cdot\mathbf{A}^k\boldsymbol{D}\rangle_{\partial\Omega_e\cap\Gamma_S},
\end{aligned}
\tag{A.2}
$$

for the HDG global problems.

In addition, the following bilinear forms are introduced in the parametric iteration

$$
\begin{aligned}
&\mathcal{A}^k_\theta(\delta\psi, \psi) \coloneqq \left(\delta\psi, \theta^k\psi\right)_{\boldsymbol{\mathcal{I}}},\\
&\mathcal{A}^k_\vartheta(\delta\psi, \psi) \coloneqq \left(\delta\psi, \vartheta^k\psi\right)_{\boldsymbol{\mathcal{I}}},\\
&\mathcal{A}(\delta\psi, \psi) \coloneqq \left(\delta\psi, \psi\right)_{\boldsymbol{\mathcal{I}}}.
\end{aligned}
\tag{A.3}
$$

Appendix B. Linear forms of the HDG-PGD weak formulation

The linear forms introduced in the spatial and parametric iterations are given by

$$
\begin{aligned}
\mathcal{R}^m_L(\delta\boldsymbol{F}_L\psi) \coloneqq &\sum_{k=1}^{\mathtt{n_a}}\sum_{l=1}^{\mathtt{n_D}}\langle \mathbf{A}^k\boldsymbol{n}\cdot\delta\boldsymbol{F}_L, \boldsymbol{g}^l_D\rangle_{\partial\Omega_e\cap\Gamma_D}\mathcal{A}^k_\vartheta(\psi, \lambda^l_D)\\
&-\sum_{i=1}^{m}\sum_{k=1}^{\mathtt{n_d}}\mathcal{A}^k_{LL}(\delta\boldsymbol{F}_L, \sigma^i_L\boldsymbol{F}^i_L)\mathcal{A}^k_\theta(\psi, \psi^i)
\end{aligned}
$$

$$
\begin{aligned}
&- \sum_{i=1}^{m} \sum_{k=1}^{\mathtt{n_a}} \left\{ \mathcal{A}^k_{Lu}(\delta \boldsymbol{F}_L, \sigma^i_u \boldsymbol{f}^i_u) - \mathcal{A}^k_{L\hat{u}}(\delta \boldsymbol{F}_L, \sigma^i_{\hat{u}} \boldsymbol{f}^i_{\hat{u}}) \right\} \mathcal{A}^k_{\vartheta}(\psi, \psi^i) \\
\mathcal{R}^m_u(\delta \boldsymbol{f}_u \psi) &:= \sum_{k=1}^{\mathtt{n_d}} \sum_{l=1}^{\mathtt{n_S}} \left(\delta \boldsymbol{f}_u, D^k \boldsymbol{g}^l_S\right)_{\Omega_e} \mathcal{A}^k_{\vartheta}(\psi, \lambda^l_S) \\
&+ \sum_{l=1}^{\mathtt{n_D}} \langle \delta \boldsymbol{f}_u, \boldsymbol{\tau} \boldsymbol{g}^l_D \rangle_{\partial \Omega_e \cap \Gamma_D} \mathcal{A}(\psi, \lambda^l_D) \\
&- \sum_{i=1}^{m} \sum_{k=1}^{\mathtt{n_a}} \left\{ \mathcal{A}^k_{uL}(\delta \boldsymbol{f}_u, \sigma^i_L \boldsymbol{F}^i_L) + \mathcal{A}^k_{up}(\delta \boldsymbol{f}_u, \sigma^i_p f^i_p) \right\} \mathcal{A}^k_{\vartheta}(\psi, \psi^i) \\
&- \sum_{i=1}^{m} \left\{ \mathcal{A}_{uu}(\delta \boldsymbol{f}_u, \sigma^i_u \boldsymbol{f}^i_u) - \mathcal{A}_{u\hat{u}}(\delta \boldsymbol{f}_u, \sigma^i_{\hat{u}} \boldsymbol{f}^i_{\hat{u}}) \right\} \mathcal{A}(\psi, \psi^i) \\
\mathcal{R}^m_p(\delta f_p \psi) &:= \sum_{k=1}^{\mathtt{n_a}} \sum_{l=1}^{\mathtt{n_D}} \langle \delta f_p, \boldsymbol{g}^l_D \cdot \mathbf{A}^k \boldsymbol{n} \rangle_{\partial \Omega_e \cap \Gamma_D} \mathcal{A}^k_{\vartheta}(\psi, \lambda^l_D) \\
&- \sum_{i=1}^{m} \sum_{k=1}^{\mathtt{n_a}} \left\{ \mathcal{A}^k_{pu}(\delta f_p, \sigma^i_u \boldsymbol{f}^i_u) - \mathcal{A}^k_{p\hat{u}}(\delta f_p, \sigma^i_{\hat{u}} \boldsymbol{f}^i_{\hat{u}}) \right\} \mathcal{A}^k_{\vartheta}(\psi, \psi^i) \\
\mathcal{R}^m_{\overline{p}}(\delta f_\rho \psi) &:= - \sum_{i=1}^{m} \left\{ \mathcal{A}_{\rho p}(\delta f_\rho, \sigma^i_p f^i_p) - \mathcal{A}_{\rho\rho}(\delta f_\rho, \sigma^i_\rho f^i_\rho) \right\} \mathcal{A}(\psi, \psi^i),
\end{aligned}
\tag{B.1}
$$

for the HDG local problems and by

$$
\begin{aligned}
\mathcal{R}^m_{\hat{u}}(\delta \boldsymbol{f}_{\hat{u}} \psi) &:= - \sum_{l=1}^{\mathtt{n_N}} \langle \delta \boldsymbol{f}_{\hat{u}}, \boldsymbol{g}^l_N \rangle_{\partial \Omega_e \cap \Gamma_N} \mathcal{A}(\psi, \lambda^l_N) \\
&- \sum_{i=1}^{m} \left\{ \mathcal{A}_{\hat{u}u}(\delta \boldsymbol{f}_{\hat{u}}, \sigma^i_u \boldsymbol{f}^i_u) + \mathcal{A}_{\hat{u}\hat{u}}(\delta \boldsymbol{f}_{\hat{u}}, \sigma^i_{\hat{u}} \boldsymbol{f}^i_{\hat{u}}) \right\} \mathcal{A}(\psi, \psi^i) \\
&- \sum_{i=1}^{m} \sum_{k=1}^{\mathtt{n_a}} \Big\{ \mathcal{A}^k_{\hat{u}L}(\delta \boldsymbol{f}_{\hat{u}}, \sigma^i_L \boldsymbol{F}^i_L) \mathcal{A}^k_{\vartheta}(\psi, \psi^i) \\
&+ \left[\mathcal{A}^k_{\hat{u}p}(\delta \boldsymbol{f}_{\hat{u}}, \sigma^i_p f^i_p) + \mathcal{A}^k_{\hat{u}\hat{u}}(\delta \boldsymbol{f}_{\hat{u}}, \sigma^i_{\hat{u}} \boldsymbol{f}^i_{\hat{u}}) \right] \mathcal{A}^k_{\vartheta}(\psi, \psi^i) \Big\}, \\
\mathcal{R}^m_{\rho}(\delta f_\rho \psi) &:= - \sum_{k=1}^{\mathtt{n_a}} \sum_{l=1}^{\mathtt{n_D}} \langle \delta f_\rho, \boldsymbol{g}^l_D \cdot \mathbf{A}^k \boldsymbol{n} \rangle_{\partial \Omega_e \cap \Gamma_D} \mathcal{A}^k_{\vartheta}(\psi, \lambda^l_D) \\
&- \sum_{i=1}^{m} \sum_{k=1}^{\mathtt{n_a}} \mathcal{A}^k_{p\hat{u}}(\delta f_\rho, \sigma^i_{\hat{u}} \boldsymbol{f}^i_{\hat{u}}) \mathcal{A}^k_{\vartheta}(\psi, \psi^i)
\end{aligned}
\tag{B.2}
$$

for the HDG global problems.

Appendix C. Geometric mapping for the channel with two microswimmers

The mapping used in the example involving the flow around two microswimmers is designed as the composition of two mappings. The first mapping, $\boldsymbol{\mathcal{M}}_{\mu_1}$, is defined to account for the change of radius of the two spheres and it is written in the general separable expression of Eq. (22) with

$$
\mathbf{M}^1_1(\boldsymbol{x}) = \begin{cases} \dfrac{1}{r} \boldsymbol{x}^-_0 & \text{if } \|\boldsymbol{x}^-_0\| \le R_{\text{out}} \\ 0 & \text{otherwise} \end{cases} \qquad \psi^1_1(\mu_1) = \frac{R_{\text{out}}(R^+(\mu_1) - R_{\text{ref}})}{R_{\text{out}} - R_{\text{ref}}},
$$

$$
\mathbf{M}^2_1(\boldsymbol{x}) = \begin{cases} \boldsymbol{x}^-_0 & \text{if } \|\boldsymbol{x}^-_0\| \le R_{\text{out}} \\ 0 & \text{otherwise} \end{cases} \qquad \psi^2_1(\mu_1) = \frac{R_{\text{out}} - R^+(\mu_1)}{R_{\text{out}} - R_{\text{ref}}},
$$

$$
\begin{aligned}
\mathbf{M}_1^3(\boldsymbol{x}) &= \begin{cases} \boldsymbol{x}_0 & \text{if } \|\boldsymbol{x}_0^-\| \leq R_{\text{out}} \\ 0 & \text{otherwise} \end{cases} && \psi_1^3(\mu_1) = 1, \\
\mathbf{M}_1^4(\boldsymbol{x}) &= \begin{cases} \dfrac{1}{r}\boldsymbol{x}_0^+ & \text{if } \|\boldsymbol{x}_0^+\| \leq R_{\text{out}} \\ 0 & \text{otherwise} \end{cases} && \psi_1^4(\mu_1) = \dfrac{R_{\text{out}}(R^-(\mu_1) - R_{\text{ref}})}{R_{\text{out}} - R_{\text{ref}}}, \\
\mathbf{M}_1^5(\boldsymbol{x}) &= \begin{cases} \boldsymbol{x}_0^+ & \text{if } \|\boldsymbol{x}_0^+\| \leq R_{\text{out}} \\ 0 & \text{otherwise} \end{cases} && \psi_1^5(\mu_1) = \dfrac{R_{\text{out}} - R^-(\mu_1)}{R_{\text{out}} - R_{\text{ref}}}, \\
\mathbf{M}_1^6(\boldsymbol{x}) &= \begin{cases} -\boldsymbol{x}_0 & \text{if } \|\boldsymbol{x}_0^+\| \leq R_{\text{out}} \\ 0 & \text{otherwise} \end{cases} && \psi_1^6(\mu_1) = 1,
\end{aligned}
\tag{C.1}
$$

where $\boldsymbol{x}_0^{\pm} = \boldsymbol{x} \pm \boldsymbol{x}_0$, $R_{\text{out}} = 0.45$ and, as detailed in Section 5.3, $\boldsymbol{x}_0 = (1.5, 0)$ and $R_{\text{ref}} = 0.116$. The radius of the sphere centred at $\boldsymbol{x}_0$ is defined as $R^+(\mu_1) = -0.0372\mu_1^2 + 0.0968\mu_1 + 0.25$ so that it takes value 0.116 for $\mu_1 = -1$, 0.25 for $\mu_1 = 0$ and 0.3096 for $\mu_1 = 1$. The radius of the sphere centred at $-\boldsymbol{x}_0$ is defined in terms of $R^+(\mu_1)$ in such a way that the total volume of the two spheres is maintained, namely $(R^+)^3 + (R^-)^3 = 1/32$. The piecewise nature of the mapping is illustrated in Fig. C.30, in the vicinity of one of the spheres.

The second mapping, $\boldsymbol{\mathcal{M}}_{\mu_2}$, is defined to account for the change of distance between the spheres and it is written in the general separable expression of Eq. (22) with

$$
\begin{aligned}
\mathbf{M}_2^1(\boldsymbol{x}) &= \begin{Bmatrix} d(x) \\ 0 \end{Bmatrix} && \psi_2^1(\mu_2) = -x_0\mu_2/3, \\
\mathbf{M}_2^2(\boldsymbol{x}) &= \boldsymbol{x} && \psi_2^2(\mu_2) = 1,
\end{aligned}
\tag{C.2}
$$

where the function $d(x)$ is given by

$$
d(x) := \begin{cases} \dfrac{x + L}{x_0 + R_{\text{int}} - L} & \text{if } x \in [-L, -x_0 - R_{\text{int}}] \\ -1 & \text{if } x \in [-x_0 - R_{\text{int}}, -x_0 + R_{\text{int}}] \\ \dfrac{x}{x_0 - R_{\text{int}}} & \text{if } x \in [-x_0 + R_{\text{int}}, x_0 - R_{\text{int}}] \\ 1 & \text{if } x \in [x_0 - R_{\text{int}}, x_0 + R_{\text{int}}] \\ \dfrac{x - L}{x_0 + R_{\text{int}} - L} & \text{if } x \in [x_0 + R_{\text{int}}, L], \end{cases}
\tag{C.3}
$$

with $R_{\text{int}} = 0.47$ and, as detailed in Section 5.3, $L = 6$.

As illustrated in Fig. C.30 both mappings are defined in a piecewise form. The mappings selected are only $\mathcal{C}^0$ on the artificial interfaces denoted by discontinuous lines in Fig. C.30. Therefore, to facilitate the numerical integration of the terms involving the Jacobian and the adjoint of the mapping, the computational meshes selected are conforming with these interfaces, as it can be observed in the mesh displayed in Fig. 14. Mappings with higher degree of continuity could be designed using a problem specific approach or the more general technique described in [55]. Further numerical experiments, not reported here, show that a greater degree of continuity enables to use meshes that do not conform with the piecewise nature of the mapping but they do not provide any extra accuracy and they induce a higher cost due to the extra number of integration points required to integrate the higher order Jacobian of the mapping.

It is also worth noting that other mappings, with a smooth transition in the artificially created interfaces can be devised. Numerical experiments not reported here for brevity, demonstrate that the piecewise linear mapping described here results in a lower number of integration points required to ensure that errors due to the numerical integration are lower than the interpolation error. However, the choice of a smoother mapping circumvents the need to create meshes conforming with artificially created interfaces. In any case, as stressed in Remark 1, this work focuses on the combination of the HDG and PGD formulations and for general geometries the general procedure described in [19] is preferred, rather than the definition of analytical mappings.

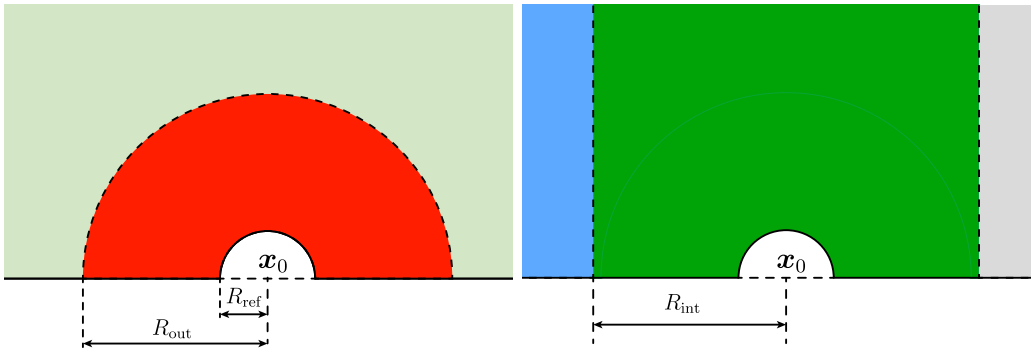

(a) $\boldsymbol{\mathcal{M}}_{\mu_1}$ (b) $\boldsymbol{\mathcal{M}}_{\mu_2}$

Fig. C.30. Illustration of the piecewise nature of the mappings $\boldsymbol{\mathcal{M}}_{\mu_1}$ and $\boldsymbol{\mathcal{M}}_{\mu_2}$ detailed in Eqs. (C.1) and (C.2) respectively in the vicinity of the sphere centred at $\boldsymbol{x}_0$.

Appendix D. Geometric mapping for the corrugated channel

Similarly to the previous example, the mapping used in the example involving the flow around a sphere in a corrugated channel is designed as the composition of two mappings. The first mapping, $\boldsymbol{\mathcal{M}}_{\mu_1}$, is defined to account for the change of radius of the sphere and it is written in the general separable expression of Eq. (22) with

$$\begin{aligned}
\mathbf{M}_1^1(\boldsymbol{x}) &= \begin{cases} \dfrac{1}{r}\boldsymbol{x} & \text{if } \|\boldsymbol{x}\| \le R_{\text{out}} \\ 0 & \text{otherwise} \end{cases} \qquad \psi_1^1(\mu_1) = \frac{R_{\text{out}}(R(\mu_1) - R_{\text{ref}})}{R_{\text{out}} - R_{\text{ref}}}, \\
\mathbf{M}_1^2(\boldsymbol{x}) &= \begin{cases} \boldsymbol{x} & \text{if } \|\boldsymbol{x}\| \le R_{\text{out}} \\ 0 & \text{otherwise} \end{cases} \qquad \psi_1^2(\mu_1) = \frac{R_{\text{out}} - R(\mu_1)}{R_{\text{out}} - R_{\text{ref}}}, \\
\mathbf{M}_1^3(\boldsymbol{x}) &= \begin{cases} \boldsymbol{x} & \text{if } \|\boldsymbol{x}\| \le R_{\text{out}} \\ 0 & \text{otherwise} \end{cases} \qquad \psi_1^3(\mu_1) = 1,
\end{aligned} \tag{D.1}$$

where $R_{\text{out}} = 0.4$ and $R_{\text{ref}} = 0.2$ and the radius of the sphere, centred at the origin, is defined as $R(\mu_1) = (\mu_1 + 2)/10$.

The second mapping, $\boldsymbol{\mathcal{M}}_{\mu_2}$, is defined to account for the change of amplitude in the undulatory part of the channel. It only affects the y coordinate and, more precisely, only the definition of f_n in Eq. (58). More precisely, the profile of the channel is given by Eq. (58) with $f_n = 1/2 + \mu_2$.

References

[1] A. Quarteroni, G. Rozza, Reduced Order Methods for Modeling and Computational Reduction, Vol. 9, Springer, 2014.
[2] G. Rozza, D.B.P. Huynh, A.T. Patera, Reduced basis approximation and a posteriori error estimation for affinely parametrized elliptic coercive partial differential equations, Arch. Comput. Methods Eng. 15 (3) (2008) 229–275.
[3] G. Berkooz, P. Holmes, J.L. Lumley, The proper orthogonal decomposition in the analysis of turbulent flows, Annu. Rev. Fluid Mech. 25 (1) (1993) 539–575.
[4] T. Lieu, C. Farhat, M. Lesoinne, Reduced-order fluid/structure modeling of a complete aircraft configuration, Comput. Methods Appl. Mech. Engrg. 195 (41) (2006) 5730–5742.
[5] F. Ballarin, A. D'Amario, S. Perotto, G. Rozza, A POD-selective inverse distance weighting method for fast parametrized shape morphing, Internat. J. Numer. Methods Engrg. 117 (8) (2019) 860–884.
[6] F. Chinesta, R. Keunings, A. Leygue, The proper generalized decomposition for advanced numerical simulations. A primer, in: Springer Briefs in Applied Sciences and Technology, Springer, Cham, 2014, p. xiv+117.
[7] F. Chinesta, P. Ladeveze, E. Cueto, A short review on model order reduction based on proper generalized decomposition, Arch. Comput. Methods Eng. 18 (4) (2011) 395.
[8] F. Chinesta, E. Cueto, A. Huerta, PGD for solving multidimensional and parametric models, in: Separated Representations and PGD-Based Model Reduction, in: CISM Courses and Lectures, vol. 554, Springer, Vienna, 2014, pp. 27–89.

[9] L. Giraldi, D. Liu, H.G. Matthies, A. Nouy, To be or not to be intrusive? The solution of parametric and stochastic equations—Proper generalized decomposition, SIAM J. Sci. Comput. 37 (1) (2015) A347–A368.
[10] X. Zou, M. Conti, P. Díez, F. Auricchio, A nonintrusive proper generalized decomposition scheme with application in biomechanics, Internat. J. Numer. Methods Engrg. 113 (2) (2018) 230–251.
[11] V. Tsiolakis, M. Giacomini, R. Sevilla, C. Othmer, A. Huerta, Nonintrusive proper generalised decomposition for parametrised incompressible flow problems in OpenFOAM, Comput. Phys. Commun. 249 (2020) 107013.
[12] F. Chinesta, A. Leygue, F. Bordeu, J. Aguado, E. Cueto, D. Gonzalez, I. Alfaro, A. Ammar, A. Huerta, PGD-based computational vademecum for efficient design, optimization and control, Arch. Comput. Methods Eng. 20 (1) (2013) 31–59.
[13] A. Leygue, E. Verron, A first step towards the use of proper general decomposition method for structural optimization, Arch. Comput. Methods Eng. 17 (4) (2010) 465–472.
[14] B. Bognet, F. Bordeu, F. Chinesta, A. Leygue, A. Poitou, Advanced simulation of models defined in plate geometries: 3D solutions with 2D computational complexity, Comput. Methods Appl. Mech. Engrg. 201 (2012) 1–12.
[15] T. Heuzé, A. Leygue, G. Racineux, Parametric modeling of an electromagnetic compression device with the proper generalized decomposition, Int. J. Mater. Form. 9 (1) (2016) 101–113.
[16] A. Ammar, A. Huerta, F. Chinesta, E. Cueto, A. Leygue, Parametric solutions involving geometry: a step towards efficient shape optimization, Comput. Methods Appl. Mech. Engrg. 268 (2014) 178–193.
[17] S. Zlotnik, P. Díez, D. Modesto, A. Huerta, Proper generalized decomposition of a geometrically parametrized heat problem with geophysical applications, Internat. J. Numer. Methods Engrg. 103 (10) (2015) 737–758.
[18] L. Chamoin, H. Thai, Certified real-time shape optimization using isogeometric analysis, pgd model reduction, and a posteriori error estimation, Internat. J. Numer. Methods Engrg. 119 (3) (2019) 151–176.
[19] R. Sevilla, S. Zlotnik, A. Huerta, Solution of geometrically parametrised problems within a CAD environment via model order reduction, Comput. Methods Appl. Mech. Engrg. 358 (2020) 112631.
[20] D. Modesto, S. Zlotnik, A. Huerta, Proper Generalized Decomposition for parameterized Helmholtz problems in heterogeneous and unbounded domains: application to harbor agitation, Comput. Methods Appl. Mech. Engrg. 295 (2015) 127–149.
[21] B. Cockburn, J. Gopalakrishnan, R. Lazarov, Unified hybridization of discontinuous Galerkin, mixed, and continuous Galerkin methods for second order elliptic problems, SIAM J. Numer. Anal. 47 (2) (2009) 1319–1365.
[22] B. Cockburn, Discontinuous Galerkin Methods for Computational Fluid Dynamics, in: E. Stein, R. de Borst, T.J.R. Hughes (Eds.), Encyclopedia of Computational Mechanics Second Edition, Vol. Part 1 Fluids, John Wiley & Sons, Ltd., Chichester, 2017.
[23] R. Sevilla, A. Huerta, Tutorial on Hybridizable Discontinuous Galerkin (HDG) for second-order elliptic problems, in: J. Schröder, P. Wriggers (Eds.), Advanced Finite Element Technologies, in: CISM International Centre for Mechanical Sciences, vol. 566, Springer International Publishing, 2016, pp. 105–129.
[24] M. Giacomini, R. Sevilla, Discontinuous Galerkin approximations in computational mechanics: hybridization, exact geometry and degree adaptivity, SN Appl. Sci. 1 (2019) 1047.
[25] M. Giacomini, R. Sevilla, A. Huerta, Tutorial on Hybridizable Discontinuous Galerkin (HDG) formulation for incompressible flow problems, in: L.D. Lorenzis, A. Düster (Eds.), Modeling in Engineering using Innovative Numerical Methods for Solids and Fluids, in: CISM International Centre for Mechanical Sciences, vol. 599, Springer International Publishing, 2020, pp. 163–201.
[26] J. Peraire, N.C. Nguyen, B. Cockburn, A hybridizable discontinuous Galerkin method for the compressible Euler and Navier-Stokes equations, in: 48th AIAA Aerospace Sciences Meeting Including the New Horizons Forum and Aerospace Exposition, Orlando, FL, 2010, AIAA 2010-363.
[27] N.C. Nguyen, J. Peraire, B. Cockburn, A hybridizable discontinuous Galerkin method for the incompressible Navier-Stokes equations, in: 48th AIAA Aerospace Sciences Meeting Including the New Horizons Forum and Aerospace Exposition, Orlando, FL, 2010, AIAA 2010-362.
[28] N.C. Nguyen, J. Peraire, B. Cockburn, Hybridizable discontinuous Galerkin methods for the time-harmonic Maxwell's equations, J. Comput. Phys. 230 (19) (2011) 7151–7175.
[29] N.C. Nguyen, J. Peraire, B. Cockburn, High-order implicit hybridizable discontinuous Galerkin methods for acoustics and elastodynamics, J. Comput. Phys. 230 (10) (2011) 3695–3718.
[30] G. Giorgiani, S. Fernández-Méndez, A. Huerta, Hybridizable Discontinuous Galerkin p-adaptivity for wave propagation problems, Internat. J. Numer. Methods Fluids 72 (12) (2013) 1244–1262.
[31] S.-C. Soon, B. Cockburn, H.K. Stolarski, A hybridizable discontinuous Galerkin method for linear elasticity, Internat. J. Numer. Methods Engrg. 80 (8) (2009) 1058–1092.
[32] H. Kabaria, A.J. Lew, B. Cockburn, A hybridizable discontinuous Galerkin formulation for non-linear elasticity, Comput. Methods Appl. Mech. Engrg. 283 (2015) 303–329.
[33] R. Sevilla, M. Giacomini, A. Karkoulias, A. Huerta, A superconvergent hybridisable discontinuous Galerkin method for linear elasticity, Internat. J. Numer. Methods Engrg. 116 (2) (2018) 91–116.
[34] R. Sevilla, A. Huerta, HDG-NEFEM with degree adaptivity for Stokes flows, J. Sci. Comput. 77 (3) (2018) 1953–1980.
[35] R. Sevilla, HDG-NEFEM for two dimensional linear elasticity, Comput. Struct. 220 (2019) 69–80.
[36] B. Cockburn, J. Gopalakrishnan, The derivation of hybridizable discontinuous Galerkin methods for Stokes flow, SIAM J. Numer. Anal. 47 (2) (2009) 1092–1125.
[37] B. Cockburn, K. Shi, Devising HDG methods for Stokes flow: an overview, Comput. & Fluids 98 (2014) 221–229.
[38] N. Nguyen, J. Peraire, B. Cockburn, A hybridizable discontinuous Galerkin method for Stokes flow, Comput. Methods Appl. Mech. Engrg. 199 (9–12) (2010) 582–597.
[39] M. Giacomini, A. Karkoulias, R. Sevilla, A. Huerta, A superconvergent HDG method for Stokes flow with strongly enforced symmetry of the stress tensor, J. Sci. Comput. 77 (3) (2018) 1679–1702.

[40] B. Cockburn, J. Gopalakrishnan, N.C. Nguyen, J. Peraire, F.-J. Sayas, Analysis of HDG methods for Stokes flow, Math. Comp. 80 (274) (2011) 723–760.
[41] A. Montlaur, S. Fernández-Méndez, A. Huerta, Discontinuous Galerkin methods for the Stokes equations using divergence-free approximations, Internat. J. Numer. Methods Fluids 57 (9) (2008) 1071–1092.
[42] N.C. Nguyen, J. Peraire, B. Cockburn, An implicit high-order hybridizable discontinuous Galerkin method for linear convection-diffusion equations, J. Comput. Phys. 228 (9) (2009) 3232–3254.
[43] N.C. Nguyen, J. Peraire, B. Cockburn, An implicit high-order hybridizable discontinuous Galerkin method for nonlinear convection-diffusion equations, J. Comput. Phys. 228 (23) (2009) 8841–8855.
[44] A.T. Patera, G. Rozza, Reduced Basis Approximation and A-Posteriori Error Estimation for Parametrized Partial Differential Equations, in: MIT Pappalardo Graduate Monographs in Mechanical Engineering, Massachusetts Institute of Technology, Cambridge, MA, USA, 2007.
[45] G. Rozza, Fundamentals of reduced basis method for problems governed by parametrized PDEs and applications, in: Separated Representations and PGD-Based Model Reduction, in: CISM Courses and Lectures, vol. 554, Springer, Vienna, 2014, pp. 153–227.
[46] D.N. Arnold, An interior penalty finite element method with discontinuous elements, SIAM J. Numer. Anal. 19 (4) (1982) 742–760.
[47] G. Allaire, Conception optimale de structures, in: Mathématiques & Applications (Berlin) [Mathematics & Applications], vol. 58, Springer-Verlag, Berlin, 2007, p. xii+278, With the collaboration of Marc Schoenauer (INRIA) in the writing of Chapter 8.
[48] P. Díez, S. Zlotnik, A. Huerta, Generalized parametric solutions in Stokes flow, Comput. Methods Appl. Mech. Engrg. 326 (2017) 223–240.
[49] P. Diez, S. Zlotnik, A. García-González, A. Huerta, Encapsulated PGD Algebraic Toolbox Operating with High-Dimensional Data, Arch. Comput. Method Eng. 27 (2020) 1321–1336.
[50] P.R. Childs, Rotating Flow, Elsevier, 2010.
[51] J. Avron, O. Kenneth, D. Oaknin, Pushmepullyou: an efficient micro-swimmer, New J. Phys. 7 (1) (2005) 234.
[52] F. Alouges, A. DeSimone, A. Lefebvre, Optimal strokes for axisymmetric microswimmers, Eur. Phys. J. E 28 (3) (2009) 279–284.
[53] X. Yang, C. Liu, Y. Li, F. Marchesoni, P. Hänggi, H. Zhang, Hydrodynamic and entropic effects on colloidal diffusion in corrugated channels, Proc. Natl. Acad. Sci. 114 (36) (2017) 9564–9569.
[54] L.M. Vieira, M. Giacomini, R. Sevilla, A. Huerta, A second-order face-centred finite volume method for elliptic problems, Comput. Methods Appl. Mech. Engrg. 358 (2020) 112655.
[55] A.E. Løvgren, Y. Maday, E.M. Rønquist, Global $\mathcal{C}^1$ maps on general domains, Math. Models Methods Appl. Sci. 19 (05) (2009) 803–832.